INFLUENCE OF OBJECTIVE FUNCTIONS ON THE IDENTIFICATION OF MATERIAL MODEL PARAMETERS FROM EXPERIMENTAL DATA

By

CHARLES FREDRICK JEKEL

A DISSERTATION PRESENTED TO THE GRADUATE SCHOOL
OF THE UNIVERSITY OF FLORIDA IN PARTIAL FULFILLMENT
OF THE REQUIREMENTS FOR THE DEGREE OF
DOCTOR OF PHILOSOPHY

UNIVERSITY OF FLORIDA

2019

This is dedicated to my family as my accomplishments would not be possible without your continued support.

ACKNOWLEDGMENTS

I would like to acknowledge Nielen Stander for his collaboration with identifying unique hysteresis curves. Nielen's recommendation to investigate noisy data proved to be very interesting. Additionally, Nielen had a number of suggestions that improved the quality of the paper.

I would like to acknowledge my funding sources. The University of Florida provided the Graduate School Preeminence Award, and The U.S. Department of Veterans Affairs provided the Dependents Education Assistance Program. This dissertation would not have been possible without both of these sources.

Thanks to Sudharshan Udhayakumar for help constructing the FE model and comparing the FE model to analytical solutions. Thanks to Andrés Bernardo for helping set up scripts to process the full displacement field data. Both Sudharshan and Andrés helped contribute to Chapter 4.

TABLE OF CONTENTS

LIST OF TABLES

LIST OF FIGURES

Abstract of Dissertation Presented to the Graduate School
of the University of Florida in Partial Fulfillment of the
Requirements for the Degree of Doctor of Philosophy

INFLUENCE OF OBJECTIVE FUNCTIONS ON THE IDENTIFICATION OF MATERIAL MODEL PARAMETERS FROM EXPERIMENTAL DATA

By

Charles Fredrick Jekel

December 2019

Chair: Rafi Haftka
Cochair: Youping Chen
Major: Mechanical Engineering

The choice of objective function has been overlooked in inverse analyses and Finite Element (FE) model updating problems, specifically in problems where the application was the identification of material parameters. These problems use optimization to find material parameters in a FE model, by getting the FE model to match some experimental responses. The optimization minimizes some objective function which assess the quality-of-fit between the two responses. Different objective functions resulted from differences in: 1) problem definition, 2) error measure, or 3) normalization of data. A chapter is dedicated to how each of these different abstractions in objective function influence the resulting material parameters. When determining parameters for a non-linear orthotropic material model from uniaxial tests, the result was that different material parameters occurred when matching either the stress-strain or the load-displacement responses. Additionally, different mathematical norms were demonstrated to result in different kinematic hardening material parameters. These norms were applied when matching complex tension-compression-tension cycle tests, and the different methods resulted in very different material parameters. There has been interest in use full-field displacement data to identify material parameters, and this work demonstrated that different normalization schemes in the displacement field residuals result in different orthotropic parameters. Linear orthotropic material parameters were better identified when the in-plane displacements had equal weight to the out-of-plane displacements. The lessons learned in this work recommend

engineers explore more than one possible objective function, as the results obtained using different objective functions may provide more insight than a single set of material parameters.

CHAPTER 1
PREFACE

Engineers typically use mathematical models based on controlled observations to design, analyze, and predict. This has been particularly prevalent in the structural analysis community, where Finite Element (FE) analysis has played an important role in the design of modern airplanes, automotive vehicles, and many other structures where the ultimate performance of the design is determined by material behavior in the context of the chosen topology. These FE models depend on many parameters characterized to represent complex material behavior. Identifying the material parameters to best describe complex material responses has been an ongoing research topic.

Inverse analyses have been used to identify material parameters in FE models. These processes have also been referred to as finite element model updating (FEMU). These problems are presented as inverse problems, because they work with the responses (effects) and attempt to calculate the material parameters (causes) in cases where the parameters cannot be directly observed. The goal in these analyses has been to find the parameters such that the FE model's response best replicates an experimental response. In this context, an inverse analysis refers to the process of using optimization to minimize the difference between experimental data and a numerical model's response. Some objective function is used to quantify the differences between responses. A few of the first works related to inverse analyses which determined material parameters include [1]–[5]. All of these papers used numerical optimization techniques to find the material parameters which minimized the difference between FE models and experimental responses.

A number of technical advances have occurred in FEMU related problems since the early contributions. New material models have been introduced to FE models which are capable of replicating more complicated material behavior, but introduce a number of additional parameters that need to be identified [6]–[9]. There have also been a number of advancements in the understanding and use of numerical optimization techniques [10]–[14]. Advancements

with optical and non-intrusive Digital Image Correlation (DIC) has lead to a number of new experimental techniques [15]. Using DIC on complex load-cases, FE model parameters have been characterized on many different materials [16]–[21]. Unfortunately, all of these studies fail to identify the influence of the objective function on the FE model parameters.

Cao and Lin [22] set out a study to understand how the objective function influences material parameter identification. The focus was on identifying parameters from multiple stress-strain curves, and three different objective functions were studied. While it can be seen that different objective functions result in different numerical models, the work focused on the comparison of the objective functions' convergence. Andrade-Campos, De-Carvalho, and Valente [23] extended the previous work, by making the proposed objective function applicable for negative and zero stress and strain values. They showed that these different objective functions resulted in different material parameters, when considering the same collection of experimental responses. The paper went on to discuss the potential advantages of incorporating each objective function. This perhaps illustrates a fundamental issue that has been overlooked in many material parameter identification problems, where the resulting material parameters are dependent upon the objective function used in the optimization.

In the context of identifying material parameters with inverse analyses, this body of work demonstrates that the choice of objective function affects the material parameters. The effects of the objective function in these inverse analyses have been overlooked for the most part of the literature, and this work presents a broad abstraction of how objective functions influence resulting material parameters. While [22] and [23] studied the objective function in such analyses, they primarily focused in a narrow scope on weighting schemes from multiple data sets. While the scope of this work can be abstracted in a way that is more fundamental to the problem of material parameter identification. This work illustrates that the choice of objective function influences identified material parameters in a variety of different applications beyond multiple data sets, which consider various materials, experiments, models, and applications.

The objective function is abstracted in three different ways throughout this work, which include: 1) problem definition, 2) error measure, and 3) normalization of data. Here problem definition relates to how the minimization problem is formulated. Typically, material parameter problems are defined by matching either a load-displacement or stress-strain response (but material parameters can be identified with other responses including heat and time). This work illustrates that the choice to define a problem in stress-strain space may produce different parameters than a problem defined in load-displacement space. In mathematics there are number of different norms which are all suitable for defining an objective function (or the quality-of-fit between two responses). This work goes on to illustrate how the choice of the norm influences resulting material parameters. Lastly, there can be many different methods to derive an objective function when dealing with full-field experimental techniques (such as DIC). This work demonstrates that different normalization techniques on the experimental data set influence resulting material parameters.

The second chapter of this document describes a process for determining parameters for a non-linear orthotropic material model for PVC-coated polyester. Two different methods were compared. Parameters were determined from an inverse analysis matching the load-displacement response from uniaxial tests. Additionally, parameters were determined directly from the stress-strain uniaxial response. The origin of the experimental data is the same for both methods, the only difference is the frame in which the problem is defined. The two approaches can be thought of as different objective functions. The results show that the material parameters are different when matching the load-displacement or the stress-strain responses. The differences in the material parameters may stem from the fact that the material model was incapable of matching the experimental response exactly.

The third chapter extends the choice of objective function to describe different error measures that assess quality-of-fit. These methods were used as the objective function to calibrate a kinematic hardening material model by measuring the error between numerical and experimental hysteresis curves. The similarity measures are convenient to use when matching

cyclic paths between a Several mathematical methods, borrowed largely from the machine learning community, were introduced to the material parameter identification problems. The different methods are related to different mathematical norms used to assess the error between two responses. The different similarity measures go on to result in different sets of material parameters.

The fourth chapter describes a material parameter problem where the normalization of data affects the material parameters. Material parameters where characterized from a bulge inflation test using full-field displacements. The inverse analysis minimizes the difference between experimental and numerical displacements. A FE model was constructed to replicate the experimental bulge inflation tests. The experimental displacement field was captured utilizing DIC. The normalization of displacement components resulted in a comparison of two different objective functions, and the normalization resulted in significantly different material parameters.

CHAPTER 2
NON-LINEAR ORTHOTROPIC MODEL FROM UNIAXIAL TESTS

A hypoelastic non-linear orthotropic material model was characterized for two different PVC-coated polyesters from uniaxial tests in the warp, fill, and 45° bias yarn directions. Ultimately the non-linear orthotropic material model fails to capture the full behavior of PVC-coated polyester. Thus the determination of material parameters depends upon which experimental response is the most important for the model to capture. Two methods are presented for determining different parameters for the non-linear orthotropic material, such that each method captures a particular aspect of the material's response better than the other method. The first approach derives the stiffness moduli as a function of strain from the experimental stress-strain response of the uniaxial tests. The second approach utilizes an inverse analysis, powered by an optimization routine, to find the best material parameters such that the experimental load-displacement response is matched in the finite element (FE) model. Additional the Poisson's effect was investigated, and the transverse uniaxial behavior is presented.*

2.1 Introduction

Coated fabrics, such as PVC-coated polyester, or other technical woven textiles are used in membrane structures. The design of membrane structures often requires some form of numerical analysis. PVC-coated polyester is generally modeled as a plane stress linear orthotropic thin shell in finite element (FE) analyses [25]–[28], because modeling the fiber interactions for a complete structure is too computationally expensive [29]. The linear orthotropic material models have been widely used despite PVC-coated polyester fundamentally violating the plane-stress assumption used by conventional FE analyses [30]. A non-linear material model may more accurately represent the complex behavior of PVC-coated polyester.

* A previous version of this chapter was published in Composite Structures [24].

For this reason, a hypoelastic plane stress non-linear orthotropic material model was selected for modeling PVC-coated polyester and other complex composite materials.

PVC-coated polyester exhibits anisotropic behavior, however the material is often simplified to behave as an orthotropic material[31]. The load-displacement response of PVC-coated polyester is highly non-linear [32]. Galliot and Luchsinger [33] defined a non-linear material model for PVC-coated polyester that was load-ratio dependent, and determined from biaxial tests of varying load-ratios. Ambroziak and Kłosowski [34] took a different approach, and defined a tri-linear orthotropic material model. The tri-linear model picked different stiffness moduli based on the elemental strain values. Both of these material models offer improvements over the traditional linear-elastic plane-stress orthotropic material model for PVC-coated polyester, but are limited to only capturing some representative response of the non-linear behavior.

A material model that may be an improvement from the previous work exists in the NLELAST model definition of MSC Marc [35]. The NLELAST model includes a simplified non-linear elastic orthotropic material model, which may be suitable for modeling PVC-coated polyester. The material model is a plane stress hypoelastic orthotropic material model for thin shell elements, where the Young's moduli (E_1 , E_2), Poisson's ratio (ν_{12}), and shear modulus (G_{12}) can be defined as functions of the strain component in their respective directions. This hypoelastic non-linear orthotropic material model for PVC-coated polyester may be useful in the design and analysis of structures that may operate in the non-linear region, while potentially providing an improved representation of the complex load-displacement behavior of the material.

With a material model chosen, the next step is to determine the appropriate material model parameters. Inverse analyses can be a useful way to characterize material parameters for the FE method. In this context, an inverse analysis is the process of using numerical optimization techniques to determine the material parameters such that a FE model matches the behavior of a physical test. One benefit of an inverse analysis is that the material may be

characterized with a load state that is more complex than traditional uniaxial or biaxial testing. Garbowski, Maier, and Novati [17] set up an inverse analysis to characterize paper samples with an orthotropic elastic-plastic hardening model. A hole was cut in the center of the biaxial samples to increase the inhomogeneous response of the specimens. Modeling materials from a complex state may provide more insight when modeling various composite structures.

In this investigation two PVC-coated polyesters are considered. The first is the VALMEX® 7318 5340, and the second is Cape Coaters (Pty) Ltd CF0700T. Two characterization methods are proposed to determine a non-linear orthotropic material model. The direct method assumes a stress-strain conventional continuum model, while the inverse method matches the materials load-displacement behavior. At the start of the project it was unknown which method will produce a non-linear orthotropic material model that more accurately represents the behavior of PVC-coated polyester. PVC-coated polyester violates the plane stress and continuum assumptions. It was a concern that simply matching the in plane stress-strain behavior is no guarantee that the load-displacement behavior will also be matched, and vice versa because of violations in the plane stress and continuum assumptions.

The purpose of this paper is to provide two methods for characterizing a material with the non-linear orthotropic material model. All the parameters used for a non-linear orthotropic material model on two different types of PVC-coated polyesters are presented in this paper. A direct method and an inverse method were used to determine the material parameters. Poisson's behavior of the material is investigated, and the limitations of the non-linear orthotropic material model are discussed.

2.2 Uniaxial Tests

The properties of the two types of PVC-coated polyester tested are listed in Table 2-1. All of the properties provided, with the exception of the material thickness, come directly from the manufacturer. The thickness was obtained from the average of ten measurements taken on the uniaxial samples.

Table 2-1. Properties of the tested PVC-coated polyester.

	VALMEX® 7318	CF0700T
warp tensile strength (ISO 1421 N/50mm)	3000	1600
fill tensile strength (ISO 1421 N/50mm)	3000	1350
grams per square meter (g/m^2)	1000	700
thickness (mm)	0.81	0.55

Uniaxial tests were conducted for both PVC-coated polyesters in the material warp, fill, and 45° bias yarn directions. For each material yarn direction, five uniaxial tests were performed. The tests were performed following the ASTM D751 standard [36] cut strip test method on a MTS Criterion® 44. Test specimens were prepared to be 25 mm in width and 175 mm in length. Clamps 30 mm wide were used to hold the specimens sufficiently flat and parallel during the test. The distance between the clamps at the start of the test was 75 mm as prescribed by the ASTM D751 standard.

Utilizing Digital Image Correlation (DIC) [37], a virtual strain gauge was used to track the displacement of the specimens. This virtual strain gauge data was the only data considered in the characterization of the non-linear orthotropic material parameters. Finite element (FE) models were constructed to replicate the physical conditions of the uniaxial test. The results of the FE models with the non-linear orthotropic material models were compared to the physical behavior of the virtual strain gauges to demonstrate the effectiveness of the material models.

The DIC generates points on the surface of an uniaxial specimen in three dimensions. Virtual strain gauges track the displacement between two points on the surface of the uniaxial specimens. A single virtual strain gauge was placed approximately in the center of each uniaxial test. The length of the various strain gauges used can be seen in Table 2-2. The strain gauge lengths were chosen to match points in the calculated full displacement field as best as possible, attempting to avoid interpolation error. The difference in initial strain gauge lengths resulted from subtle differences in the parameters used to calculate the displacement field.

Three non-linear FE models were created in MSC Marc to replicate the three distinct uniaxial tests in the warp, fill, and 45° bias material directions respectively. Symmetry is

Table 2-2. Initial virtual strain gauge length l_i for material test direction.

Direction	l_i (mm)
Warp	20.0
Fill	22.8
45° Bias	19.8

utilized to simplify the uniaxial FE models in the warp and fill directions. However, the 45° bias FE model could not take advantage of reflective symmetry as the test produced an unsymmetrical displacement field. The FE models of the warp and fill direction only model the area of the virtual strain gauge, while the entire sample is modeled between the grips for the 45° bias FE model because of the unsymmetrical response. The mesh used for the warp uniaxial test is seen in Fig. 2-1, while a similar mesh is used in the fill direction. The virtual strain gauge location on the 45° bias mesh can be seen by the two green dots in the center of Fig. 2-2.

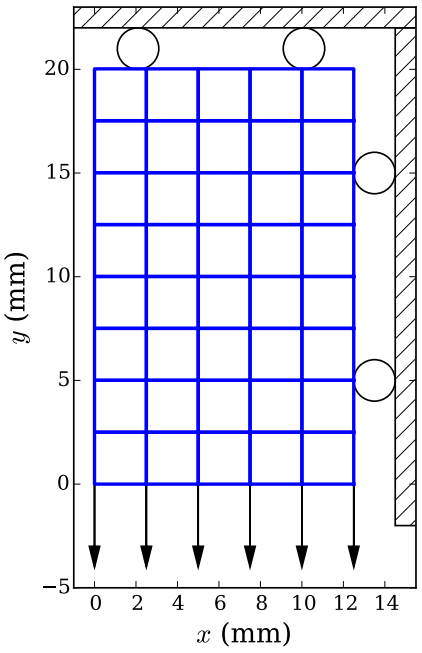

Figure 2-1. Symmetric FE mesh of the warp uniaxial test with boundary conditions.

The Young's moduli (E_1 , E_2), Poisson's ratio (ν_{12}), and shear modulus (G_{12}) are defined as functions of the strain component in their respective direction for the non-linear

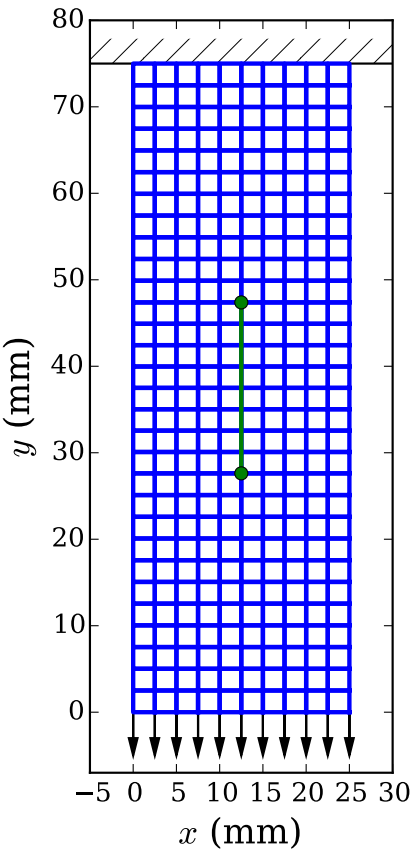

Figure 2-2. 45° bias uniaxial test FE mesh with boundary conditions and virtual strain gauge indicated by the green dots in the center of the mesh.

orthotropic material model. MSC Marc allows for the material model to define Poisson's ratio as a function of strain. However having Poisson's ratio as a function of strain presented a computational concern for the inverse problem, specifically how to determine this function. Thus it was assumed that Poisson's ratio was to be a fixed constant. The next section explains how the Poisson's ratio was determined.

2.3 Poison's Ratio

The Poisson's ratio (ν_{12}) can be expressed as the ratio of the negative transverse strain to the axial strain for a uniaxial test in the warp direction. It is possible to add an additional virtual strain gauge in the transverse direction to approximate the Poisson's ratio of the PVC-coated polyester from the uniaxial tests. A transverse strain gauge was added to every uniaxial test, with a length of 15.0 mm. The length was chosen to avoid edge effects, while still being

large enough to capture the transverse response. Only ν_{12} is needed to define the Poisson's ratio for a constant thickness orthotropic material model, as ν_{21} is determined through the material model. We can use the test results from the uniaxial warp direction to approximate Poisson's ratio, because we have set up the material warp direction to align with the primary direction in our material model.

The Poisson's ratio was calculated for the VALMEX® 7318 and CF0700T at various loads of the warp uniaxial tests. The results are presented in Figs. 2-3 and 2-4. It can be noted that the Poisson's ratio varies as the load of the material changes. There is extremely large variation between tests in the determined Poisson's ratios. A rudimentary approach was taken to deal with this variation, by simply taking the average Poisson's ratio ν_{12} from the warp tests. It was then assumed that this average Poisson's ratio was a constant in the numerical models. The average Poisson's ratio of the VALMEX® 7318 was found to be 0.136, while 0.072 was the average Poisson's ratio for CF0700T. The transverse displacements from the uniaxial tests and FE models are presented in the results section of this paper.

It is important to consider the effects of the Poisson's ratio on the FE models before characterizing the non-linear orthotropic material models. A sensitivity study was performed on the axial loads and traverse displacements of the numerical models in the warp, fill, and 45° bias material directions. The sensitivity of the axial load to Poisson's ratio is seen in Fig. 2-5. It is noted that the warp and fill uniaxial models are hardly affected by changes in ν_{12}, while the 45° bias uniaxial test is strongly linked to the value of ν_{12}. The sensitivity of the transverse displacement to Poisson's ratio is presented in Fig. 2-6. As expected the transverse displacement of the material warp and fill uniaxial tests are dependent on ν_{12}. The 45° bias uniaxial test appears to have similar sensitivity to the Poisson's ratio in both the transverse and axial directions. With the sensitivity study it was concluded that the 45° bias FE model was dependent on both ν_{12} and G_{12}, as both variables strongly influence the 45° bias response. There is a likelihood that this dependency may result in different combinations of ν_{12} and

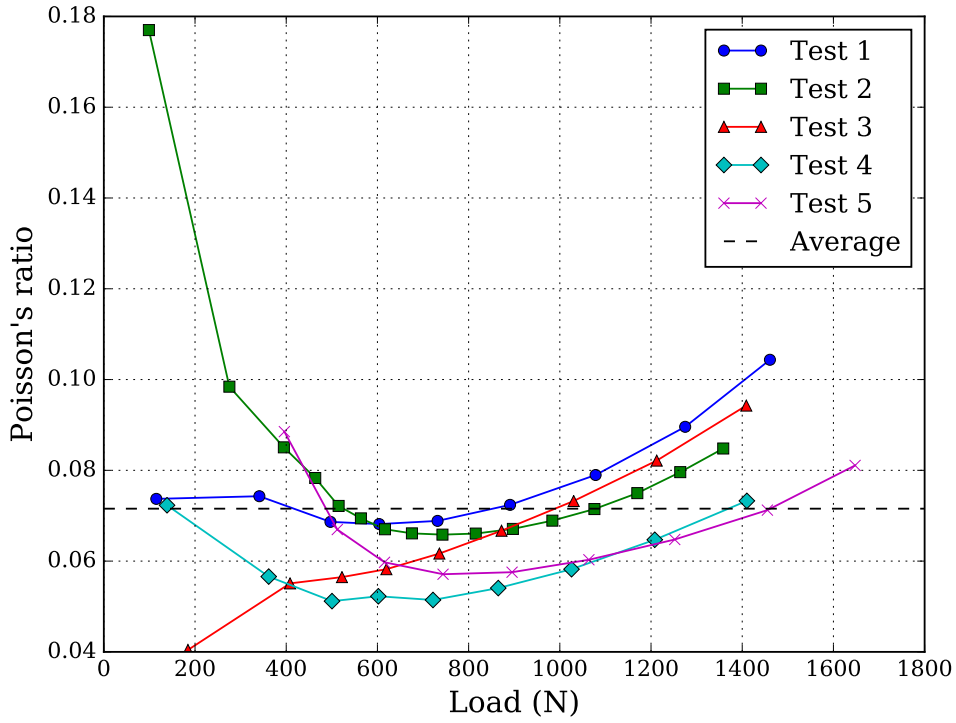

Figure 2-3. Poisson's ratio (ν_{12}) for various loads from the warp uniaxial test on VALMEX® 7318.

G_{12} producing similar behavior. Thus the simultaneous optimization of ν_{12} and G_{12}, with the 45° bias FE model, may result in a non-unique solution.

2.4 Characterization Method 1: Direct Stress-Strain Approach

The first method for characterizing the non-linear orthotropic material model uses stress and strain to determine stiffness moduli as a function of strain. The engineering strain values were calculated from the virtual strain gauges on all of the uniaxial tests. The engineering stress values were calculated by dividing the total load by the initial cross sectional area of the test specimens. Engineering stress and strain are used as opposed to true stress and strain, because the non-linear orthotropic material model does not account for through thickness change of the material. Thus the FE model is not capable of determining either true stress or true strain. In addition, the thickness change of the materials during the uniaxial tests were not measured.

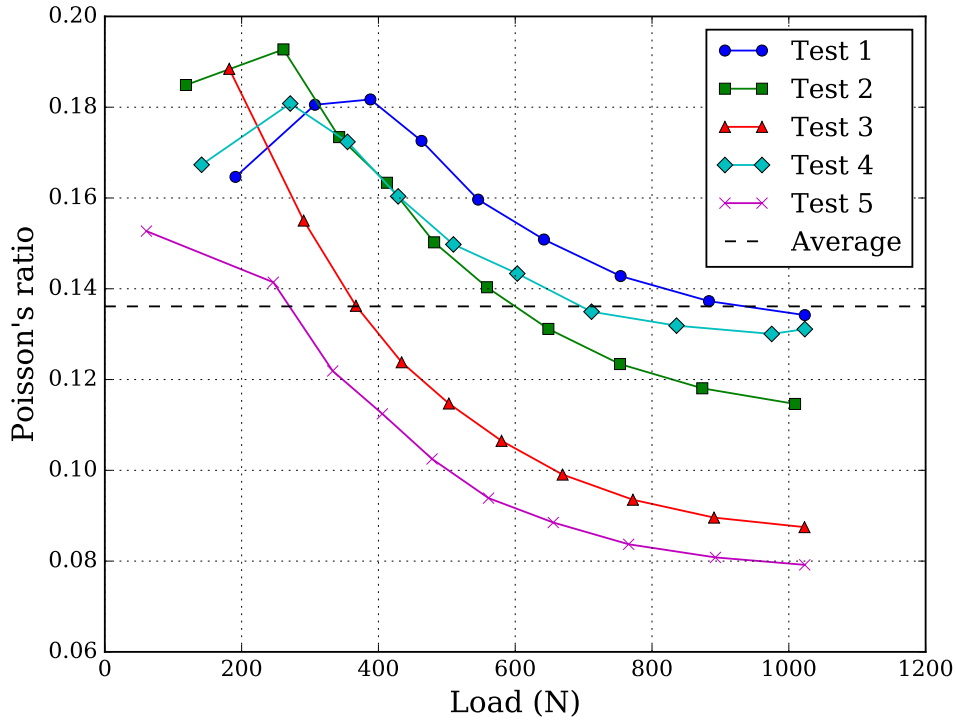

Figure 2-4. Poisson's ratio (ν_{12}) for various loads from the warp uniaxial test on CF0700T.

The stress-strain data from the uniaxial tests on the two materials is presented in Figs. 2-7 and 2-8. Data points in the figures are from all five uniaxial tests. A polynomial was fitted to the stress-strain data for each material direction using the least squares method. The data set contained each data point from the five uniaxial tests. It was useful to force the polynomial through the origin by removing the vertical intercept, because the FE model will only start from a zero stress-strain state. Different order polynomial fits were attempted. It was found that a fourth order polynomial had the lowest root mean square error for the warp uniaxial stress-strain behavior, while third order polynomials resulted in the lowest error values for the fill and 45° bias behavior. It is noted that the polynomials are excellent fits to the experimental stress-strain data. Both the coefficient of determination and the root mean square error of the fitted polynomials were used to quantify the quality of fits. The stress-strain polynomials are defined by Eqs. 2-1 - 2-3, where terms α_0 - α_9 represent the coefficients determined from the least squares fit.

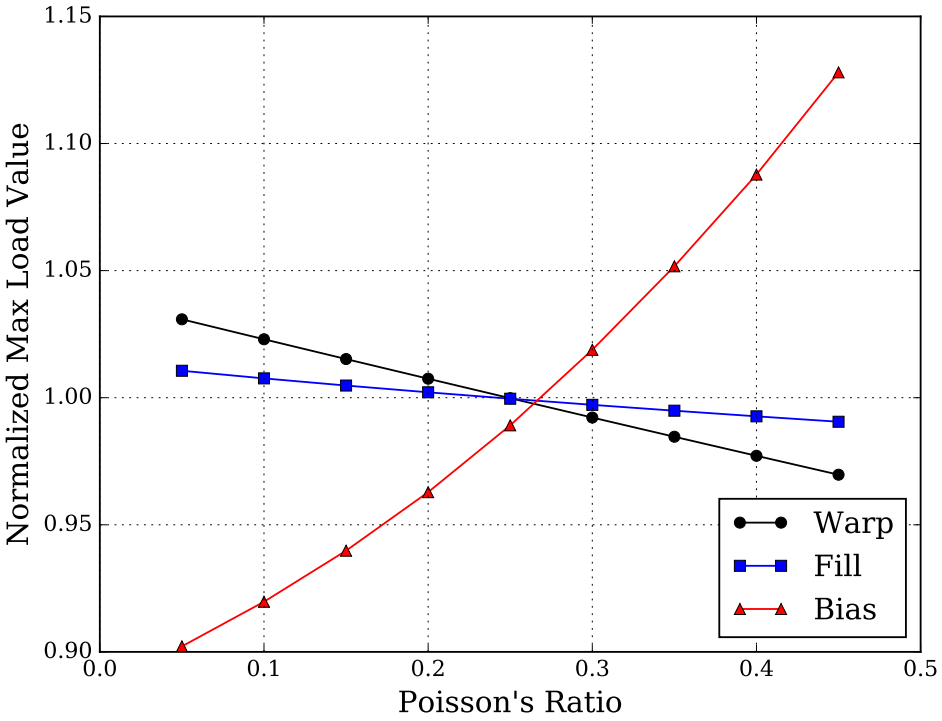

Figure 2-5. The sensitivity to Poisson's ratio of the axial load in the FE models of the warp, fill, and 45° bias uniaxial tests.

$$\sigma_{warp}(\varepsilon_1) = \alpha_0\varepsilon_1 + \alpha_1\varepsilon_1^2 + \alpha_2\varepsilon_1^3 + \alpha_3\varepsilon_1^4 \tag{2-1}$$

$$\sigma_{fill}(\varepsilon_2) = \alpha_4\varepsilon_2 + \alpha_5\varepsilon_2^2 + \alpha_6\varepsilon_2^3 \tag{2-2}$$

$$\sigma_{45°bias}(\gamma_{12}) = \alpha_7\gamma_{12} + \alpha_8\gamma_{12}^2 + \alpha_9\gamma_{12}^3 \tag{2-3}$$

Each of the fitted polynomials were differentiated to obtain the stiffness moduli as functions of strain for the non-linear orthotropic model. The stiffness moduli are defined by Eqs 2-4 - 2-6, where terms β_0 - β_9 represent the variables of the non-linear orthotropic material model. The stiffness moduli polynomials were calculated from a strain of zero, to the maximum strain as experienced by the experimental tests in each material direction. The

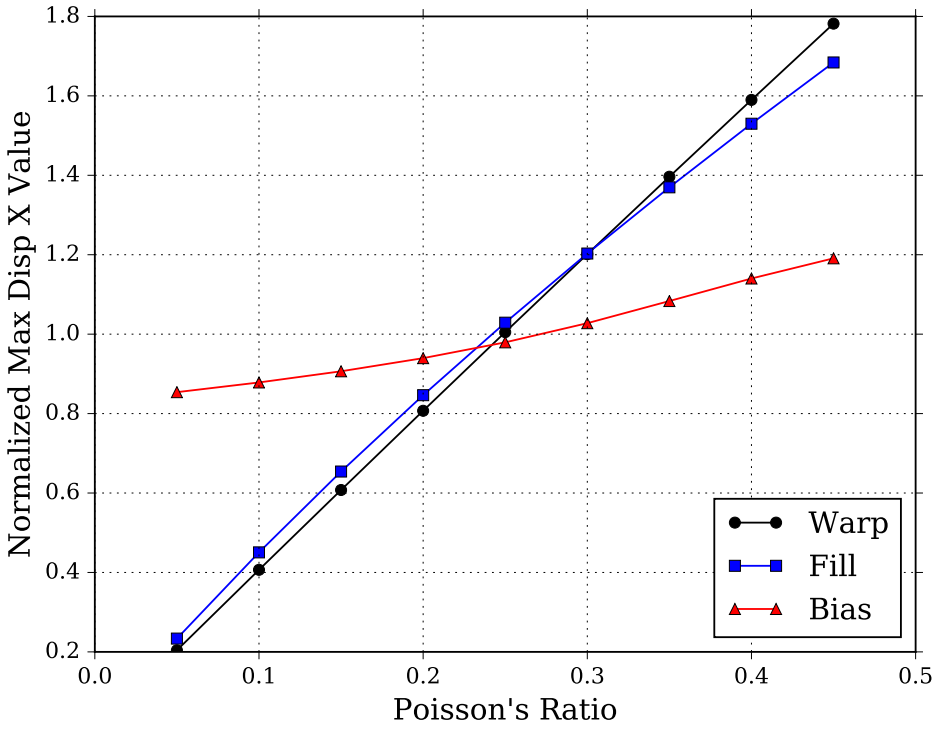

Figure 2-6. The sensitivity to Poisson's ratio of the transverse displacement in the FE models of the warp, fill, and 45° bias uniaxial tests.

vales of the stiffness moduli were then inputted as a table into the NLELAST material model definition. The FE models are useful for providing some validation, and this is done by using the defined material model in the FE models to compare with the experimental test results.

$$E_1(\varepsilon_1) = \beta_0 + \beta_1\varepsilon_1 + \beta_2\varepsilon_1^2 + \beta_3\varepsilon_1^3 \tag{2-4}$$

$$E_2(\varepsilon_2) = \beta_4 + \beta_5\varepsilon_2 + \beta_6\varepsilon_2^2 \tag{2-5}$$

$$G_{12}(\gamma_{12}) = \beta_7 + \beta_8\gamma_{12} + \beta_9\gamma_{12}^2 \tag{2-6}$$

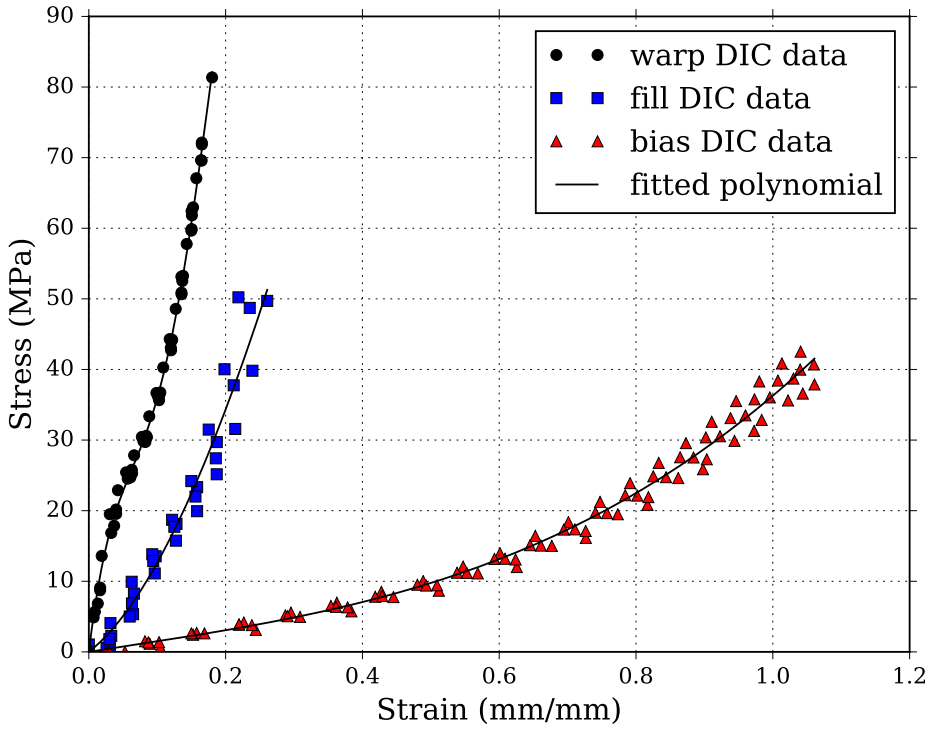

Figure 2-7. The engineering stress and strain values with fitted polynomials for VALMEX® 7318.

2.5 Characterization Method 2: Inverse Analysis Load-Displacement

As an alternative method, an inverse analysis was performed to find a non-linear orthotropic material model that matches the virtual strain gauge load-displacement response. The material parameters (β terms of Eqs. 2-4 - 2-6) are initially guessed. Then an optimization routine is used to minimize the difference between the load-displacement of the FE models and the experimental tests. The goal of the inverse analysis is to find the best material parameters, such that the FE model matches the experimental load-displacement response.

The load strain gauge displacement relationships can be seen in Figs. 2-9 and 2-10. The figures contain data points collected from all five uniaxial tests in a material direction. A polynomial, represented by the solid line, was fitted to the test data in each material direction. These polynomials were used in place of the experimental data to characterize the non-linear orthotropic material model. The experimental data from multiple runs were

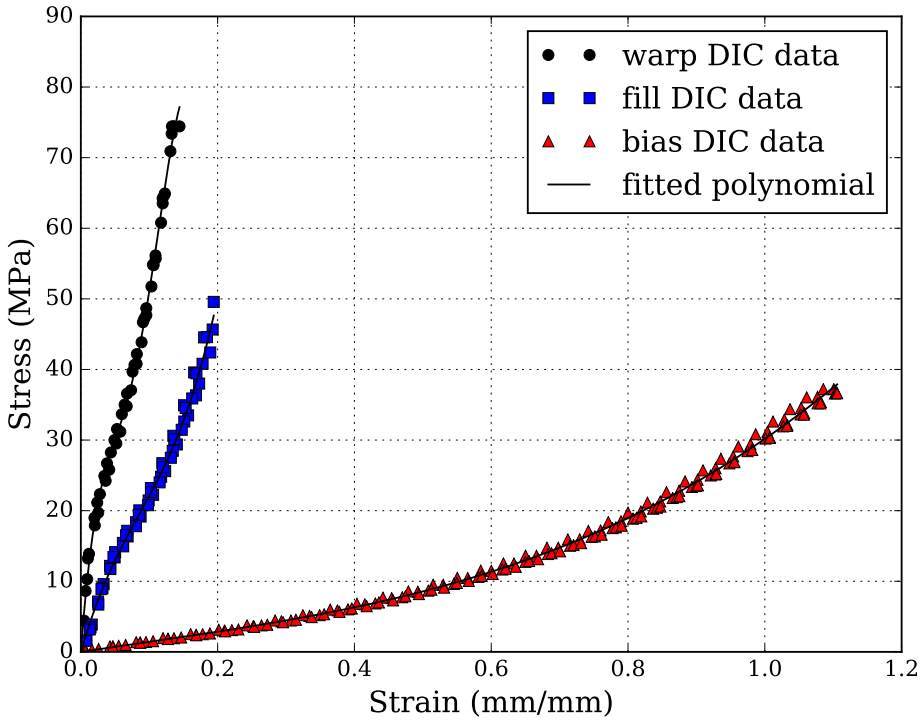

Figure 2-8. The engineering stress and strain values with fitted polynomials for CF0700T.

considered simultaneously, as the polynomials were fitted to the entire collection of data points. The polynomials were of excellent fit, as the lowest coefficient of determination of the polynomials was 0.959. Working with the polynomial is preferred over the data points, because the polynomial can be evaluated anywhere in the displacement range, so no interpolation would be needed between data points. The polynomials are used in place of the experimental data for the inverse analysis, for convenience and due to the high quality of fit.

Optimization is used to determine the best non-linear orthotropic material model by minimizing the difference between the physical uniaxial tests and the FE models. The uniaxial FE models are considered simultaneously to compute a single error value that describes the fit of the FE models to the virtual strain gauge test results. Design Optimization Tools (DOT) [38] wrapped in a Python script is used to run the FE models and determine the optimum material parameters.

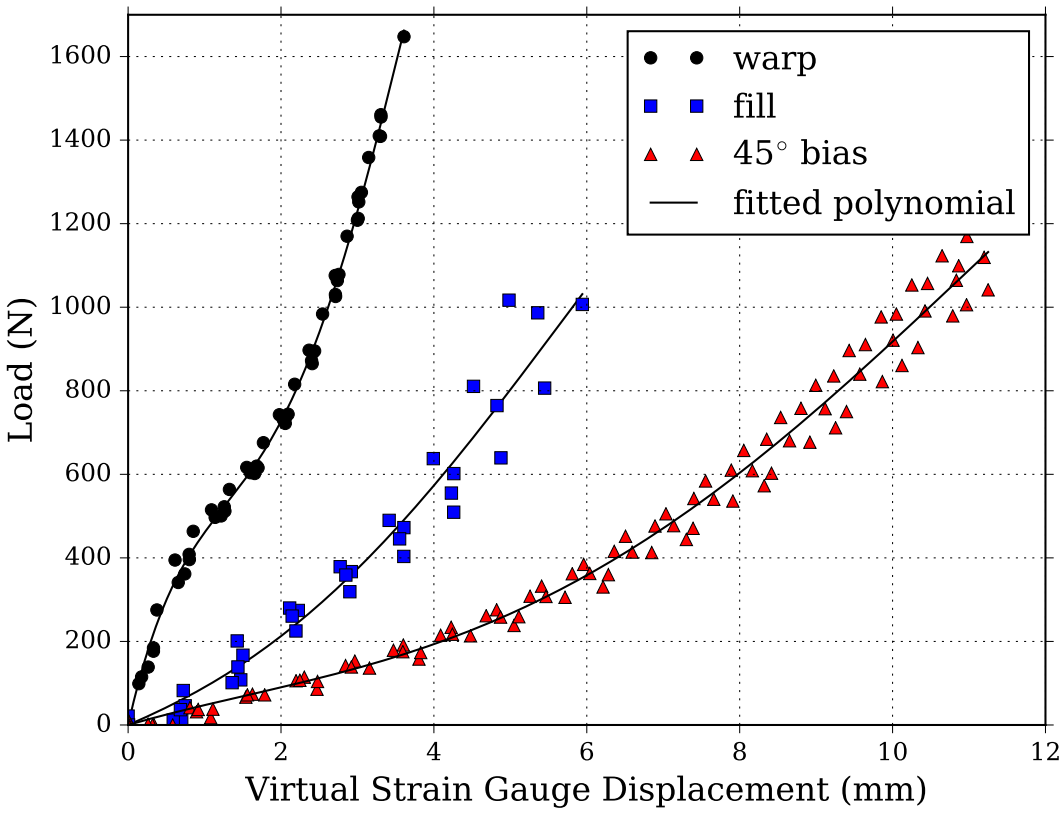

Figure 2-9. Load strain gauge displacement values for the uniaxial tests in the warp, fill, and 45° bias material directions with fitted polynomial for the VALMEX® 7318.

Root mean square (RMS) error is used to determine the error between the FE model and the physical tests. The polynomials fitted to the load-displacement virtual strain gauge data from the physical uniaxial tests are represented by P_{warp}, P_{fill}, and P_{bias}. The FE models use 100 evenly spaced displacement increments when simulating a uniaxial test. Results of the FE model are only available at these specific increments. It is important that these increments are evenly distributed to avoid sampling errors, in which the error from a particular region of the test was sampled more often because more results where available in this area than other areas. A simple example of a non-linear FE model where this phenomenon would occur is any model that utilized adaptive time stepping. At each of the 100 load increments of the FE model, the load extracted from the FE model is represented by F_{warp}, F_{fill}, and F_{bias}. The load from the

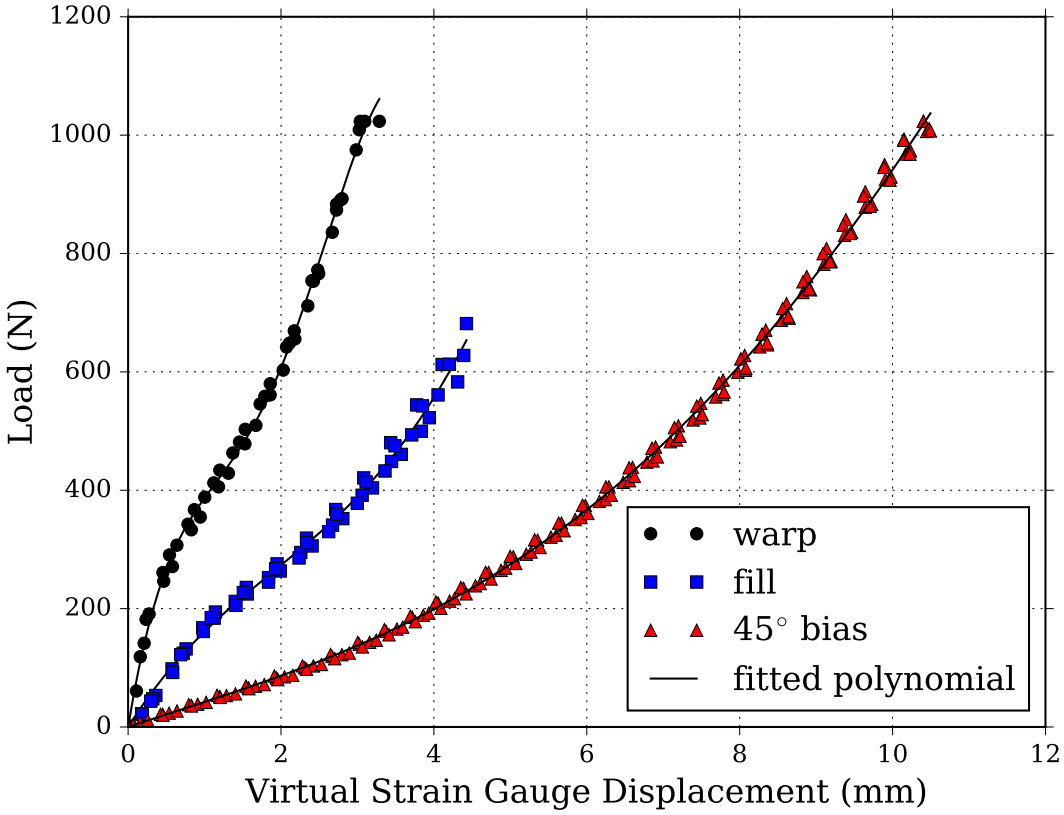

Figure 2-10. Load strain gauge displacement values for the uniaxial tests in the warp, fill, and 45° bias material directions with fitted polynomial for the CF0700T.

polynomials is compared directly with the load of the FE model at the 100 FE increments.

Three RMS errors are calculated for each material direction, and can be seen in Eqs. 2-7 - 2-9.

$$e_{warp} = \sqrt{\frac{\sum_{i=1}^{100}(F_{warp}(i) - P_{warp}(i))^2}{100}} \tag{2-7}$$

$$e_{fill} = \sqrt{\frac{\sum_{i=1}^{100}(F_{fill}(i) - P_{fill}(i))^2}{100}} \tag{2-8}$$

$$e_{bias} = \sqrt{\frac{\sum_{i=1}^{100}(F_{bias}(i) - P_{bias}(i))^2}{100}} \tag{2-9}$$

The three RMS errors can be combined into a single error value $e_{uniaxial}$. It is possible to create the single error value by simply adding up the RMS of each material direction, though it was found that the optimizations were faster when considering the sum of the square of RMS from each material direction as seen in Eq. 2-10. Each material direction is considered equally. It can be noted that weights can be added if matching the behavior of a particular uniaxial test direction was more important than the other directions. A $e_{uniaxial}$ value of 0.0 corresponds to a non-linear orthotropic material model in which the uniaxial FE models match the polynomials exactly. It is important to remember the fitted polynomials represent the experimental uniaxial load-displacement test data.

$$e_{uniaxial} = \sqrt{e_{warp}^2 + e_{fill}^2 + e_{bias}^2} \tag{2-10}$$

The overall objective function of the optimization can be expressed by minimizing the overall error of the FE models load-displacement results. The ideal material model will match the uniaxial virtual strain gauge load-displacement results exactly, while the best material model is defined mathematically as having the lowest objective function value. This optimization process is subject to two constraints, the first being that the moduli in the material model must remain positive for the entire strain range because a negative moduli for a positive strain is not sensible. The second being that all of the FE analyses are valid, in which case Marc outputs an exit code for each analysis of 3004. This is important as the optimization may attempt to try many material models that are numerically unstable, and results in FE models that can only be partially completed. Thus when an error code of 3004 is returned, it means that the FE model converged on all 100 load increments. The overall objective function can be seen in Eq. 2-11. The two constraints serve as logical flags for the constrained optimization. When a constraint is violated, a value of 1 is fed into the algorithm, while a value of -1 indicates a satisfied constraint. This type of true-false Boolean constraint may be problematic for a gradient based optimization algorithm, however DOT deals with Boolean constraints well by backtracking when encountering a violated constraint in the one

dimensional search. It is important to mention that DOT's approach works well, provided that the optimization is started from a feasible point.

$$\begin{aligned} &\text{minimize:} \quad e_{uniaxial} \\ &\text{such that:} \quad E_1, E_2, G_{12} > 0 \quad \text{and} \\ &\qquad \text{All Marc Exit Codes} = 3004 \end{aligned} \tag{2-11}$$

The β terms of Eqs. 2-4 - 2-6 are the variables the optimizer will use to determine the best non-linear orthotropic material model, however a reasonable starting point and the variable bounds are unknown. Suitable variable bounds were approximated to be one order of magnitude, larger and smaller, from the solution of the previous method. The bounds used for the optimization of both materials are provided in Table 2-3. An initial optimization was performed on β terms that began in the feasible region to satisfy the Boolean constraints.

DOT parameters were used in their default configuration, including gradient step size, scaling, and convergence criteria. From the optimum of this initial optimization, a second optimization was run with a gradient step size one order of magnitude smaller than DOT's default. The second optimization typically resulted in the lowest obtained objective function for both materials. One can point out that a suitable starting point for the optimization would be the resulting material model variables from the stress-strain method, however this approach wasn't used because it was the intention to demonstrate that the inverse analysis could function independently of the stress-strain method. The Modified Method of Feasible Directions (MMFD) algorithm proved to be the most reliable gradient based optimization algorithm from the DOT library for the inverse problems considered here. It is wise to start the optimizations from multiple starting points to ensure the best material model is found, and to avoid selecting a local minimum in the design space as the best material model.

Table 2-3. Optimization bounds used for the inverse analysis to determine the non-linear orthotropic material model.

Variable	Lower Bound	Upper Bound
β_0	0.25	2.0
β_1	-0.01	0.01
β_2	-0.001	0.001
β_3	-0.002	0.002
β_4	0.01	2.0
β_5	-0.01	0.01
β_6	-0.001	0.001
β_7	70.0	700.0
β_8	-50.0	50.0
β_9	-4.0	4.0

2.6 Results

Two different methods were used to determine non-linear orthotropic material models for VALMEX® 7318 and CF0700T. The β terms that define the material models are provided, and the material models are compared directly. It is expected that the material models will produce stress-strain and load-displacement relationships that differ from the experimental uniaxial tests, because of issues with the continuum assumption at the large strains experienced. To demonstrate these differences, the results of the FE uniaxial models with material models from both methods are compared directly to the experimental test data.

The β terms that define the non-linear orthotropic material models are presented in Table 2-4. Subtle differences in the values can be noted for the two different methods for a particular material. The non-linear orthotropic material models are plotted together in Figs. 2-11 and 2-12. The stress-strain method produced a material model that is similar to the inverse load-displacement method. In addition, the stiffness moduli of the different materials appears to be similar.

The non-linear orthotropic material models were used in FE models replicating the experimental uniaxial test. It is important to understand the ability of the FE models to replicate the behavior of the physical tests, before considering the material model in the

Table 2-4. Variables for the polynomials that define the non-linear orthotropic material models for the two types of PVC-coated polyester from the stress-strain and inverse load-displacement methods.

	VALMEX® 7318		CF0700T	
Variable	Method 1: direct	Method 2: inverse	Method 1: direct	Method 2: inverse
β_0	0.803338	0.808749	1.303904	1.007260
β_1	-0.00204	-0.00207	-0.00474	-0.00258
β_2	0.000218	0.000226	0.000679	0.000291
β_3	-0.00059	-0.00058	-0.00274	-0.00085
β_4	0.075277	0.076246	0.332784	0.346241
β_5	0.000107	0.000114	-0.00037	-0.00045
β_6	-8.2e-07	-7.5e-07	2.13e-05	3.09e-05
β_7	149.5966	270.589	145.1017	337.0310
β_8	-0.61890	-19.6316	-1.04362	-29.0470
β_9	0.073223	0.553649	0.062623	0.892731

modeling of a structure. Thus the results of the FE models were compared directly to the uniaxial test data.

The experimental stress-strain values are compared to FE results in Figs. 2-13 and 2-14. For both materials, in the warp and fill directions, the non-linear orthotropic material models do an excellent job at replicating the stress-strain behavior of the materials. Either the direct stress-strain method or inverse load-displacement method produces a stress-strain curve that is analogous to the experimental data in the warp and fill uniaxial test directions. Unfortunately the same cannot be stated for the 45° bias uniaxial test. Both methods fail to capture the behavior of the 45° bias test at high strains. For the CF0700T PVC-coated polyester, the 45° bias FE model was unstable and failed to converge to the maximum strain.[1] This is why in Fig. 2-14, the stress-strain curve resulting from the bias FE model terminates before 0.2

[1] From the author's experience, the only way to get the 45° bias model to converge with this particular set of material model parameters is to use a coarser mesh. The convergence problem is linked to an element becoming singular during the deformation. Generally when a finer mesh is used, the number of singular elements increases. The results of the model with a coarser mesh were not shown in this result section, because it would not be a fair comparison with the other FE models.

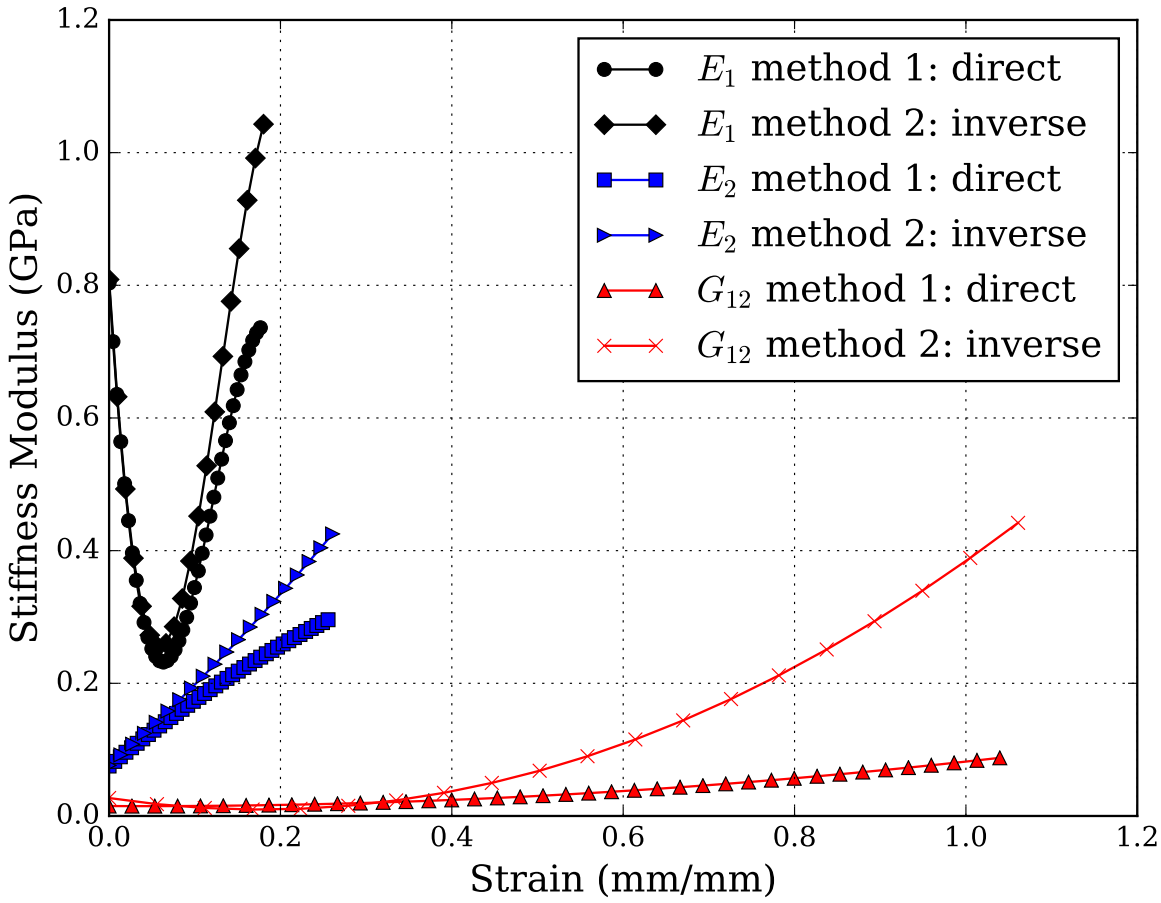

Figure 2-11. Non-linear orthotropic material models for VALMEX® 7318 from the direct stress-strain and inverse load-displacement methods.

strain instead of the maximum 0.5 strain. The inverse load-displacement non-linear orthotropic material model also severely over predicts the response of the bias extension test, though it appears the inverse load-displacement method produces a material model that better represents the 45° bias uniaxial test behavior.

The axial virtual strain gauge displacements are compared to the results of the FE models in Figs. 2-15 and 2-16. Again in the material warp and fill directions, it can be noted that both the direct stress-strain and inverse load-displacement methods produce non-linear orthotropic models that match the physical uniaxial behavior. The inverse load-displacement method was defined to match the load-displacement behavior, and effectively accomplishes this by matching the load-displacement behavior of the experimental tests data for each material direction

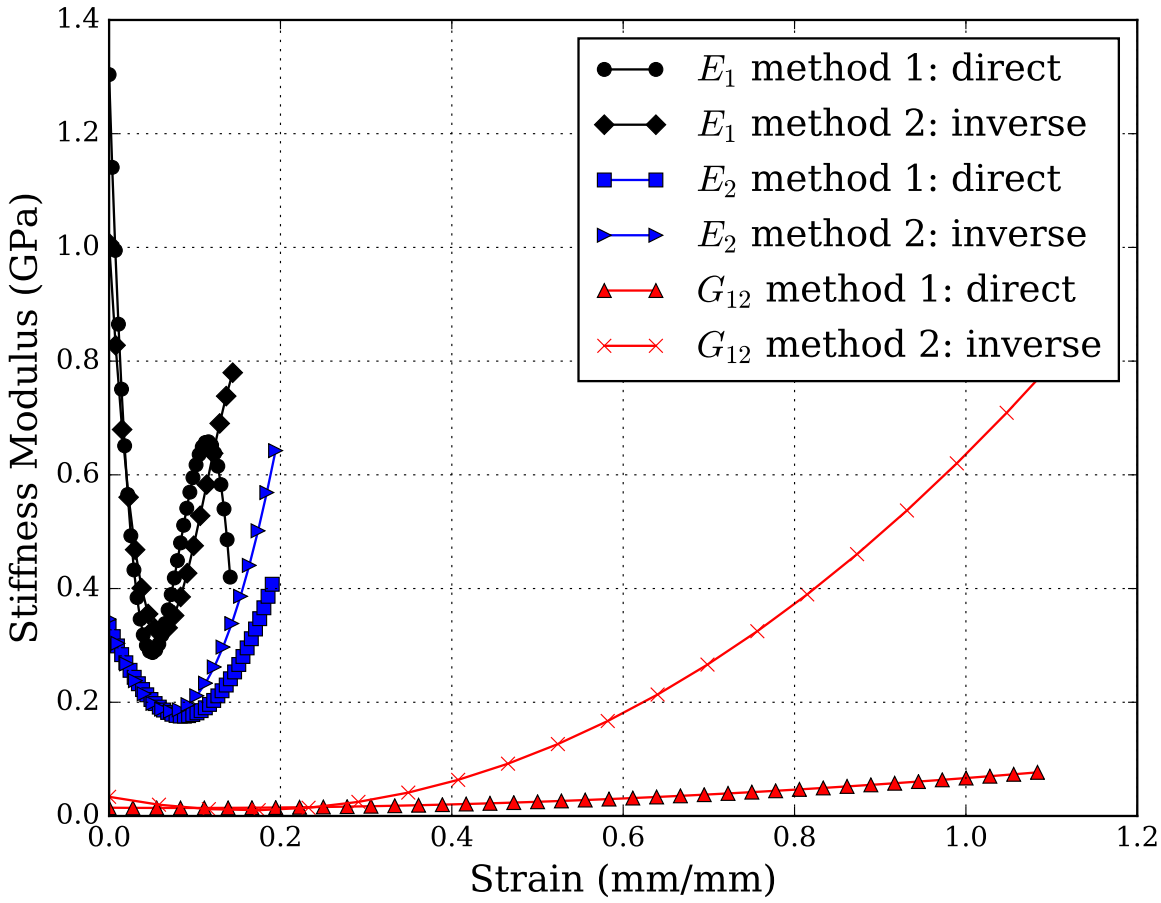

Figure 2-12. Non-linear orthotropic material models for CF0700T from the direct stress-strain and inverse load-displacement methods.

almost exactly. The direct stress-strain method produces a non-linear orthotropic material model that severely under predicts the load-displacement response of the 45° bias test.

The coefficient of determination was calculated for each comparison of the non-linear orthotropic FE models to the experimental uniaxial data. As seen in Table 2-5, the inverse load-displacement method produced similar coefficient of determinations. This suggests that the inverse load-displacement method produced non-linear orthotropic material models that are analogous to the direct stress-strain method. N/A in the table represents the FE models that were unstable, and failed to converge.

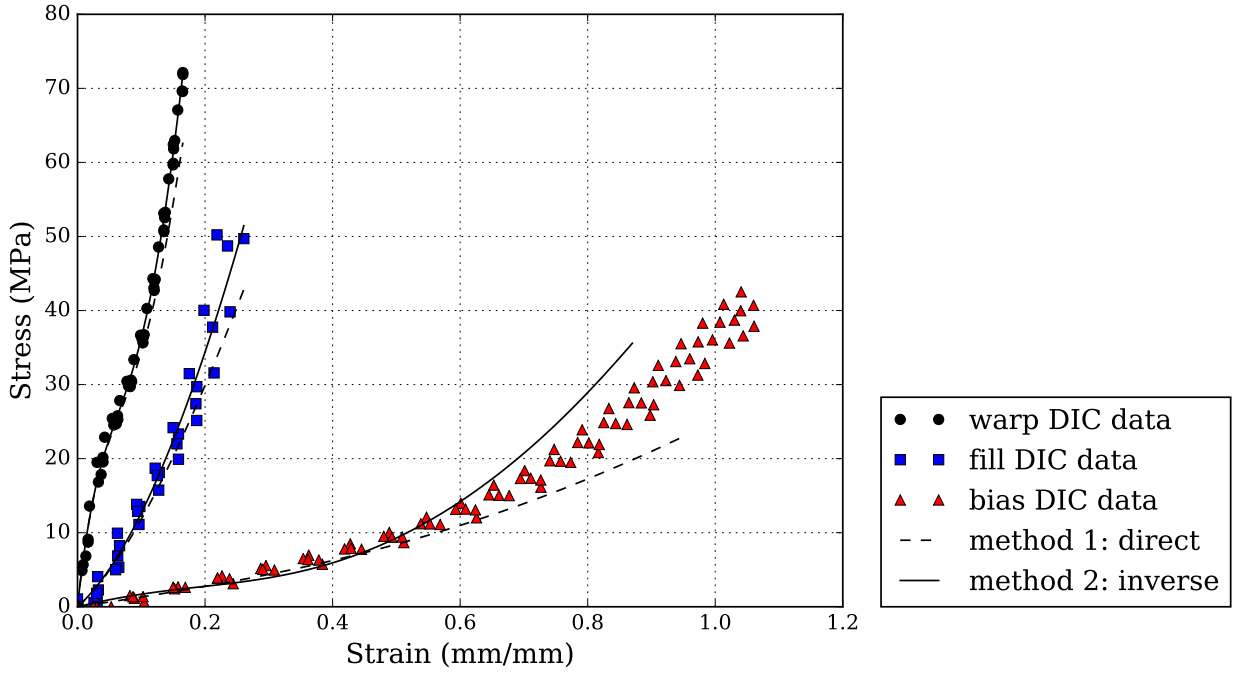

Figure 2-13. Stress-strain results of the FE models with the two different material models compared to the experimental uniaxial data for VALMEX® 7318.

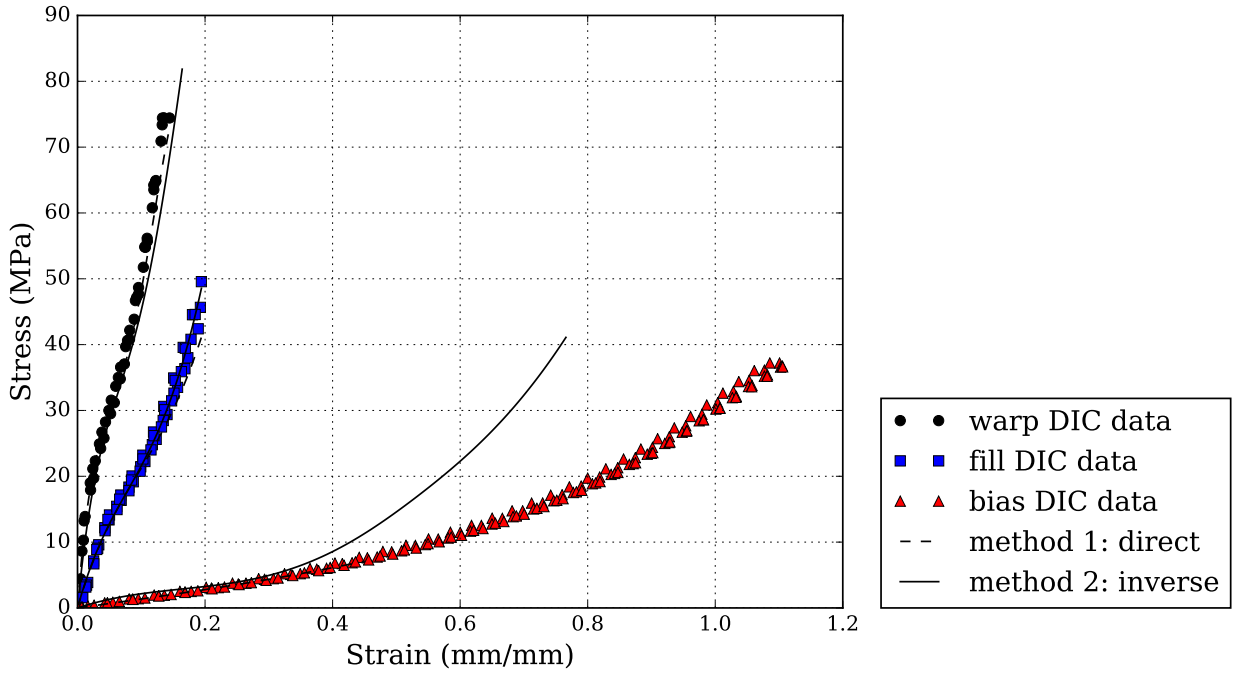

Figure 2-14. Stress-strain results of the FE models with the two different material models compared to the experimental uniaxial data for CF0700T.

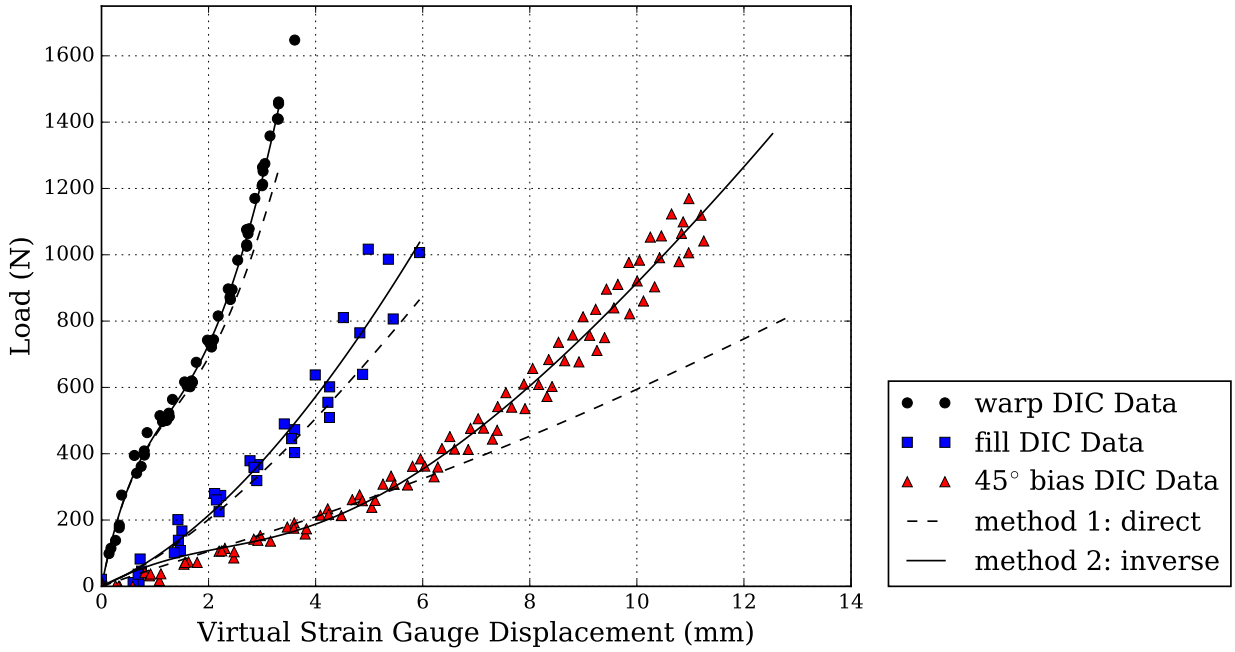

Figure 2-15. Virtual strain gauge results of the FE models with the two different material models compared to the experimental uniaxial data for VALMEX® 7318.

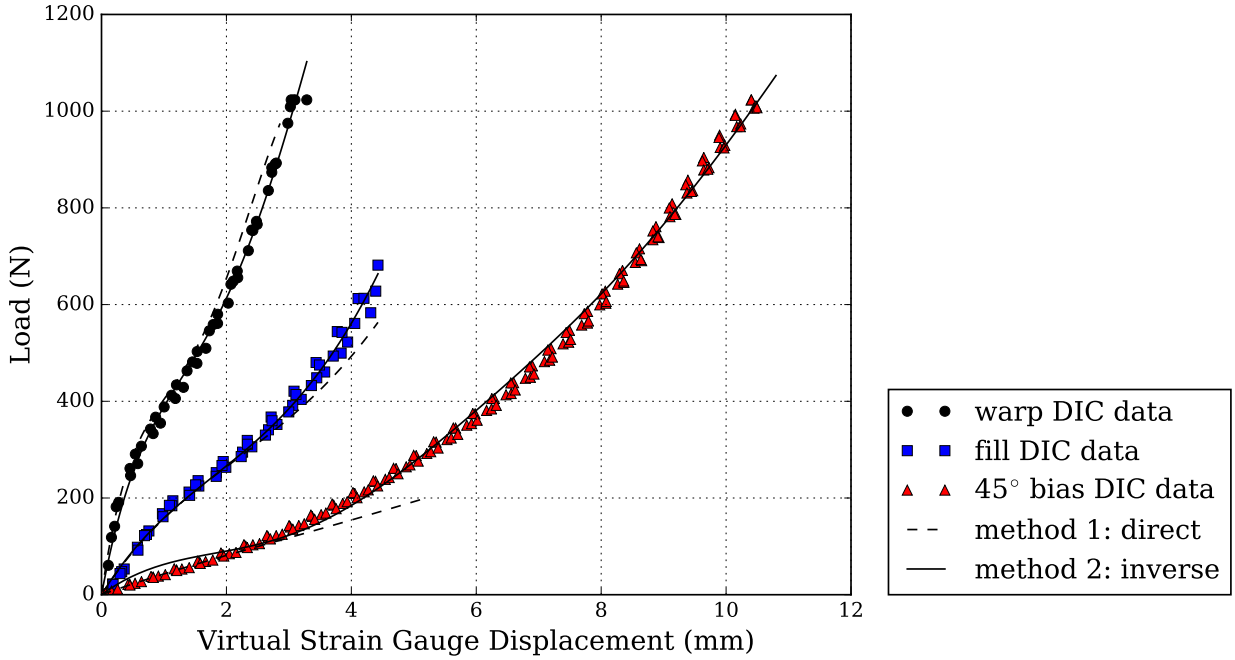

Figure 2-16. Virtual strain gauge results of the FE models with the two different material models compared to the experimental uniaxial data for CF0700T.

Table 2-5. Coefficient of determination for each stress-strain or load-displacement material comparison from the FE results using the non-linear orthotropic material models.

	VALMEX® 7318		CF0700T	
Material comparison	Method 1: direct	Method 2: inverse	Method 1: direct	Method 2: inverse
R^2 of warp stress-strain	0.97	0.99	0.99	0.94
R^2 of warp load-displacement	0.96	0.99	0.98	0.99
R^2 of fill stress-strain	0.92	0.95	0.97	0.99
R^2 of fill load-displacement	0.92	0.95	0.97	0.99
R^2 of 45° bias stress-strain	0.84	0.82	N/A	0.0
R^2 of 45° bias load-displacement	0.71	0.98	N/A	0.99
Average R^2 for method	0.89	0.95	N/A	0.82

An excellent material model would be able to accurately predict both the axial and transverse load-displacement material response. The transverse displacement of the FE models were compared to the results from a virtual horizontal strain gauge on the experimental uniaxial tests. It is seen that the non-linear orthotropic material model matches the transverse load-displacement response of the materials in the warp direction, as seen in Figs. 2-17 and 2-18. This suggests that the use and determination of the Poisson's ratio (ν_{12}) adequately matches the response of both materials in the warp direction. The transverse load-displacements, seen in Figs. 2-19 and 2-20, are poor and over estimated for the fill uniaxial test. Potentially this shows that the non-linear orthotropic material model behaves fundamentally different than the physical behavior of the PVC-coated polyester. It is interesting to point out that the transverse comparison in the 45° bias direction yields a different result, as seen in Figs. 2-21 and 2-22. It appears that the direct stress-strain method doesn't match the transverse behavior of the 45° bias extension test, while the material model from the inverse load-displacement analysis matches the transverse displacement extremely well at low strains. Though the good fit quickly deteriorates at higher strains, potentially demonstrating the limitations of the non-linear orthotropic material model.

A lack-of-fit study was performed in Appendix A to determine whether the material model adequately describes the data. The study considered two different variance estimators to perform a lack-of-fit test on each of the six test cases. Lack-of-fit was only present in the CF0700T 45° bias test. This indicates that the experimental data was not adequately explained by the material model, and the region of interest is highlighted with residual plots. The cause of lack-of-fit is due to the uniaxial test data being extremely compliant in the first mm of displacement, that the FE model is incapable of replicating.

2.7 Conclusion

Non-linear orthotropic material models were determined for two different PVC-coated polyesters. The material models were determined using two different methods. The first method determined the non-linear orthotropic model by differentiating the stress-strain

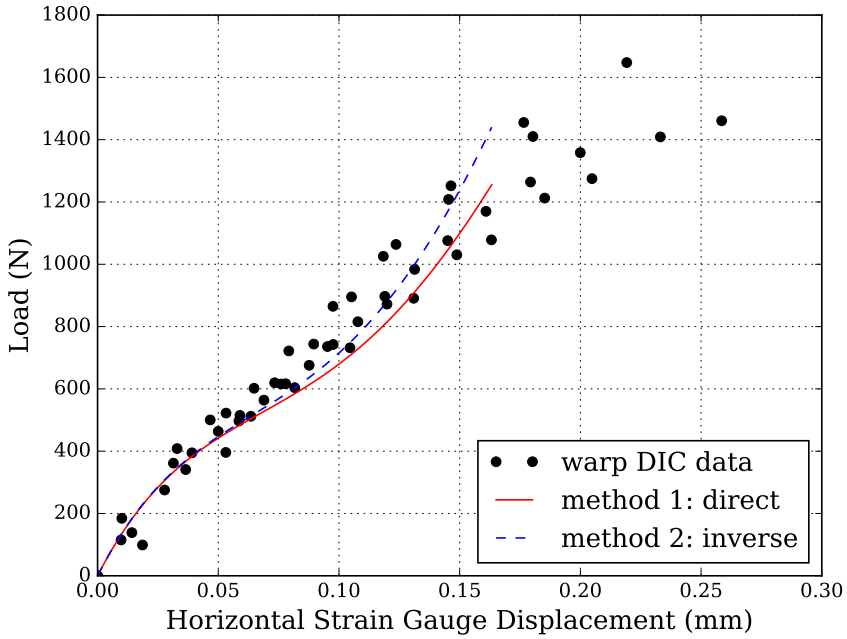

Figure 2-17. Transverse displacement of the FE models compared with the experimental warp uniaxial test data for VALMEX® 7318.

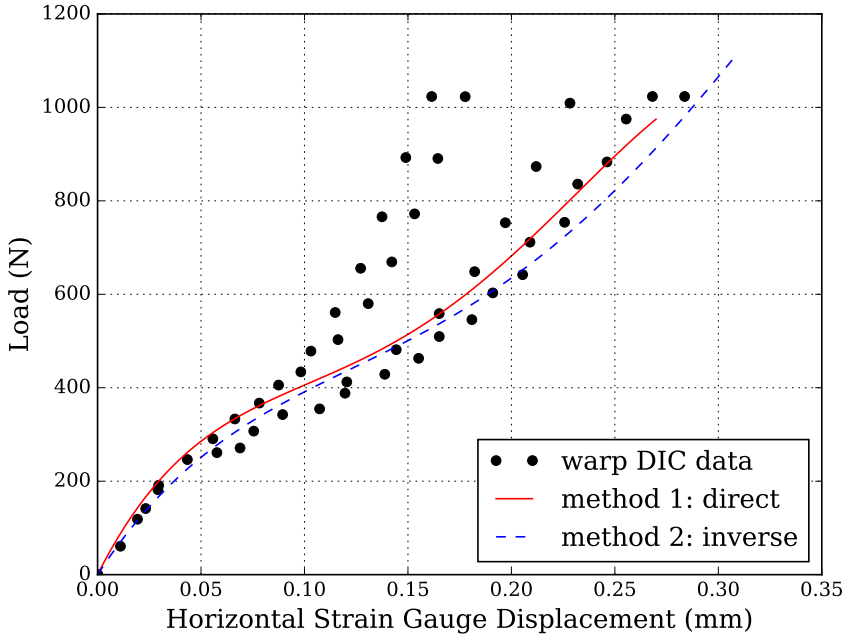

Figure 2-18. Transverse displacement of the FE models compared with the experimental warp uniaxial test data for CF0700T.

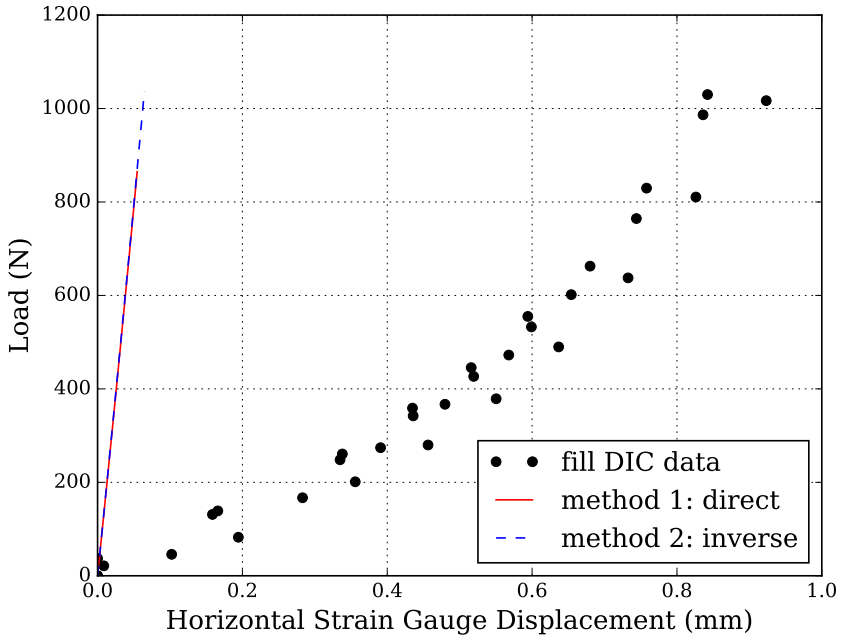

Figure 2-19. Transverse displacement of the FE models compared with the experimental fill uniaxial test data for VALMEX® 7318.

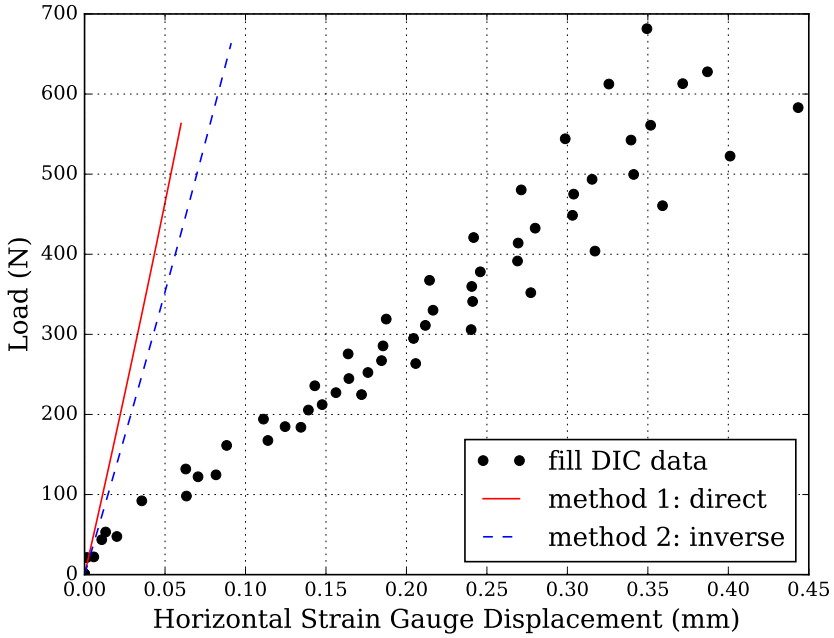

Figure 2-20. Transverse displacement of the FE models compared with the experimental fill uniaxial test data for CF0700T.

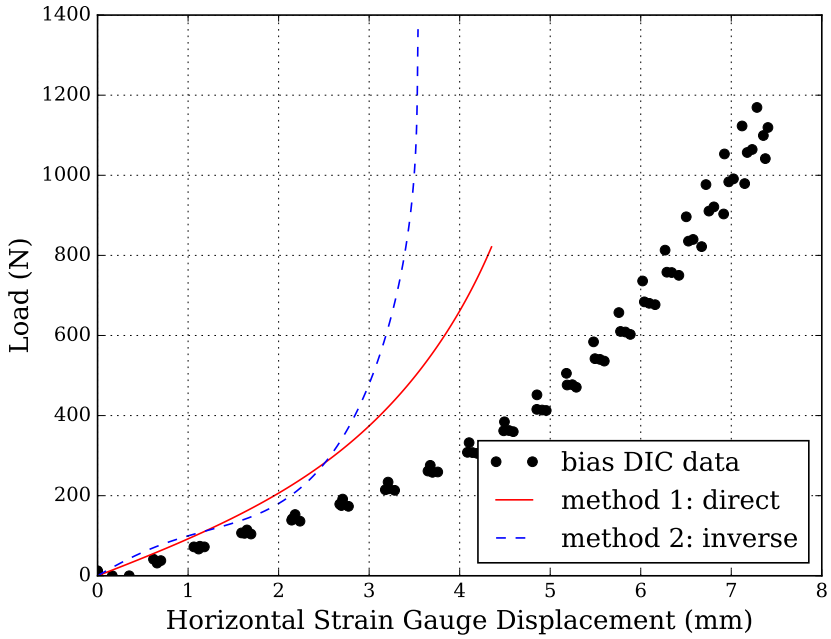

Figure 2-21. Transverse displacement of the FE models compared with the experimental 45° bias uniaxial test data for VALMEX® 7318.

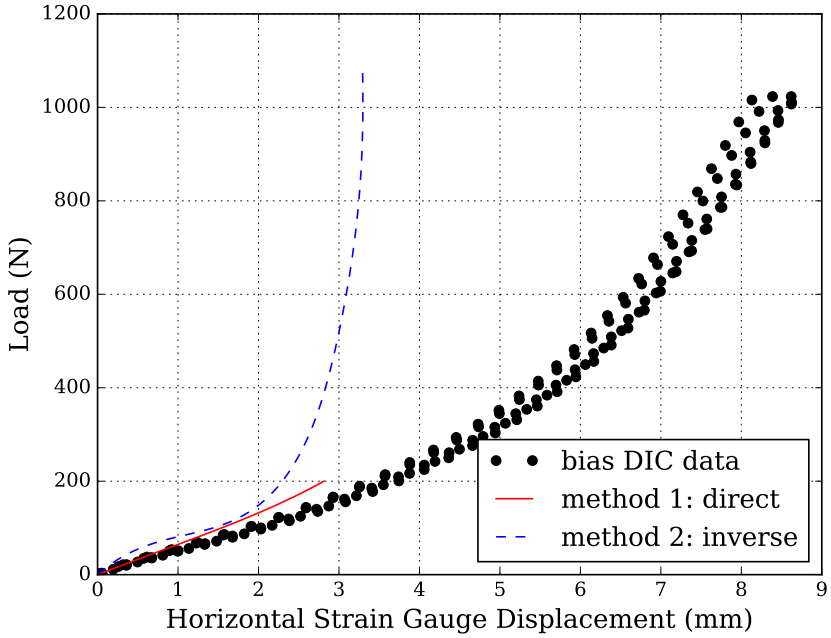

Figure 2-22. Transverse displacement of the FE models compared with the experimental 45° bias uniaxial test data for CF0700T.

response from uniaxial tests. The second method utilized an inverse analysis that produced a non-linear orthotropic material model through numerical optimization, by matching the FE models to the uniaxial load-displacement response. The two approaches produce different material model parameters, however at small strains the material behavior from the different methods is comparable. Due to breakdowns in the plane-stress continuum assumption and the large strains exposed in the uniaxial models, it is impossible to match the complete stress-strain and load-displacement material responses at high strains with this material model.

The derived non-linear orthotropic models failed to capture the complete uniaxial response in the 45° bias extension test for both PVC-coated polyesters. The direct stress-strain method produced a non-linear orthotropic material model that matched the experimental stress-strain response better than the material model from the inverse load-displacement method. While the inverse analysis proved useful, as a method to accurately reproduce the load-displacement behavior of the experimental bias test seen in Figs. 2-15 and 2-16. Though due to the limitations of the non-linear orthotropic model, the inverse method produced a model that over predicted the stress-strain response of the bias extension test. There is an effective trade-off between matching either the stress-strain or the load-displacement response with the 45° bias extension test at high strains, because the 45° bias test produces a complex load case that the hypoelastic non-linear orthotropic material model is incapable of recreating.

The Poisson's ratio (ν_{12}) was determined using the transverse and axial displacements from the warp uniaxial tests. It was demonstrated that by simply taking the average of calculated Poisson's ratios, a suitable Poisson's ratio can be determined for the warp uniaxial test. This was demonstrated for the material model by the traverse load-displacement results of a warp uniaxial test, as seen in Figs. 2-17 and 2-18. For the warp uniaxial test, all non-linear orthotropic material models matched the axial and transverse displacements excellently. However the Poisson's effect observed in the experimental fill and bias uniaxial tests is vastly different from what the non-linear orthotropic material model is capable of offering. With the combination of transverse displacement results for the fill direction in Figs. 2-19 and 2-20

and the transverse displacement sensitivity study of Fig. 2-6, it was concluded that it was not possible for the presented non-linear orthotropic material model to simultaneously match the transverse displacements in both the warp and fill uniaxial tests.

CHAPTER 3
SIMILARITY MEASURES TO IDENTIFY MATERIAL PARAMETERS FROM HYSTERESIS CURVES

Sum-of-square based error formulations may be difficult to implement on an inverse analysis consisting of multiple tension-compression hysteresis loops. Five alternative measures of similarity between curves are investigated as useful tools to help identify parameters from hysteresis loops with inverse analyses. A new algorithm is presented to calculate the area between curves. Four additional methods are presented from literature, which include the Partial Curve Mapping value, discrete Fréchet distance, Dynamic Time Warping, and Curve Length approach. These similarity measures are compared by solving a non-linear regression problem resembling a single load-unload cycle. The measures are then used to solve more complicated inverse analysis, where material parameters are identified for a kinematic hardening transversely anisotropic material model. The inverse analysis finds material parameters such that a non-linear FE model reproduces the behavior from five experimental hysteresis loops. Each method was shown to find useful parameters for these problems, and should be considered a viable alternative when sum-of-square based methods may be difficult to implement. It is important to consider multiple similarity measures in cases when it is impossible to obtain a perfect match.*

3.1 Introduction

The calibration of model parameters to find models which reproduce experimental hysteresis tension-compression cycles is difficult. There are a wide variety of material models implemented in commercial finite element (FE) software. Unfortunately the selection of appropriate parameters for these models is not a simple process, despite the advancements in experiential methods, constitutive models, and the FE method. In some applications constitutive parameters can be determined by a curve fit from experimental data as done

* A previous version of this chapter was published in the International Journal of Material Forming [39].

with a number of generalized polynomial strain energy models [40]. Alternatively full-field displacement methods provided by non-invasive optical techniques have been used with the virtual fields methods to identify constitutive parameters [41], [42]. Another solution has been to use an inverse analysis to identify material parameters in a process of updating a FE model, where material parameters are determined such that the FE model's response best replicates an experiment. The focus of this paper is on the objective function that quantifies the quality of fit between two different responses.

In this context an inverse analysis refers to the process of using optimization to minimize the difference between experimental data and a numerical model's response. Some objective function is used to quantify the differences between responses. A few of the first works related to inverse analysis to determine material parameters include [1]–[5]. For various hysteresis and hardening parameter identification problems, objective functions based on the sum-of-squares have been used. While the use of a sum-of-squares objective function is widely established, other similarity measures may be easier to work with when dealing with experimental hysteresis loops.

It is well-established to use a sum-of-square based objective function with inverse analysis to identify material parameters. Lederer, Igarashi, Kost, *et al.* [43] used a root means square quality function to measure the difference between experimental and numerical magnetic hysteresis curves. Haddadi, Bouvier, Banu, *et al.* [44] used a form of mean square error as the cost function to identify kinematic hardening and micro-structural model parameters. The mean square error compared the difference of stress and hardening rates between a FE model and experimental data. Eggertsen and Mattiasson [45] used a weighted mean square error to identify material parameters for hardening laws with an inverse analysis. Harth, Schwan, Lehn, *et al.* [46] described using a weighted sum of differences between experimental and numerical models to identify the optimum material parameters for inelastic constitutive models. Rabahallah, Balan, Bouvier, *et al.* [6], Souto, Andrade-Campos, and Thuillier [7], Yoshida, Urabe, Hino, *et al.* [8] used a weighted sum-of-squares objective function to identify

material parameters from inverse analysis on hysteresis loops. De-Carvalho, Valente, and Andrade-Campos [47] concluded that a weighted sum-of-squares objective function was more appropriate than a single point objective function for complicated geometric phenomena including necking, springback, and stress concentration.

A typical sum-of-squares is defined as

$$SS = \sum_{i=1}^{n} \left(f(x_i) - \hat{f}(x_i) \right)^2 \tag{3-1}$$

where f is the experimental data, $\hat{f}$ is the numerical model, and the difference is taken at the same x_i condition. Often differences in stress between the experimental and numerical data are calculated for the same strain values [7], [44], [47]–[49].

Now consider the simple example in Fig. 3-1 of some potential noisy material load-unload response accompanied with a numerical model that replicates that response. Initially in A) it may appear trivial to apply the sum-of-squares, though when zooming into the data as shown in B) it appears that the experimental data does not share mutual strain or stress values in order to calculate the sum-of-squares. There is essentially no concurrent x_i to calculate the difference between the experimental data and numerical model.

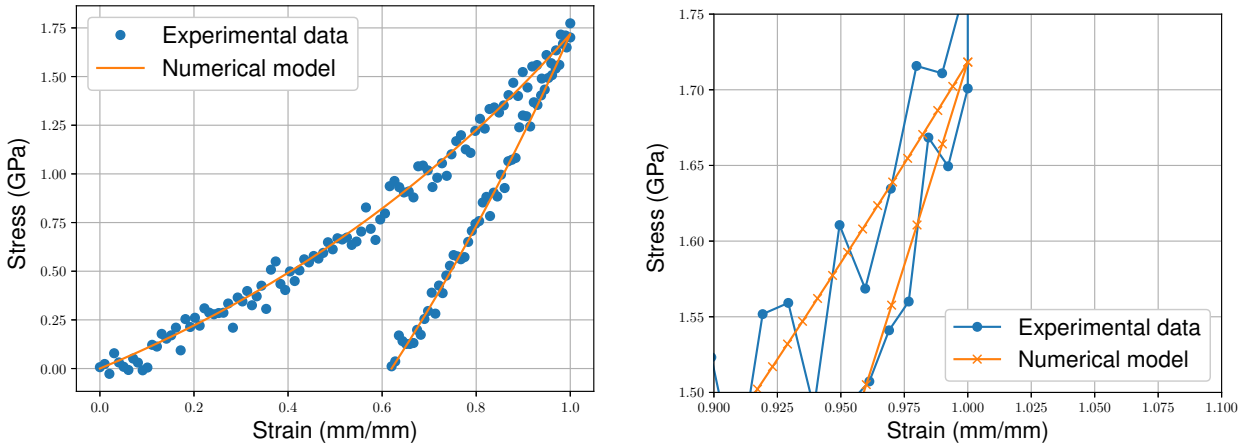

A Complete data

B Area of interest

Figure 3-1. Example of a potential material load-unload response and the numerical model replication of the response where A) shows the complete data while B) shows a zoomed-in area of interest and the order of the experimental data points.

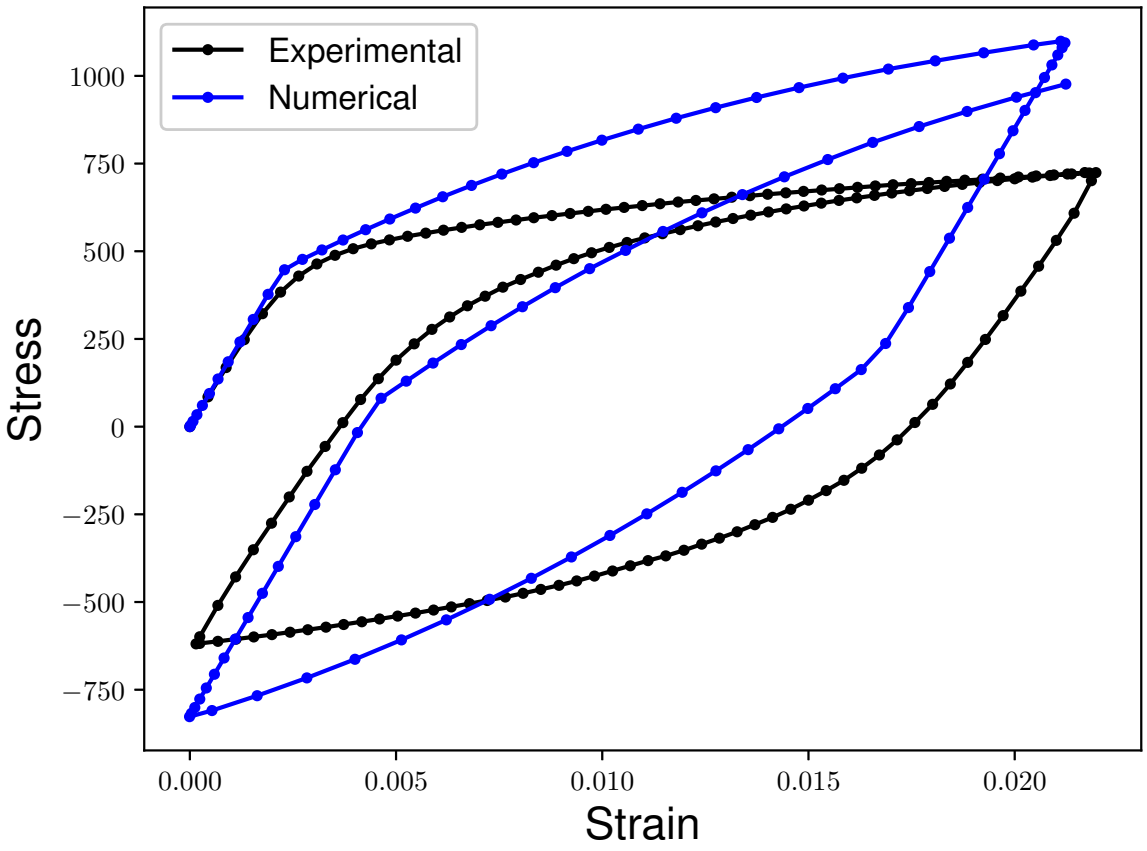

Figure 3-2. Assessing the quality of the numerical model's match of the experimental response is difficult for material tension-compression-tension curves.

A tension-compression-tension test with experimental data and the results from a numerical model is shown in Fig. 3-2. There exists some set of numerical model parameters which will result in the numerical curve aligning with the experimental curve exactly. Often, an optimization is run to find the best set of parameters that minimize the error between two curves. Traditionally the error has been defined as a sum-of-square based objective function. However, in this case it is not possible to directly apply a sum-of-squares function to quantify the difference between the numerical model and experimental data. One problem is that there are a different number of data points on the experimental curve than the numerical curve. Additionally, there are no concurrent stress or strain values to take a difference of as required by a sum-of-squares function. An alternative objective function is needed to measure the similarity between the two curves.

Several other methods have been proposed in response to the shortcomings of using sum-of-squares to identify parameters from hysteresis loops. These methods will be discussed in detail in Section 2. A new algorithm to calculate the area between curves is proposed and compared with other measures of similarity from literature. The area algorithm is compared to the discrete Fréchet distance, Dynamic Time Warping (DTW), Partial Curve Mapping (PCM), and a Curve Length based objective function. The measures of similarity are minimized on simple problems where it is impossible for the model to match the data exactly. Additionally, these measures are used as the objective function in an inverse analysis to determine material parameters for a kinematic hardening transversely anisotropic material model. The resulting FE models replicate the experimental data from five hysteresis tension-compression loops. Artificial noise is added to the problems to demonstrate the robustness of the measures to noise, and to help distinguish the measures in an events where it is impossible to match experimental data exactly.

3.2 Methodology

Inverse analysis have been used to identify material parameters for numerical models [6]–[8], [44]–[46], [50], [51]. In general some experiment was conducted on a material (e.g. a load-unload uniaxial test, or tension-compression test). Then a numerical model was created which replicates the physical conditions of the test (e.g. an appropriately constrained FE model). In the case of using a FE model, this process has been referred to as the FE model updating (FEMU) method [52]. An inverse analysis determines parameters of the numerical model by minimizing the difference between experimental data and the response of the numerical model. Optimization is used to find the parameters by minimizing an objective function which describes the quality-of-fit from the collection of parameters. Traditionally the objective function has been based on a sum-of-squares error formulation when using an inverse analysis to find material parameters. This work explores using Partial Curve Mapping (PCM), Area between curves, discrete Fréchet distance, Dynamic Time Warping (DTW), and a Curve

Length objective function proposed by Andrade-Campos, De-Carvalho, and Valente [23] as measures of the similarity between two curves for inverse analyses.

It is important to distinguish between the inverse analyses that require a FE model to continuously update, and non-linear regression problems which parameters are identified from curve fits to experimental data. There are a number of generalized polynomial strain energy models (including Mooney–Rivlin and Ogden hyperelastic material models) which can be identified from curve fits [40]. Additionally, Martins, Natal Jorge, and Ferreira [53] used non-linear regression to determine properties of various hyperelastic models for soft tissues.

There have been a variety of optimization techniques used to solve inverse analysis and non-linear regression problems, including both stochastic and deterministic optimization methods [54]. The focus of this work is to present a collection of objective functions that may be particularly useful when performing an inverse analysis to identify material parameters from hysteresis loops. Thus any optimization technique could be used, assuming the result is close to the global optimum. It is worth to note that different optimization techniques which appear to solve some inverse analyses well, may struggle on other particular inverse problems as principle of the No Free Lunch theorem [11]. LS-OPT® [14], a general purpose design optimization and probabilistic analysis toolbox, was used to solve the inverse analyses for this study.

Three problems are proposed and solved in this paper by minimizing the PCM, Area, discrete Fréchet, DTW, and Curve Length measures. The first problem illustrates the differences between these similarity measures and a traditional least squares fit when fitting a line to quadratic data and fitting a line to data with an outlier. The second problem is a non-linear regression problem invented to illustrate finding material parameters from a single load-unload cycle. The third problem is an inverse analysis to identify material parameters for a kinematic hardening model. Separate optimizations are performed using either the PCM, Area, discrete Fréchet, DTW, or Curve Length similarity measures as the objective function. The intention is to demonstrate how each measure may be useful when identifying

material parameters. The methodology goes on to describe the PCM, Area, Fréchet, and DTW measures of similarity between two curves. It is important to note that the order of the data points is important for these methods.[1]

3.2.1 Partial Curve Mapping

The Partial Curve Mapping (PCM) method was proposed by Witowski and Stander [55] to identify material parameters with inverse analyses. PCM uses a combination of arc-length and area to determine the similarity between curves, because sometimes the choice of parameters changes the overall curve length. An example of where an experimental curve and numerical curve have different overall lengths is seen in the material tension-compression-tension test of Fig. 3-2. First the arc-length of the shorter curve is imposed onto a section on the longer curve. Then trapezoids are constructed between the curves, and the areas of the trapezoids are summed. This is repeated for 200 or so iterations, as various offsets of the short arc length are imposed on the curve with the longer arc length.[2] Trapezoids constructed between two curves for an arbitrary offset can be seen in Fig. 3-3. The final PCM value is the minimum area from all attempted arc-length offsets.

The PCM algorithm is implemented in LS-OPT and has been used to calibrate a variety of material parameters. Venter and Venter [56] used the PCM method with an inverse analysis to calibrate a hybrid material model capable of reproducing the orthogonal load-unload response for plain woven polypropylene. Hassan, Maqbool, Güner, *et al.* [51] used the PCM method

[1] Initially consider two identical curves discretized by identical data points. All of these measures of similarity would return a value of zero. Now reverse the order of the data points on one curve, and then all of these measures would return a large value.

[2] Arc lengths can be iterated such that for the first iteration the arc length of the longer curve is only considered from the beginning of the data to the end of the arc length on the shorter curve. The next iteration would again consider only the shorter arc length of the longer curve, but only after some offset from the beginning of the longer curve. The process is repeated until an offset is used such that the last data point of each curve is considered.

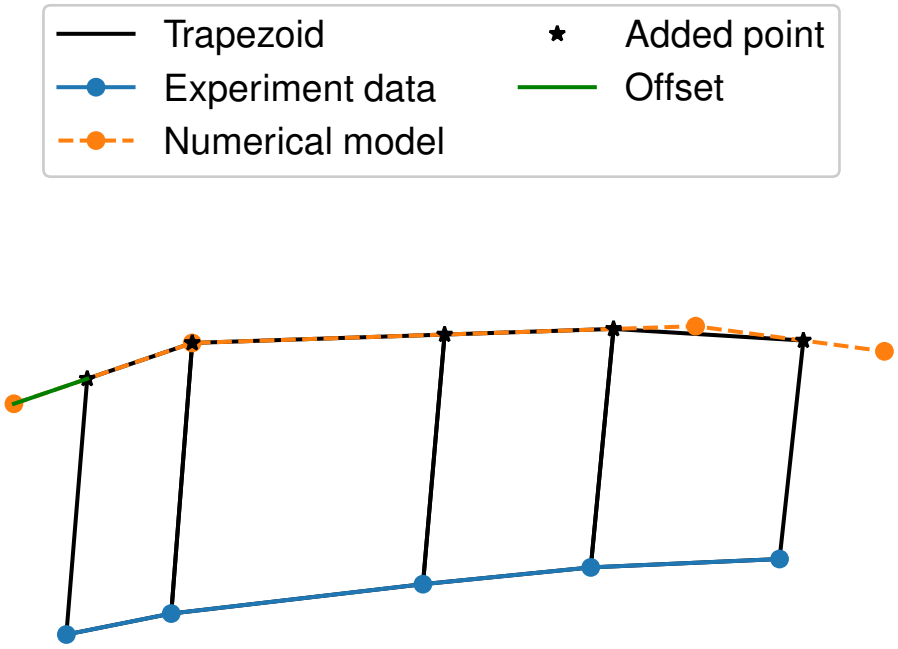

Figure 3-3. The PCM method constructs trapezoids between the two curves for every possible offset.

to calibrate material parameters for the same kinematic hardening model (MAT_125) used in Section 3.3.3. In LS-OPT PCM is referred to as a curve matching algorithm [14].

Though the PCM method has proven a useful tool for material calibration problems, there are some limitations. The PCM method performs poorly when the data has noise, as noise artificially increases the arc length. The LS-OPT manual recommends to reduce noisy data with a filter prior to using the PCM method [14].

3.2.2 Area Between Two Curves

Two curves are generally discretized into a time-series of ordered data points. An algorithm is proposed in this paper to approximate the area between two curves. The algorithm constructs quadrilaterals between two curves and calculates the area for each quadrilateral. The details of the area algorithm is presented in Appendix B.

Two curves that are being compared require the same number of points in order to construct quadrilaterals to approximate the total area between curves. If one curve has fewer data points than the other curve, data points are added until both curves have the same number of data points. It was chosen to add, rather than remove points to avoid any loss of information for general problems. While there are many ways to add artificial data points to the curve, a simple approach was taken which adds an artificial data point by bisecting two points. The location for the bisection was chosen based on the largest Euclidean distance between two consecutive points. Points are added to the curve in this fashion until both curves have the same number of points.

Polygons assume that there is a straight line between any two points. This straight line assumption is important, because adding additional points through the linear interpolation doesn't change the area between the two curves. For instance you can split a pentagon into two quadrilaterals, and the area of the two quadrilaterals will be exactly equal to the area of the pentagon. The adding of additional points is just used to aid in the facilitation of the area approximation. As the number of data points on both curves increases, so does the accuracy of the area approximation.

A simple demonstration of the Area method is shown in Fig. 3-4, where quadrilaterals are constructed between experimental and numerical data. The numerical simulation yields four data points while the experimental data has five points. An artificial data point was added to the numerical data by bisecting the two consecutive points with the largest Euclidean distance, such that both curves have the same number of points. Four quadrilaterals are then created between the curves by taking consecutive pairs from each curve. Since each quadrilateral is a simple quadrilateral, Gauss's area formula is used to calculate the area of each quadrilateral. The quadrilateral areas are summed to give the effective area between curves.

The area between two curves is a positive value ($A \geq 0$). This is true even when the two curves considered cross each other. It is possible for a curve that is slightly above the desired curve to have the same value as a curve that is slightly below the desired curve. Whether

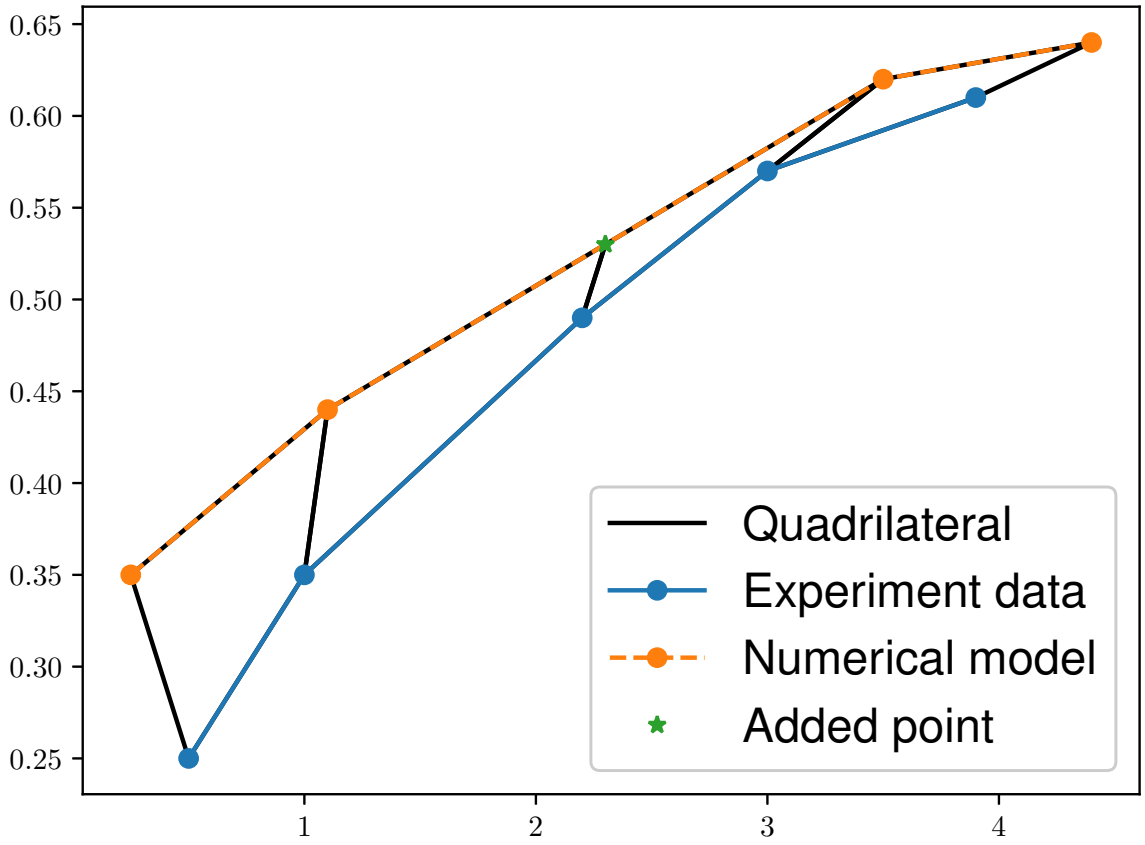

Figure 3-4. The Area between two curves is approximated by summing the quadrilaterals. An artificial point is added to the numerical model, such that both curves have the same number of points.

the curve is over or under the desired curve doesn't matter, however what does matter is the amount of mismatch between the two curves. Minimizing the area between the two curve results in minimizing the amount of mismatch between two curves.

3.2.3 Fréchet Distance

The Fréchet distance is a measure of similarity between curves which preserves the time-series order of data along the curves. The measure was first defined in Fréchet's PhD thesis [57]. Intuitively the Fréchet distance has been described as the length of a leash in a walking dog problem. Suppose a man is walking a dog, where the man is constrained to stay on one curve and the dog on another. The man and dog can vary their velocities independently at all times. Both the man and the dog are limited to either moving forward or stopping along

their curves, as it is forbidden for them to move backwards. The Fréchet distance reflects the shortest possible leash connecting the man and dog sufficient to complete the walk along the curves.

Eiter and Mannila [58] described an algorithm to approximate the Fréchet distance by considering the line segments between the end points of two polygonal curves. This algorithm is referred to as the discrete Fréchet distance, or the coupling distance. If we are to consider a curve P with p number of points and a curve Q with q number of points, the discrete Fréchet distance has a fixed quadratic run time of O(pq). There has been work to reduce the quadratic run time cost of the discrete Fréchet distance [59], [60]. The computational cost is generally not a concern when considering a typical test data, and is only mentioned to understand how the algorithm scales with the number of data points. The discrete Fréchet distance has been used in a variety of applications, including the identification of unique atomistic motions [61].

The difference between the discrete Fréchet distance and the true Fréchet distance is at most the length of the longest edge along the polygonal curves [58]. It is worthwhile to note that algorithms to obtain a more accurate Fréchet distance do exist, but at the cost of additional computational expense. For instance Alt and Godau [62] presented an algorithm that computes the Fréchet distance using a parametric search with a run time of O($pq \log(pq)$). The discrete Fréchet distance was deemed to be a reasonable approximation for this work because the upper bounded error was small with the provided data. The Python MDAnalysis library includes a discrete Fréchet distance function that was used in this work [61].

3.2.4 Dynamic Time Warping

Dynamic Time Warping (DTW) has been a popular method for pattern recognition, and particularly useful for speech recognition [63], [64]. DTW first calculates the distance between points of one curve onto the other curve. If we are to consider a curve P with p number of points and a curve Q with q number of points, for each p point the distance between p and every q point is calculated. This has the same quadratic complexity of O(pq) as the discrete

Fréchet distance. The goal of DTW is to find the path between curves that minimizes the cumulative distance between points.

Imagine traversing the path of both curves simultaneously, where you start from the first index of each curve. The distance between the points at the first index of each curve is your first distance. You are then presented with three choices: (1) move to the second index of curve P, (2) move to the second index of curve Q, or (3) move to the second index of curve P and the second index of curve Q. The second distance will be either the distance between the points of the second indexes, or the distance between the point of the second index on one curve and the first index on the other curve. This process is repeated until you are on the last index of each curve. The optimal DTW distance represents the path with the smallest cumulative distance once you have reached the last index of each curve. To aid in the visualization of DTW consider the arbitrary curves in Fig. 3-5 A. The optimal DTW path is shown in Fig. 3-5 B, where the DTW distance is the value of the tile in the top right (at the last index of each curve).

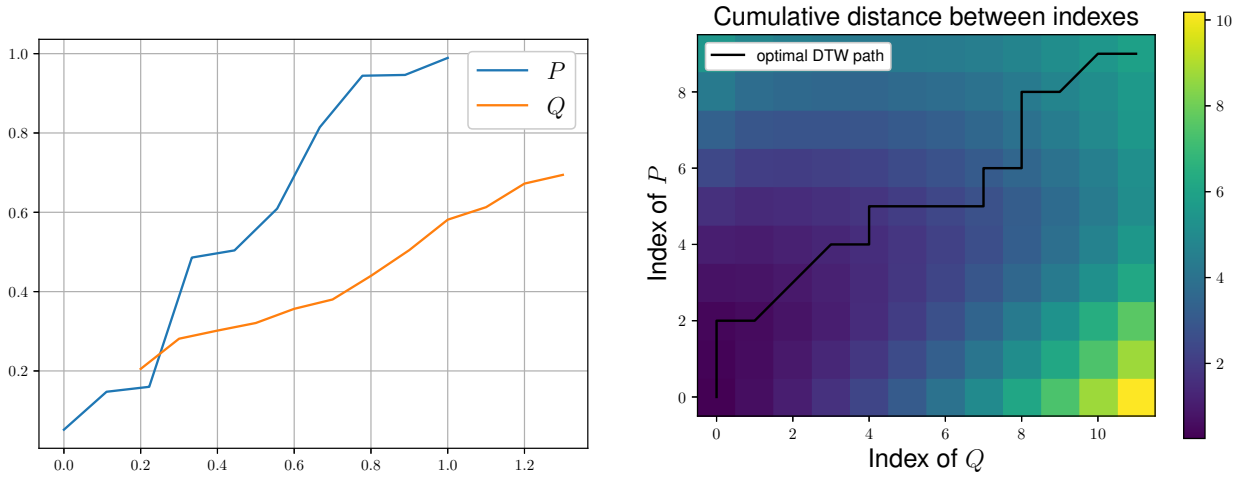

A Consider curve P and Q

B DTW path and cumulative distance

Figure 3-5. Arbitrary curve P and curve Q shown in two dimensions in A) where the optimal DTW path is shown in B) where each tile represents the cumulative distance from the first index of each curve.

The R dtw package was used in this work [65]. In a case where a very large number of points are considered, it may be worthwhile to consider the FastDTW algorithm by Salvador and Chan [66]. FastDTW is a popular approximation of the DTW distance with linear cost, although the reduced computational expense comes at the cost of reduced accuracy. The quadratic computational expense is not a concern for typical hysteresis curves, but it is worthwhile to note how the method may scale provided a very large number of points.

3.2.5 Curve Length

Cao and Lin [22] suggested an objective function with automatic weighting factors to determine material constants that match experimental data. Andrade-Campos, De-Carvalho, and Valente [23] took the objective function of Cao and Lin and extended it to be applicable for negative and zero stress and strain values. Additionally, Andrade-Campos et al. introduced a novel curve length attribute to be included in the objective function to quantify the quality of fit between two curves. The final Curve Length objective function is suitable for identifying parameters for a variety of cases, including cyclic hysteresis tests and Bauschinger tests.

This Curve Length inspired objective function works on the principle that a point on one curve can be compared to its corresponding curve length location on the other curve. Essentially the stress and strain values from a cyclic tension-compression-tension test can be expressed as a function of the curve length distance from the first data point. A data point on the experimental curve will have some curve length distance that can be expressed as a ratio from the total experimental curve length. The stress and strain values from two curves are compared at the same curve length ratios, and an objective function is formulated as the sum of the natural log of these squared deviations.

An illustration depicting this process is provided in Fig. 3-6. A corresponding data point on the numerical model is calculated at the equivalent curve length location of the experimental curve. Squared residual values are then calculated as function of both the dependent and independent variables. The sum of these squared residuals is used to quantify the difference between the two curves.

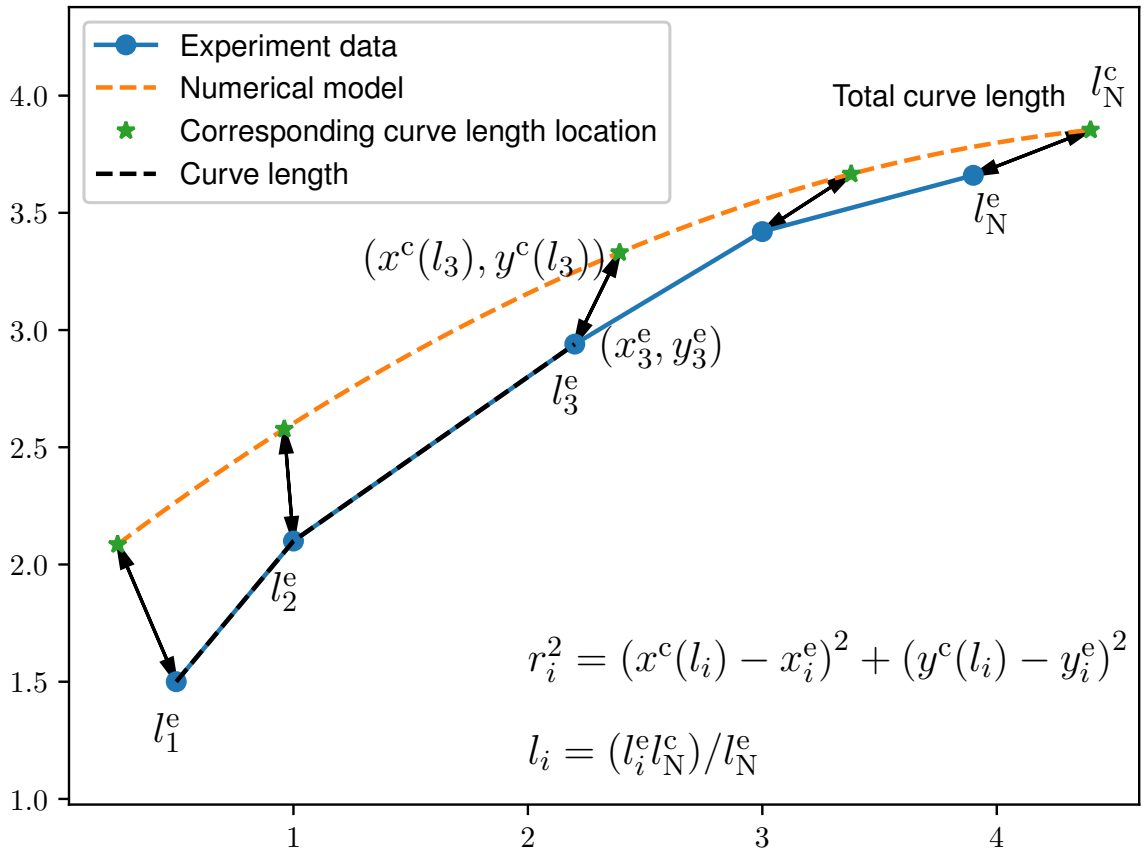

Figure 3-6. Depiction of a Curve Length inspired objective function. The r_i^2 residuals are summed for the N data points to quantify the difference between the two curves.

The implementation of the Curve Length measure used in this work is the OF2 from [23], which was seen to better identify a hyperelastic and elasto-viscoplastic models. This formulation is self-normalizing, and utilizes a natural log transformation. This OF2 objective function is referred to as the Curve Length method throughout this paper.

3.3 Results

The different similarity measures were first compared to minimizing the sum-of-squares to clearly illustrate the difference between methods. The first example fits a straight line to linear data with a single outlier and fits a straight line to quadratic data. Optimization is used to find the best line according to the Area, PCM, discrete Fréchet, DTW, and Curve Length similarity measures.

The similarity measures were then used in optimizations to identify parameters from a single load-unload cycle. This problem was invented for the purpose of illustrating the methods on a simple example. There is a known analytical solution. Having a known solution makes it easier to test both the optimization strategy, and the implementation of each similarity measure.

Lastly, material parameters were identified for a kinematic hardening transversely anisotropic material model. Optimization was used to find the parameters such that the FE models reproduce experimental tension-compression-tension cycles. Test data is from five different tension-compression-tension cycles. The material exhibits stress-strain hysteresis, and the results compare the differences between measures of similarity. To see how the objective functions deal with noise, the inverse problems are solved again with artificially added noise to the desired curves.

In general, it is impossible for numerical models to match experimental data exactly. It is not likely that a material model matches reality perfectly, and even if it does, measurement errors are likely to foil a perfect fit. An outlier, linear model to quadratic data, fitting with noise, and the kinematic hardening problem are just examples of when obtaining a perfect fit is not possible. These examples illustrate how the best model may be dependent upon the similarity measure chosen for many practical problems.

3.3.1 Straight Line Illustrative Fit

In this section a straight line is fit to linear data with an outlier, and to quadratic data using the five measures of similarity. The fits are performed using a global optimization routine. The similarity measures were minimized using the genetic algorithm (GA) implemented in LS-OPT with the default parameters. The GA serves as the global optimization routine to find the best line.

A straight line was fit to ten data points originating from a straight line, with one of the data points being modified to resemble an outlier. The Area, PCM, discrete Fréchet, DTW, and Curve Length similarity measures were minimized to find the line of best fit to the data.

The methods are compared to the line resulting from minimizing the sum-of-squares through a least squares fit. Results from the different similarity measures are presented in Fig. 3-7. The Area and DTW methods entirely ignore the single outlier, as expected between methods that sum the absolute distances (L1 norm). Minimizing the discrete Fréchet distance creates a line that is in-between the outlier and the remaining data points, as can be expected by a method that minimizes the maximum distance (L-infinity norm). Minimizing the PCM method produced a line with a steeper slope than the trend, as the method was accounting for the increased arc-length from the outlier. The sum-of-squares optimum represents a line that is an average preserving compromise between the true trend and the outlier, as expected from an L2 norm. The Curve Length similarity measure produces a line that is initially similar to the sum-of-squares optimum, but dips slightly below the data points at the end.

The results of fitting a line to quadratic data are shown in Fig. 3-8. First a fit was performed to the original data. Then a second fit was performed, where the data was first normalized such that each variable ranged from zero to one. The fits were determined by minimizing the similarity measures with the GA. The discrete Fréchet distance and DTW methods were severely affected by the normalization. Looking at the normalized quadratic data it is seen that the discrete Fréchet distance resulted in a line that was just above the sum-of-squares solution, while the Area and DTW methods result in a line just bellow the sum-of-squares solution. Minimizing the Area and DTW produced the same results when fitting quadratic data or fitting a line with an outlier, as seen in Fig. 3-7 and Fig. 3-8 B). The PCM method resulted in a line with a different slope than the other methods. Normalization is built into the PCM and Curve length methods, so in both cases they resulted in the same fit. Normalization did not appear to affect the Area method as the results with and without normalization were the same.

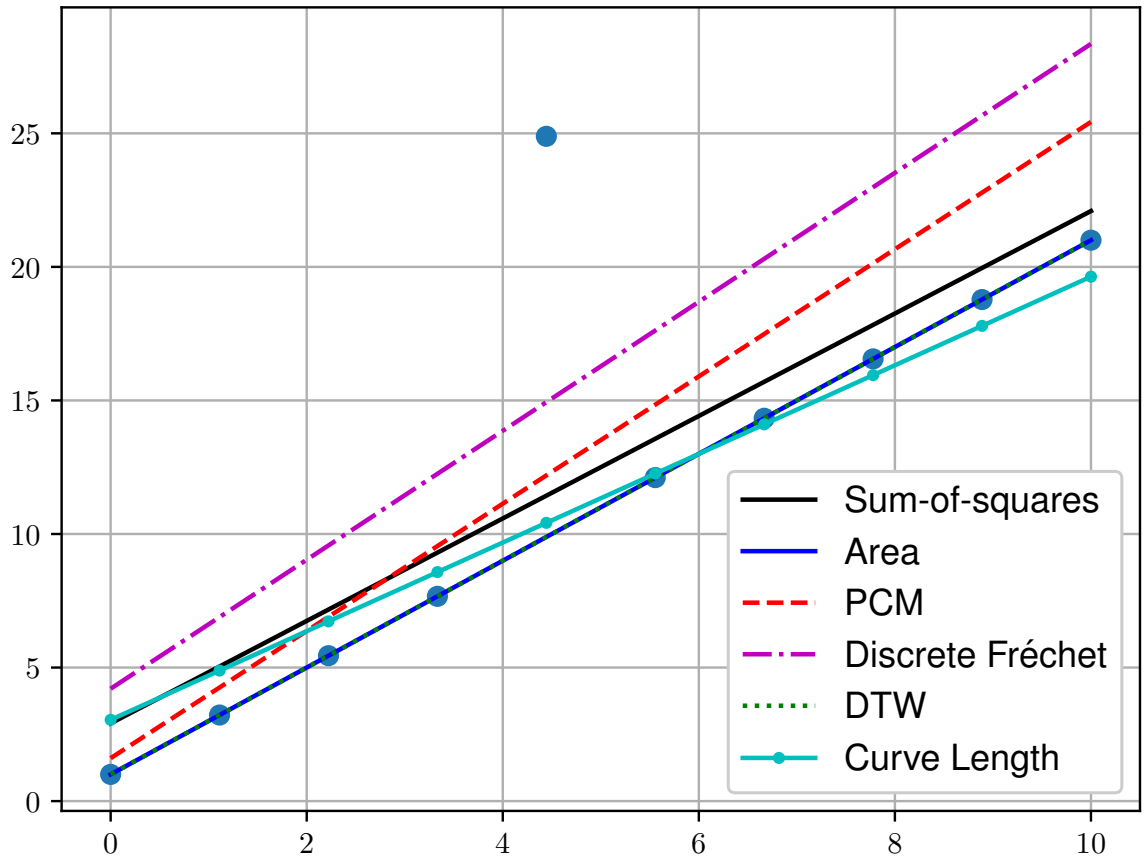

Figure 3-7. Results of fitting a line to linear data with central outlier by minimizing different similarity measures. The outlier was exaggerated to clearly show the differences between similarity measures.

3.3.2 Single Load-Unload Cycle Example

A single load-unload cycle problem is proposed as the following piecewise equation

$$\begin{cases} \exp(\beta_0 x) + \beta_1 & 0 \leq x \leq 1.0 \\ 2.0\exp(\beta_2 x) - 2.0\exp(\beta_3) + \exp(1.0) - 1.0 & 1.0 \geq x \geq 0.62 \end{cases} \tag{3-2}$$

with four unique $\boldsymbol{\beta}$ parameters to identify. This piecewise function with added noise was seen in Fig. 3-1. The true values and optimization bounds of the problem are found in Tab. 3-1. The problem is solved with and without noise. Artificially added noise was generated by taking a randomly sampled array from the normal distribution of $\mu = 0.0$ and $\sigma^2 = 0.05$, and then the array was added to the true response. The noise is added only to the dependent variable

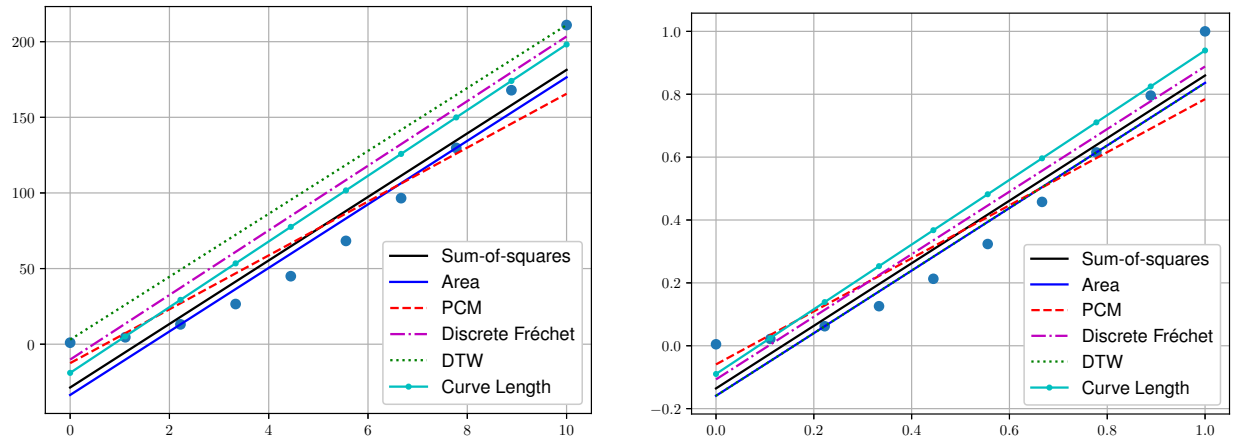

Figure 3-8. Results of fitting a line to quadratic data by minimizing different similarity measures. The original data and results are presented in A), while B) shows the results with normalized data.

($f(x)$), and results in a signal-to-noise ratio (the ratio of the mean to the standard deviation from noise) of 3.33.

Table 3-1. Parameter bounds and true values for the single load-unload cycle example.

Parameter	Lower bound	True value	Upper bound
β_0	0.0	1.0	10.0
β_1	-10.0	-1.0	10.0
β_2	0.0	1.0	10.0
β_3	0.0	1.0	10.0

The genetic algorithm (GA) was used with the default parameters, except for the maximum number of iterations which were increased from 100 to 200, because the optimizations were still improving after 100 iterations. This optimization problem is more challenging in terms of the number of function evaluations required to find a global optimum, than the previous straight line fits. The GA was used to find the optimal $\boldsymbol{\beta}$ terms that minimize the difference between some guess and the true values. The problem is solved by minimizing either the Area, PCM, discrete Fréchet, DTW, and Curve Length methods. The GA iterations are plotted against the objective function values in Fig. 3-9. When there isn't noise, the objective values are still improving at 200 iterations, and presumably heading to the known

zero objective value. However, when noise is introduced we see that all objective functions stop improving around 100 iterations.

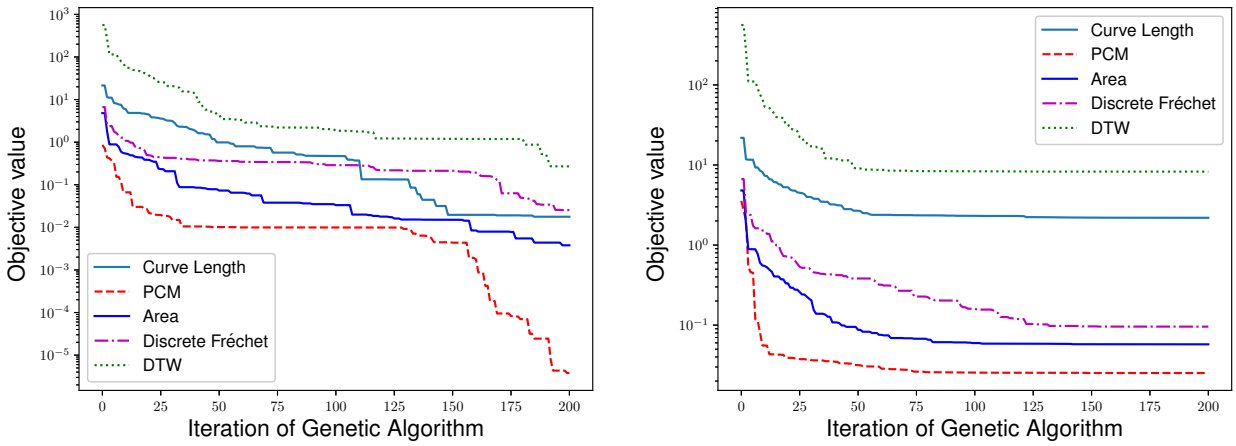

A No noise

B Added noise

Figure 3-9. Plots of the objective values as a function of the iteration of the Genetic Algorithm for the single load-unload cycle example.

All of the objective functions can be minimized to find the true solution. The resulting curves from the best objective functions are shown in Fig. 3-10. However when noise was present in the data the PCM method struggled, as the optimum objective functions from the noisy data are seen in Fig. 3-11. DTW and the Area method produced a response that moves through the center of the data points, which is nearly identical to a response by minimizing the sum-of-squares. The line from the sum-of-squares solution is actually covered up by the lines from the DTW and Area methods. The response from the discrete Fréchet distance moves through the data points, but does not remain in the center of the noise. The PCM method was not capable of finding reasonable parameters with the noisy data. The Curve Length method produced a response that travels on the outer edge of the noise.

The problem with noise is interesting because it is not possible for any of the objective functions to equal zero. Each optimization found their own best objective function (i.e. minimizing DTW resulted in the best DTW value, minimizing PCM resulted in the best PCM value, etc.). Visually some of these resulting curves (Area, DTW, and sum-of-squares) appear to be better fits than the other objective function values. These fits are just the best according

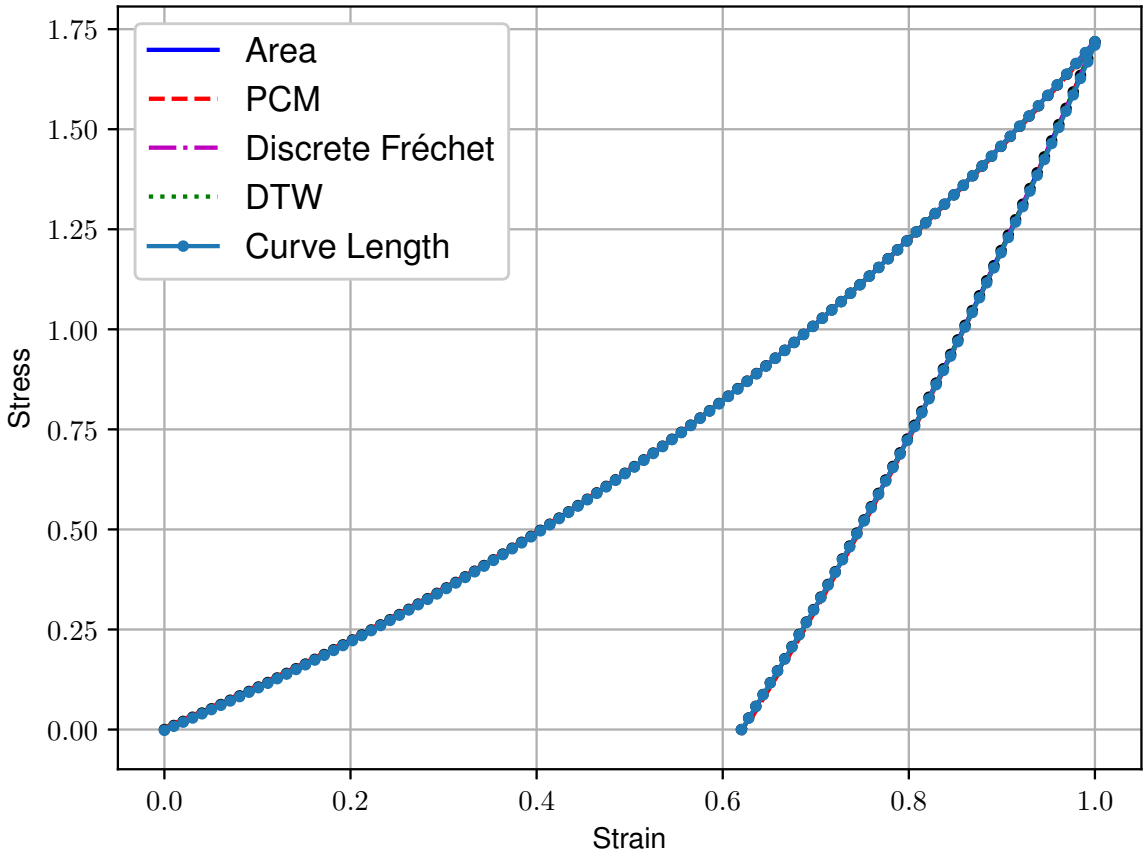

Figure 3-10. The curves resulting from the best found objective function values and the original data.

to the minimized objective function. When it was impossible to obtain a perfect fit, the different measures of similarity produced different results. However, each measure of similarity produced nearly identical results when it was possible to obtain a perfect fit.

3.3.3 Kinematic Hardening Parameter Identification from Five Cycles

The kinematic hardening parameter identification problem used in Witowski and Stander [55] is revisited to compare the performance of the Area, PCM, discrete Fréchet, DTW, and Curve Length methods. The LS-DYNA material model MAT_125 is calibrated using a single element, and the nine unknown material parameters are determined by matching the response of the LS-DYNA model to five experimental hysteresis tension-compression-tension curves. A single objective function is created by summing the similarity measures between the numerical

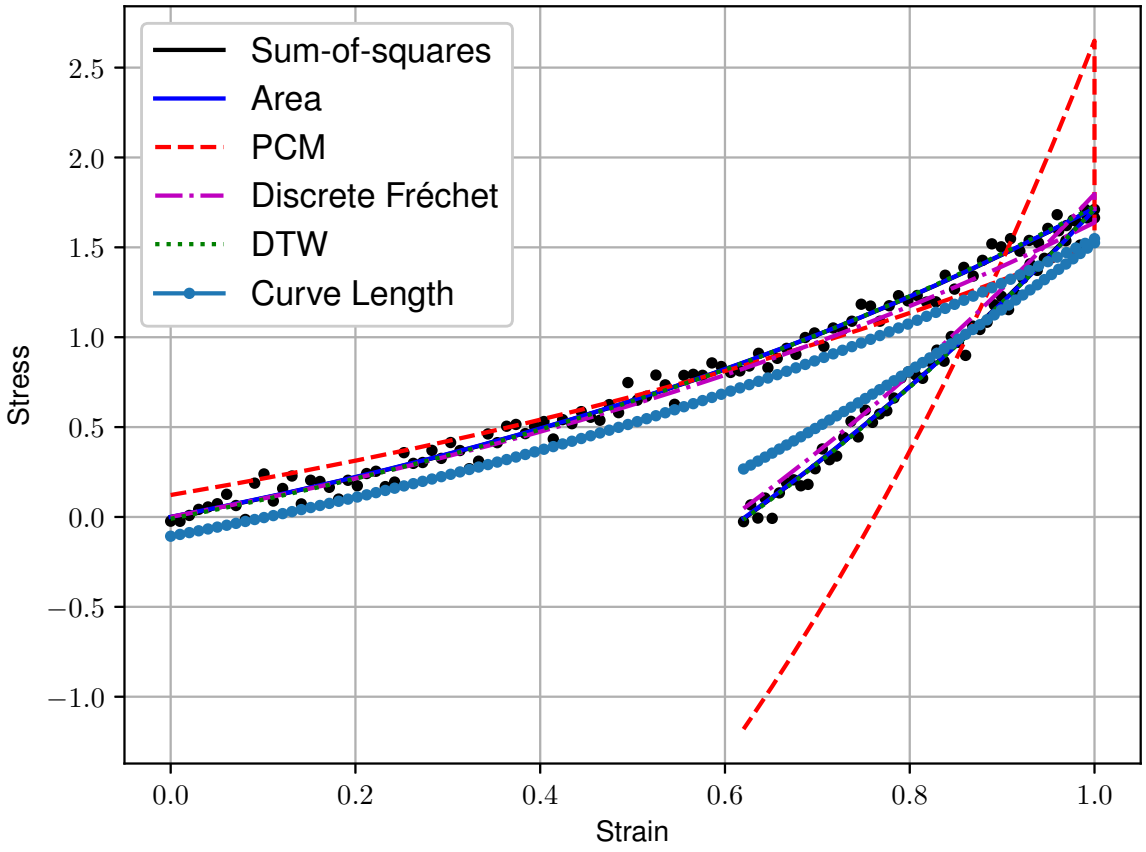

Figure 3-11. Curves resulting from the best found objective function values using the noisy data.

model results and the test cycles. Again ten optimizations are run in total, two for each method. The problem is solved with the experimental curves as is, and with artificially added noise.

MAT_125 is based on the kinematic hardening rule developed by Yoshida and Uemori [48], with the addition of allowing the Young's modulus to vary as a function of the effective plastic strain [67]. The manual recommends to use MAT_125 with an implicit FE model when modeling a metal forming process [67]. The material model is not time dependent, thus comparisons of time from the FE model to quasi-static test data may not be relevant.

The parameters are determined in a two part optimization process in an attempt to find the global optimum. First a metamodel (or surrogate) based optimization using the sequential domain reduction (SDRM) technique is run [12]. The SDRM can find reasonable parameters

after just a few iterations, though it is not guaranteed to find the true global optimum. The optimum from SDRM is then used as one individual (or the starting point) for a genetic algorithm (GA), in hopes that the GA will find the global optimum. The GA terminates when the relative objective function improvement was less than 0.1% for 100 consecutive iterations. This overall strategy requires a large number of function evaluations on multiple non-linear FE models. If the number of function evaluations is a concern, it may be reasonable to consider using just the SDRM to find a good-enough solution for a fixed number of function evaluations. The optimization bounds are presented in Tab. 3-2.

Table 3-2. Parameter bounds for the kinematic hardening material model.

Parameter	Lower bound	Upper bound
CB	500	1000
SIGY	450	600
C	90	300
K	10	35
RSAT	250	550
SB	120	400
H	0.5	1.2
C1	0.01	0.1
C2	0.05	0.5

The optimizations are performed with and without artificial noise to the test data. The noise was added at random from a normal distribution of $\mu = 0.0, \sigma^2 = 35$. The noise is added only to the stress values. The signal-to-noise ratio (consider the mean of the absolute stress value over the standard deviation of the added noise) from the first tension-compression-tension cycle to the last cycle is: 83.1, 105, 117, 127, and 133. These large values suggest that the signal of the hysteresis loop was much stronger than the added noise. It isn't known if this amount of added noise is realistic of an experimental test, but the added noise will provide insight into how the the different similarity measures behave. The added noise represents a case where it is impossible for the numerical model to match the test data exactly. The original test data that was used by Witowski and Stander [55], along with the artificially added noise can be seen in Fig. 3-12.

The data was first normalized for DTW and Discrete Fréchet measures which were shown sensitive to noise in Fig. 3-8. The normalization strategy is similar to the PCM method, which sets the stress-strain values of the test curve between zero and one.

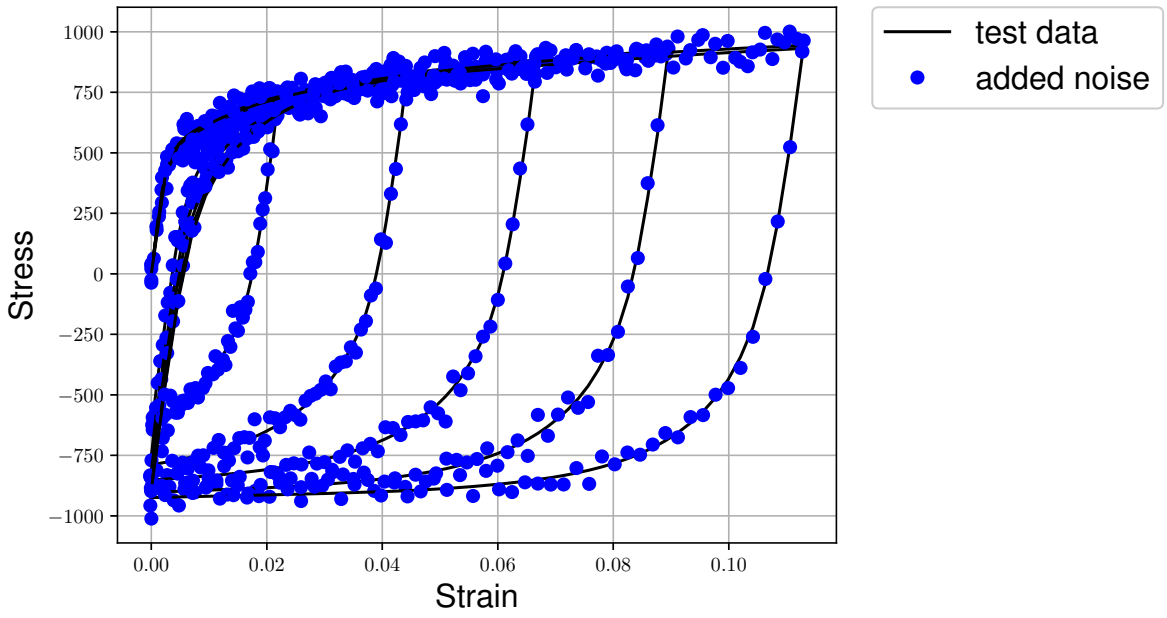

Figure 3-12. The five cycles of the original test data as well as the five cycles with artificially added noise.

The numerical model optima responses are seen in Fig. 3-13, and the results with the added noise in Fig. 3-14. The PCM method was unable to find reasonable material parameters when noise was added to the test data. Though the results of using Area, discrete Fréchet, DTW, or Curve Length as objective functions appears to produce a stress-strain curve that falls within the noise of the hysteresis data. To view the results of individual hysteresis cycles refer to Appendix D. Qualitatively, the results from the Area, DTW, or Curve Length method appear to match the test data the best. While it appears that the Area, Discrete Fréchet, or DTW methods appear to match the test data with added noised the best.

The parameter values found from each optimization are presented in Tab. 3-3. Each method recommended different material parameters with a considerable amount of variation. Additionally, variation is present when comparing the results with noise to the results without noise. There is no clear consensus as to what the best set of parameter values should be.

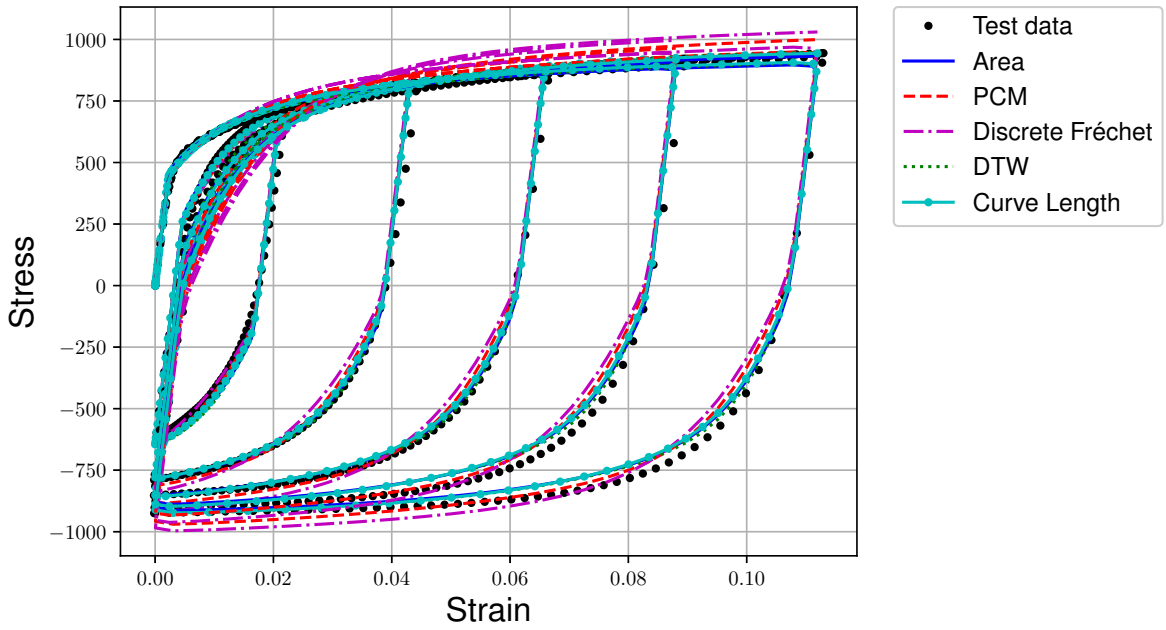

Figure 3-13. Material parameter identification optima for MAT_125 using various measures of similarity.

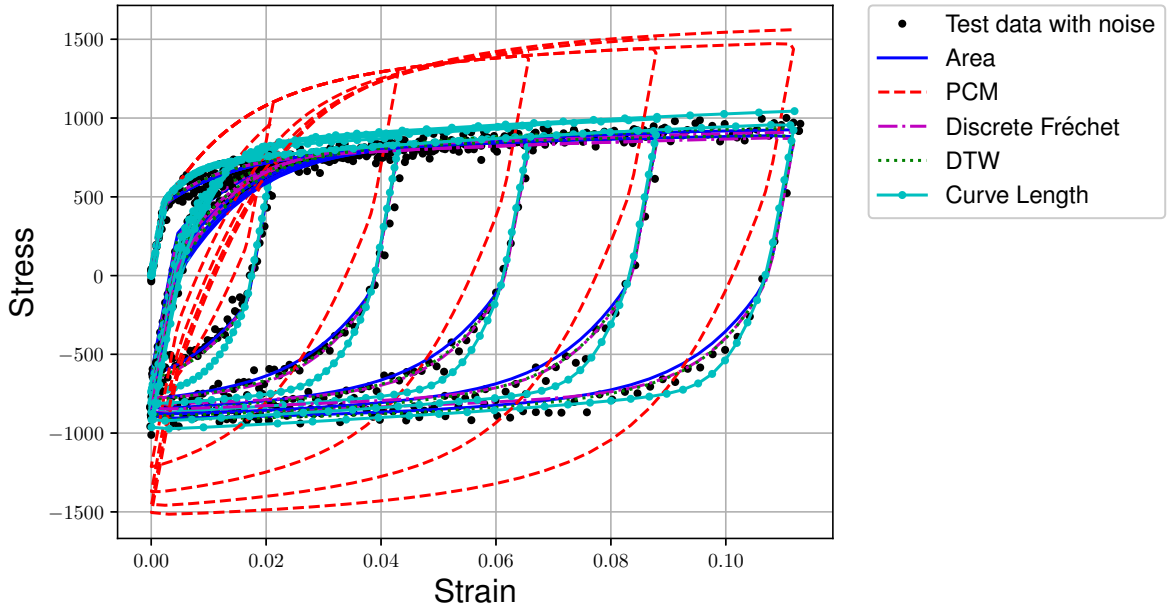

Figure 3-14. Material parameter identification optima for MAT_125 using various measures of similarity when noise was artificially added to the test data.

The resulting optima by minimizing one objective function were evaluated by the other measures of similarity, and presented in Tab. 3-4 and 3-5. Each global optimization was

successful in finding it's own best similarity measure. For the results without noise, the Area, DTW, and Curve Length methods appear to have the most similar objective values.

Line plots between the results of the first SDRM optimization were performed and shown in Appendix C. The line plots indicate whether multiple local optima exist in-between the optima found. Local optima was occasionally found by line plots when considering the cases without added noise (e.g. Fig. C-1 A). In general there were fewer local optima (indicated by line plots) when considering the hysteresis loops with artificially added noise.

Table 3-3. Parameters determined from minimizing different objective functions for the kinematic hardening problem. Values at a lower or upper bound do not imply that the similarity measures produce similar material parameters.

Objective function	CB	SIGY	C	K	RSAT	SB	H	C1	C2
without noise									
Area	629	467	160	35	414	196	0.54	0.01	0.12
PCM	687	450	127	24	508	174	0.56	0.01	0.15
Fréchet	763	454	93	23	481	123	0.89	0.02	0.21
DTW	604	451	202	35	493	209	0.50	0.01	0.12
Curve Length	619	451	173	35	389	215	0.51	0.01	0.13
with artificially added noise									
Area	678	450	119	28	328	143	0.50	0.01	0.17
PCM	1000	450	132	35	550	343	1.19	0.01	0.29
Fréchet	720	450	132	11	421	120	0.89	0.02	0.18
DTW	642	451	164	35	407	166	0.50	0.01	0.15
Curve Length	695	472	300	10	550	190	1.19	0.01	0.41

Table 3-4. Without noise: Objective function values from different optimizations on the kinematic hardening problem. The first column of a row indicates what objective function was minimized by the optimization, while the other columns indicate the other objective function values.

Optimization objective	Method value				
	Area	PCM	Fréchet	DTW	Curve Length
Area	45.1	6.3×10^{-3}	0.36	22.5	4.4
PCM	59.7	3.3×10^{-3}	0.37	27.9	7.5
Fréchet	78.3	4.5×10^{-3}	0.34	35.8	10.7
DTW	45.5	5.7×10^{-3}	0.36	21.7	4.6
Curve Length	45.5	4.9×10^{-3}	0.36	22.6	4.3

Table 3-5. With added noise: Objective function values from different optimizations on the kinematic hardening problem. The first column of a row indicates which objective function was minimized by the optimization, while the other columns indicate the other objective function values.

Optimization objective	Method value				
	Area	PCM	Fréchet	DTW	Curve Length
Area	119.0	1243.8×10^{-3}	0.42	30.2	29.2
PCM	434.1	832.1×10^{-3}	1.59	176.2	50.3
Fréchet	123.7	1248.3×10^{-3}	0.40	30.6	28.7
DTW	120.8	1208.6×10^{-3}	0.44	28.7	28.2
Curve Length	150.6	1062.2×10^{-3}	0.59	47.0	24.9

The results without noise did not find parameters for the MAT_125 model which result in a zero objective function value. An additional optimization was run by picking a known set of MAT_125 parameters, and setting the test data to be the result of the FE models from these known parameters. The SDRM optimization produced stress-strain curves that resembled virtual test data. Then when the GA was used to improve upon the SDRM results, it was observed that all objective values were heading to zero. If a perfect fit exist, then any of the measures of similarities can be used to identify the parameters.

A five fold cross validation (CV) study was performed on the kinematic hardening parameter identification problem while trying to determine the differences between similarity measures. This means that the inverse problem was solved using four of the five hysteresis loops, and then validated on the remaining hysteresis loop. The processes was repeated five times such that each loop was used as the validation once. Only the SDRM optimization method was used, because of computational cost restrictions. When these five fold CV results were compared with the initial SDRM results, it was observed that not including a hysteresis loop as data in the inverse problem resulted in material parameters that aren't as good at matching that particular hysteresis loop.

This kinematic hardening parameter identification problem is used as an LS-OPT training example. The data, models, and optimization routines are available upon request.

3.4 Discussion

The Area, discrete Fréchet, and DTW measures of similarity are similar to traditionally statistical measures of similarity between curves. The discrete Fréchet distance is similar to the maximum error, as both methods (when minimized) are sensitive to outliers. Despite different rationale, the Area and DTW methods are similar to the sum-of-errors (or mean absolute deviation). The Area and DTW methods could be modified to produce analogous results to the sum-of-squares solution. This could be accomplished by squaring the distances in DTW, or by squaring the areas in the Area method. Together these methods are similar to the standard L1 norm, L2 norm, and L-infinity norm with an advantage of being particularly useful for identifying unique hysteresis loops.

It is worthwhile to note that all of the similarity measures would return an objective function value of zero for the exact β parameters when considering noiseless data. For perfect global optimization, there will be a non-zero residual for an imperfect model. There is always the potential that an imperfect model could be be improved with a better physical understanding of the problem (e.g. selecting a better material model, or more appropriate FE model). When the noisy data is considered there will always be a non-zero objective function value. In all examples, the PCM method was more sensitive to the noise than the other methods. The PCM method is known to be sensitive to noise, thus the LS-OPT manual recommends to use a noise filter to pre-process the curve before using PCM. If it was possible to completely filter out the noise, then the results without noise would be identical to the results with noise for all problems.

The discrete Fréchet distance and DTW produced different straight lines when considering the normalized and original quadratic data, as shown in Fig. 3-8. This was a result of the algorithms focusing on removing the distance in the variable that was an order of magnitude larger than the other variable. It is recommended to first normalize stress-strain responses when applying discrete Fréchet distance and DTW as stress can be orders of magnitude larger

than strain. It is worthwhile to mention that normalization is built into the PCM and Curve Length methods by default.

Using partial matching algorithms, such as PCM, may sometimes be preferable to the other measures of similarity. For instance consider a case where the numerical model was only replicating the loading stage of a hysteresis loop. In this case, PCM is the only method that can be applied to find a partial match of just the initial tension section of the hysteresis loop shown in Fig. 3-15. The PCM is the only measure of similarity in this paper that would return a zero value for this partial mapping. Tormene, Giorgino, Quaglini, *et al.* [68] proposed a partial matching DTW strategy that is available in the R dtw package. Partial matching DTW was not covered in this study, but it may be of interest for future work.

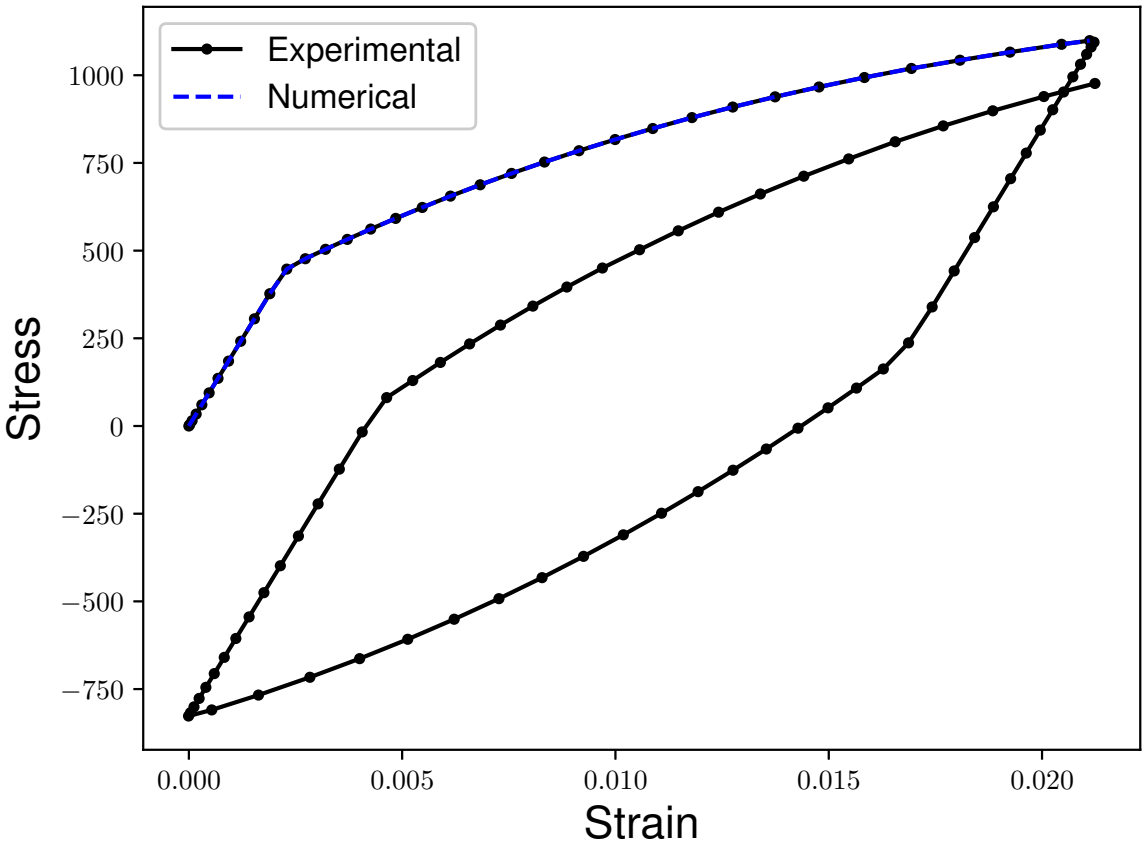

Figure 3-15. Partial mapping example where the PCM objective function value is zero between numerical and experimental curve.

Each measure of similarity presented has its own advantages when being used for parameter identification. The PCM method is capable of matching partial responses. The Discrete Fréchet distance would be useful at reducing the maximum error at any location of two curves. The Area and Curve Length methods appear to have a smoother design space than the other measures when comparing the line plots in Appendix B. It may be preferable to use gradient based optimizations on smooth objective functions which would have fewer local minima than non-smooth objective functions. A qualitative comparison of the objective functions is presented in Tab. 3-6.

Table 3-6. A qualitative comparison of the objective functions covered in this work.

Objective function	Partial matching	Resistance to noise	Resistance to outliers	Function shape
Area	no	good	good	smooth
PCM	yes	poor	poor	non-smooth
Fréchet	no	fair	poor	non-smooth
DTW	see [68]	good	good	less smooth
Curve Length	no	fair	good	smooth

Consider a problem where the data is perfect, meaning that there is no noise and all data points are trusted. All five similarity measures presented will return zero for a numerical model that matched the data exactly. Ideally this would represent a global optimum for the numerical model. If the numerical model was unable to replicate the behavior from just one experimental data point, then each similarity measure may have a unique global optimum recommending a different set of model parameters. The differences in identified parameters would be the result of the interpretation of each similarity measure. A comparison of the measures of similarity for imperfect fits was best illustrated in section 3.1, with Figs. 3-7 and 3-8. This is reasonable motivation to consider multiple similarity measures, as often it is impossible for numerical models to match experimental data exactly. For example, it could be impossible to obtain a perfect match if the numerical model inadequately captured the physics of an experimental response, or if there are errors associated with the experimental response.

3.5 Conclusion

Five different measures of similarity between two curves are presented. The PCM, discrete Fréchet, DTW, and Curve Length measures are from literature. Additionally, a new algorithm is presented to approximate the Area between two curves. These five methods offer advantages over traditional sum-of-square methods, because they don't require the numerical model to be aligned with the experimental data. Additionally they may work particularly well with hysteresis loops, load-unload cycles, or tension-compression tests. These similarity measures can be considered as alternatives to error formulations based on the sum-of-squares, as they help quantify the quality of fit between an experimental and numerical curve. These quantities can be minimized in an inverse analysis to aid in the identification of material parameters. Note that this work assumes that the curves are in a particular time-series order from an initial point to a final point.

When there is no noise present in the data, the results of minimizing either the Area, PCM, discrete Fréchet, DTW, or Curve Length similarity measures produce a reasonable solution. If a perfect fit is possible, any single similarity measure can be used to find the parameters that determine the perfect match. If it is impossible for the numerical model to match the experiment exactly, each method may yield a different solution due to the different physical interpretation of each method. For practical problems it is often impossible to match the experimental data exactly. In these cases, it would be useful to have the best set of parameters from multiple similarity measures. Differences between sets of material parameters may provide an indication of the uncertainty associated with each parameter.

CHAPTER 4
FITTING MATERIAL MODELS TO FULL DISPLACEMENT FIELD BULGE INFLATION TESTS

A methodology is presented to fit material parameters in finite element (FE) models using full displacement field data. Four bulge inflation tests were performed on a PVC-coated polyester material. Digital image correlation (DIC) was used to capture the full displacement field of the material. An inverse analysis was set up to find material parameters in a FE model which replicated the full displacement field of the experimental test. Two different objective functions were considered to quantify the discrepancy between the FE model and test data. One function considered equal weight among displacement components, while the other function weighted the discrepancies to balance different displacement magnitudes. The resulting parameters, for isotropic and orthotropic models, were heavily dependent upon which objective function was chosen. Additionally, cross validation was performed to perform material model selection between the two material models. Similar to the material parameters, the cross validation results preferred different material models depending upon which objective function was being used.

4.1 Introduction

The finite element (FE) method has become an important design tool for membrane structures, and selecting material parameters to represent complex material behavior is a difficult task. This is especially true for the most complex and non-linear materials including coated woven fabrics. Inverse analyses, or iterative schemes for FE model updating (FEMU) have been used to find material parameters from complex load cases. Two different objective functions were investigated when selecting material parameters from bulge inflation tests on PVC-coated polyester. Objective function refers to how the discrepancy between the FE model and test data is quantified, and material parameters are typically selected to minimize this function. The objective function has an important effect on the material parameters selected using this type of inverse analysis.

PVC-coated polyester is a coated textile. It's most commonly modeled as a continuous, homogeneous, orthotropic material [69], which is largely dependent on the warp-to-fill stiffness ratio [70]. The typical weave has the warp yarns pulled taught, while the fill yarns are woven in-between the warp yarns. The fill yarns run orthogonal to the warp yarns. Various non-linear models have been used in an attempt to better describe the behavior of the material. Galliot and Luchsinger [33] proposed a non-linear material model based on the load ratio between the material warp and fill directions. Ambroziak and Kłosowski [34] used a piecewise linear orthotropic model, and Jekel, Venter, and Venter [24] used polynomials to describe the non-linear elastic behavior of the material.

Biaxial tests are commonly used to characterize material parameters for structural membrane materials [71]. Several studies [18], [19], [72], [73] have used bulge (or bubble inflation) tests to induce an equal biaxial load on the material. These bulge tests typically involve inducing a pressure on one side of a circularly clamped membrane material. The equal biaxial load occurs at the apex of the deflected membrane for an isotropic material. The measured pressure and displacements are then used to infer material parameters, by comparing the results to a FE simulation.

A variety of applications [20], [21], [74] have used Digital image correlation (DIC) as non-invasive deformation measuring technique. The technique uses the correlation between consecutive images, from multiple cameras, to calculate a full 3D displacement field. For bulge tests, DIC is an ideal tool to obtain a full 3D displacement field while not interfering with the inflation or deflection of the membrane material.

Material parameters in various models have been identified using FEMU [2], [5], [75]. The process can be generalized by using optimization to find parameters in a FE model that minimize the discrepancy between the model and experimental data. In a forward problem parameters can be directly inferred from an experimental test. While an inverse problem iteratively updates the FE model to find parameters that lead to responses that resembles the experimental response.

This work also investigates using cross validation to select the best material model when performing FEMU. The idea is that cross validation could be used to determine whether the isotropic or orthotropic material model generalizes the PVC-coated polyester better in the complex load case. This is especially important for PVC-coated polyester, which is not a homogeneous (or continuous) material, but modeled as one in the FE method. Cross validation was performed using the two different objective functions described to select material parameters from the experimental data.

The previous studies [72], [73] used only the height to determine material parameters from bulge inflation tests. Machado, Favier, and Chagnon [18] used curvatures to determine a stress tensor from bulge inflation tests to infer material parameters for an elastic material. While these previous methods work well for a planar isotropic material, they are difficult to extend to a directional dependent woven textile like PVC-coated polyester. Jekel, Venter, and Venter [76] showed that it was possible to use the displacement field of a bulge test to select parameters for a non-linear orthotropic material model using simulated experimental data. Jekel [77] then used this process on polynomial displacement fields fitted to experimental data at selected inflation pressures. These polynomial surfaces introduce an extra layer of error in the material parameters. This work will find material parameters by fitting the full experimental displacement field directly. A new approach is describe which allows for any data point in the experimental displacement field be compared to a FE model, for any initial surface location and inflation pressure. While [76] considered the discrepancy in the x, y and z displacements fields to be equal weight, this work shows that substantially different orthotropic parameters occur when less importance is given to the z discrepancies.

4.2 Methods

Bulge inflation tests were performed using DIC on PVC-coated polyester.[1] A FE model was created to replicate the boundary conditions of the bulge inflation tests. Two different objective functions are described. Each objective function represents a different method to quantify the difference between the experimental data and FE model. The process to perform the inverse analysis is briefly described. Cross validation is also discussed as a method for selecting material models in this scheme.

4.2.1 Experimental Tests

The bulge inflation tests involve clamping a sample of membrane material into a circular clamp. Pressure is then induced on one side of the material. The material deflections were recorded using DIC. The DIC system used was the StrainMaster with DaVis [37], which was capable of syncing the inflation pressure with the recorded images. A visual representation of a bulge inflation test is provided in Figure 4-1.

Four bulge inflation tests were performed at Stellenbosch University in South Africa. Details of the process and test fixture are found in section 5.1 of [77]. The diameter of the circular bulge test was 200 mm. The PVC-coated polyester tested was Mehler Texnologies VALMEX® 7318 (the same material in Chapter 2). Four samples of material were cut from the same roll, with each sample being a 250 mm square. Spray paint was added to the surface of each specimen, with a random pattern, to increase the surface contrast of the material for DIC processing. Each test was inflated from zero to three bar, by manually opening a compressed air valve to the bulge inflation test fixture. This resulted in each test being inflated at a unique load rate as seen in Figure 4-2. The internal pressure was recorded with a Festo SPTE-P10R-S4-V-2.5K pressure transmitter.

[1] An online repository is available at https://github.com/cjekel/inv_bubble_opt which includes the source code to perform the inverse analysis, test data, and procedures to reproduce this work.

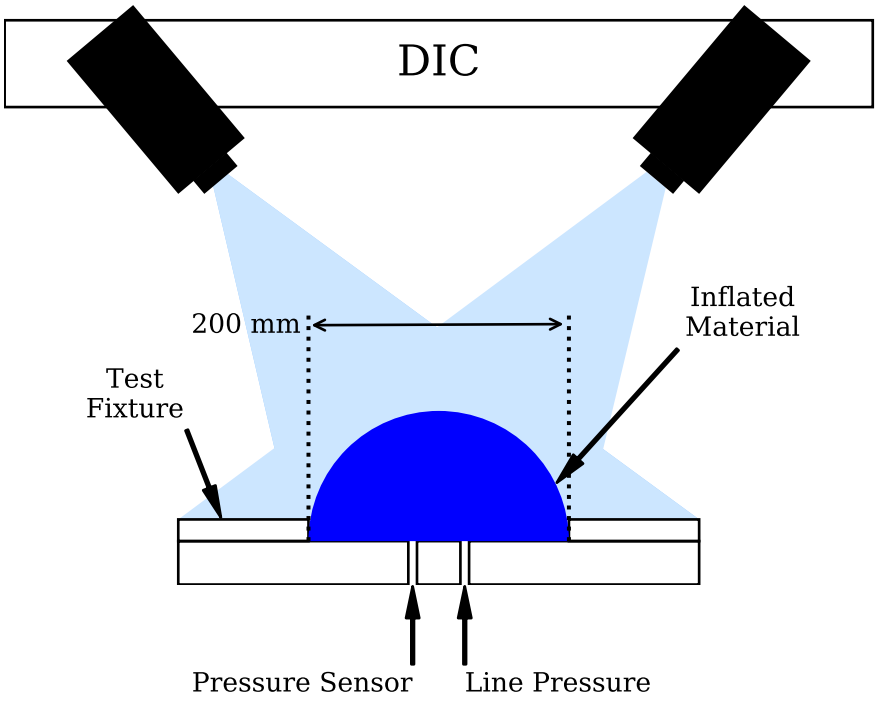

Figure 4-1. Bulge inflation test overview.

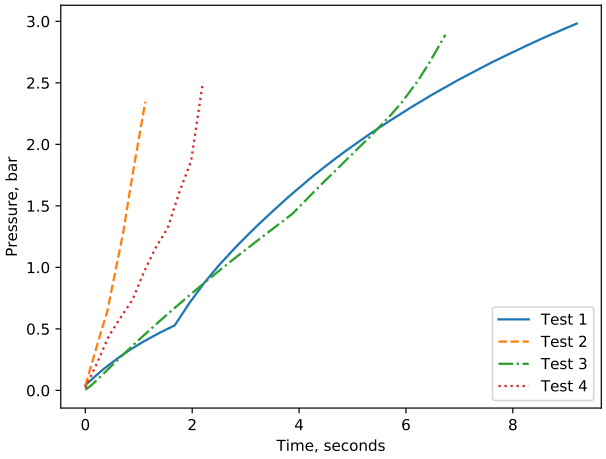

Figure 4-2. Pressure time curves from each bulge inflation test.

Full field bulge inflation tests generated a large amount of data as shown in Table 4-1. The xy-plane was oriented with the surface of the material prior to inflation, with the x direction occurring in the warp material direction, while the y direction occurred in the fill material direction. The material was inflated in the z direction. The number of data points

Table 4-1. Number of unique (x, y, p) data points from each test and inflation pressures.

Test	# of data points
1	1,836,961
2	729,718
3	1,201,509
4	289,312

ranged from test to test. The variation was largely dependent on how finely the DIC data was processed. Here the largest test generated nearly two million data points, while the smallest test generated only two hundred thousand data points. Each data point represents a unique combination of inflation pressure p and initial x, y location. There are three deformations recorded for each data point, represented as separate $\Delta x, \Delta y$, and Δz values.

The DIC techniques were not perfect, as there are missing data points in some of the test. This happens when correlations is lost between images, and becomes more evident with larger deflections. Additionally, the severity of missing data varies from test to test. Figure 4-3 shows each x, y data point at the last inflation pressure of each test, where each colored pixel is a DIC data point. The spacing of the x, y data points vary from test to test as a result of different DIC processing While Tests 1 and 2 have the highest density of data points, Test 1 doesn't have any missing data points while test 2 has several small holes on the surface of the material. The worst of the missing data occurs with test 3, which has large holes on one quarter of the test. Test 4 only has two small holes on the surface of the data, and also has the least number of x, y data points on the surface of the material.

4.2.2 Finite Element Model

An implicit non-linear FE model was constructed in ABAQUS which resembled the physical boundary conditions of the bulge inflation test. Sheplak and Dugundji [78] described differential equations to solve for the displacement field of bulge inflation tests for isotropic and orthotropic material models, but [78] was not used as the geometry is simple enough to quickly construct in any non-linear FE code. The FE model uses an implicit solver, with 201 load steps between zero and three bar. Each load step uses adaptive time stepping. The adaptive

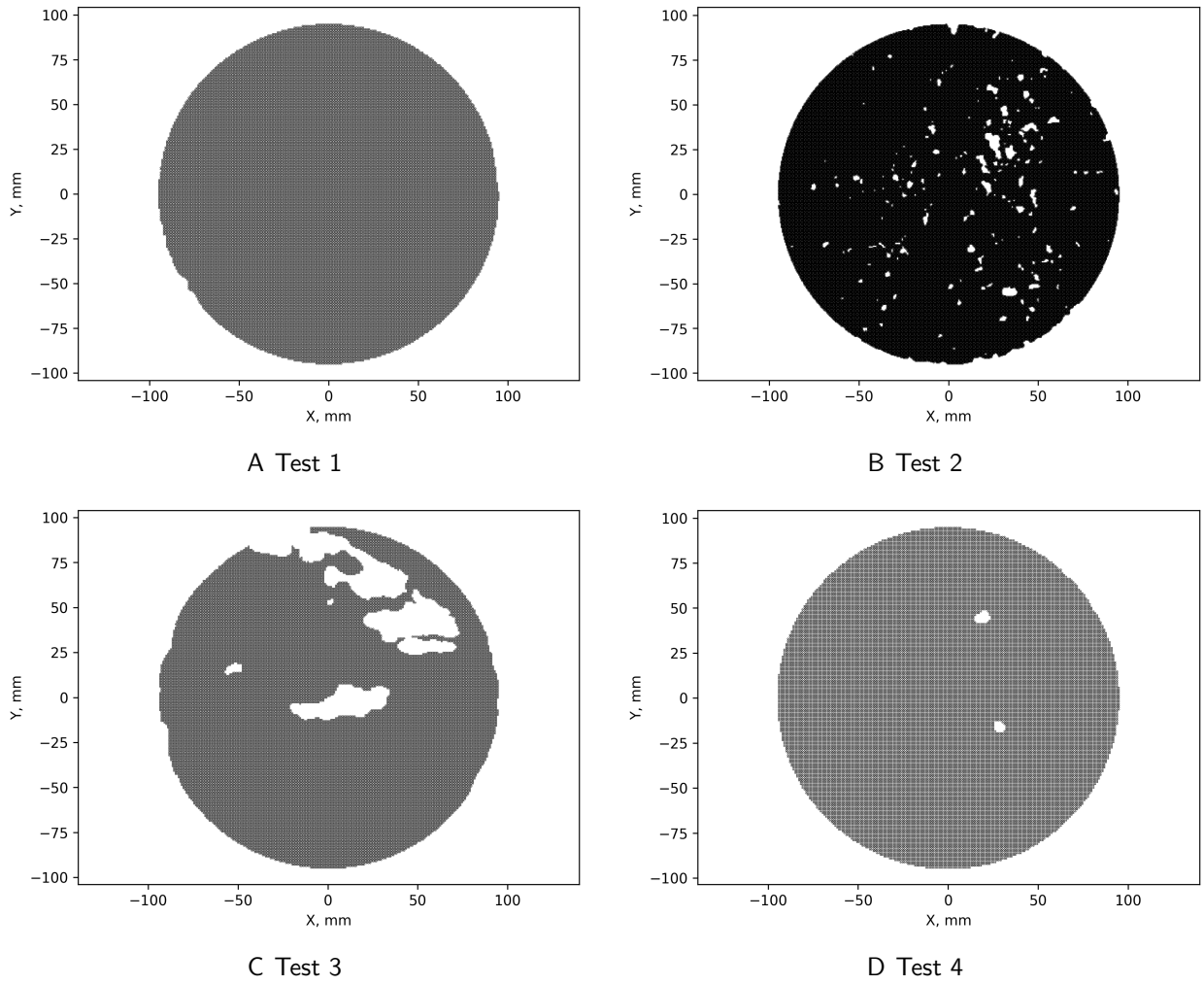

Figure 4-3. Plots of the x, y data points of each bulge inflation test. The darker color is related to having a higher density of data points.

time stepping allows the model to solve a single load-case in one step, or cut back to smaller increments if needed. Over 900 linear Q4 membrane elements are used to represent the surface of the material. The linear elements prevent nonphysical out-of-plane force imbalances. The displacement field at the nodes of the FE solver are exported to be used in further calculations when the model is run with a given material model.

The displacement field of the FE model needs to be computed several times at various pressures which correspond with the pressures of the experimental data. Either load steps can be added to the FE model at the exact experimental pressures, or the displacement field of the FE model can be interpolated to match the exact experimental pressures. Interpolation

was chosen since it didn't involve manually editing the input deck for each test, and resulted in a fixed number of exported displacement fields. Specifically linear interpolation was used to evaluate the FE model's displacement at the nodes for the exact pressures of the experimental test. Linear interpolation is use to solve the displacement field $\Delta(x, y, p)$ by interpolating the displacement field at the two nearest pressures as

$$\frac{\Delta(x, y, p) - \Delta(x, y, p_1)}{p - p_1} = \frac{\Delta(x, y, p_2) - \Delta(x, y, p_1)}{p_2 - p_1} \tag{4-1}$$

where p_2 and p_1 represent the nearest pressures of the FE models' load steps.

Overall, the linear interpolation scheme proved very accurate when interpolating between the FE model load steps. The linear interpolation accuracy was compared to FE models with load steps halfway in-between the previous 201 load steps (representing the worse possible interpolation case). The linear interpolation error was negligible, with the interpolation error following on the order of single precision (10^{-8} mm) numerical noise. This level of single precision was the same level of precision used by the FE model.

Linear isotropic and orthotropic material models were investigated. An isotropic model with one unknown parameter (stiffness modulus E), and an isotropic model with two unknown parameters (stiffness modulus E and the shear modulus G) were considered. The orthotropic model was simplified as a three parameter mode, with parameters for the stiffness moduli (E_1 & E_2), and the shear modulus (G_{12}). The one parameter isotropic model and the orthotropic model use a Poisson's ratio of 0.24 as measured in Chapter 2. Using a constant Poisson's ratio simplifies issues with gradient magnitudes, as it is anticipated that gradients of Poisson's ratio could be orders of magnitude different than stiffness moduli.

The displacement field of the FE model for an orthotropic material model at 2.0 bar is shown in Figures 4-4 through 4-6. The maximum Δz value is about ten times larger than the Δx or Δy values. Radial Basis Functions (RBF) are used to interpolate the displacements from the initial (x, y) node locations at each outputted pressure. The RBFs are exact at the node locations, and result in a smooth displacement field from the linear four node FE elements.

The InterpolateSimpleRBF object construct these RBFs to the full displacement field of the FE analysis. The RBFs were inspired by the SciPy rbf function [79].

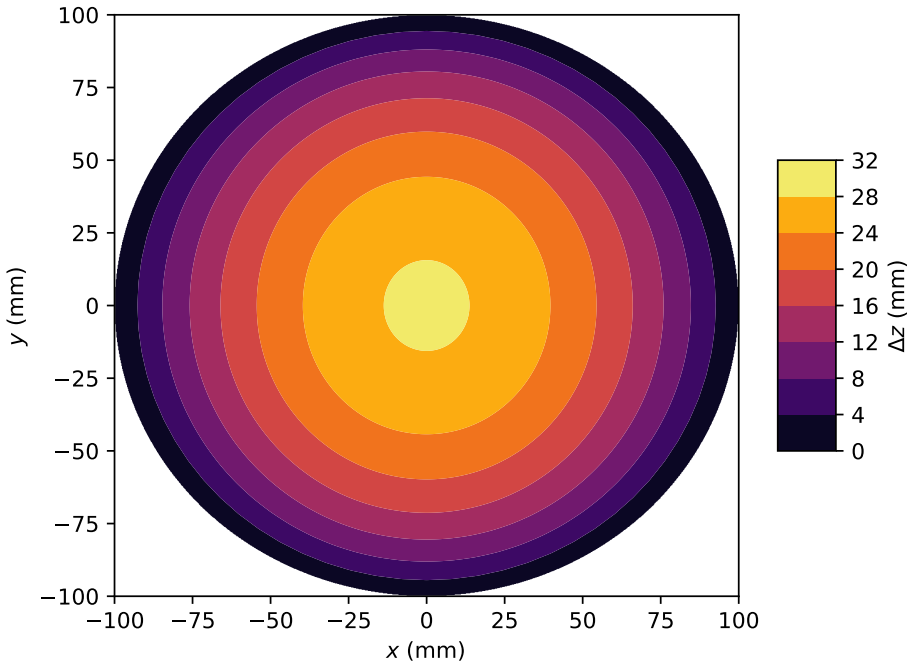

Figure 4-4. Displacement Δz of FE model at 2.0 bar with orthotropic properties $E_1 = 0.8$ GPa, $E_2 = 0.15$ GPa, $G_{12} = 0.025$ GPa, and $\nu_{12} = 0.24$.

The radial basis functions are expressed as

$$\boldsymbol{y} = \boldsymbol{A}\boldsymbol{\lambda} \tag{4-2}$$

where

$$\boldsymbol{A} = \begin{bmatrix} ||\boldsymbol{x}_1 - \boldsymbol{x}_1||_2 & ||\boldsymbol{x}_2 - \boldsymbol{x}_1||_2 & \cdots & ||\boldsymbol{x}_n - \boldsymbol{x}_1||_2 \\ ||\boldsymbol{x}_1 - \boldsymbol{x}_2||_2 & ||\boldsymbol{x}_2 - \boldsymbol{x}_2||_2 & \cdots & ||\boldsymbol{x}_n - \boldsymbol{x}_2||_2 \\ \vdots & \vdots & \ddots & \vdots \\ ||\boldsymbol{x}_1 - \boldsymbol{x}_n||_2 & ||\boldsymbol{x}_2 - \boldsymbol{x}_n||_2 & \cdots & ||\boldsymbol{x}_n - \boldsymbol{x}_n||_2 \end{bmatrix} \tag{4-3}$$

which follows a simple linear kernel [80]. The RBF parameters $\boldsymbol{\lambda}$ are solved for a general input of $\boldsymbol{x}$, output of $\boldsymbol{y}$, with n data points. Then $\hat{n}$ predictions are generated for new $\hat{\boldsymbol{x}}$ locations as

$$\hat{\boldsymbol{y}} = \hat{\boldsymbol{A}}\boldsymbol{\lambda} \tag{4-4}$$

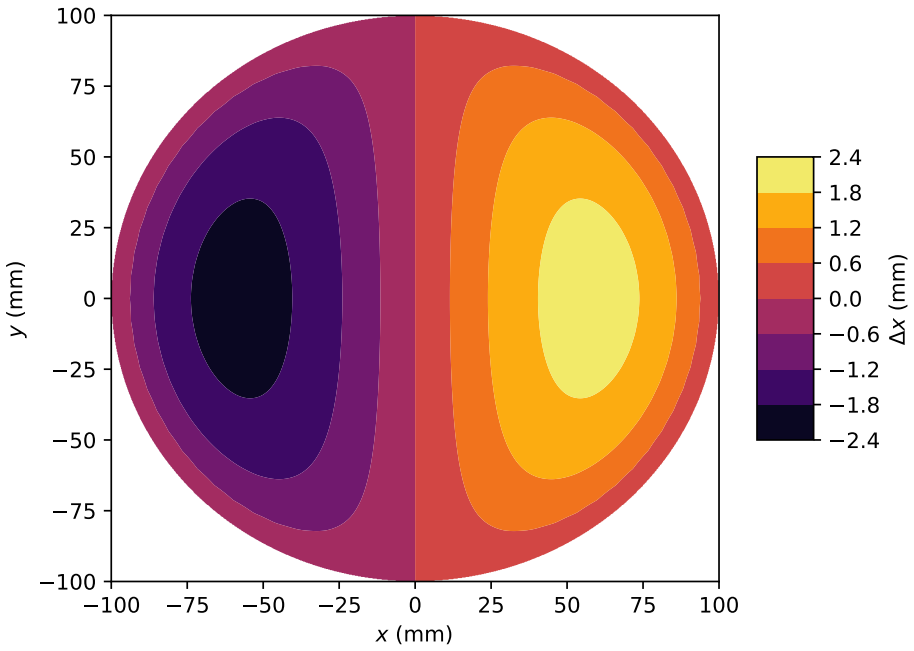

Figure 4-5. Displacement Δx of FE model at 2.0 bar with orthotropic properties $E_1 = 0.8$ GPa, $E_2 = 0.15$ GPa, $G_{12} = 0.025$ GPa, and $\nu_{12} = 0.24$. Note the symmetry about $x = 0$.

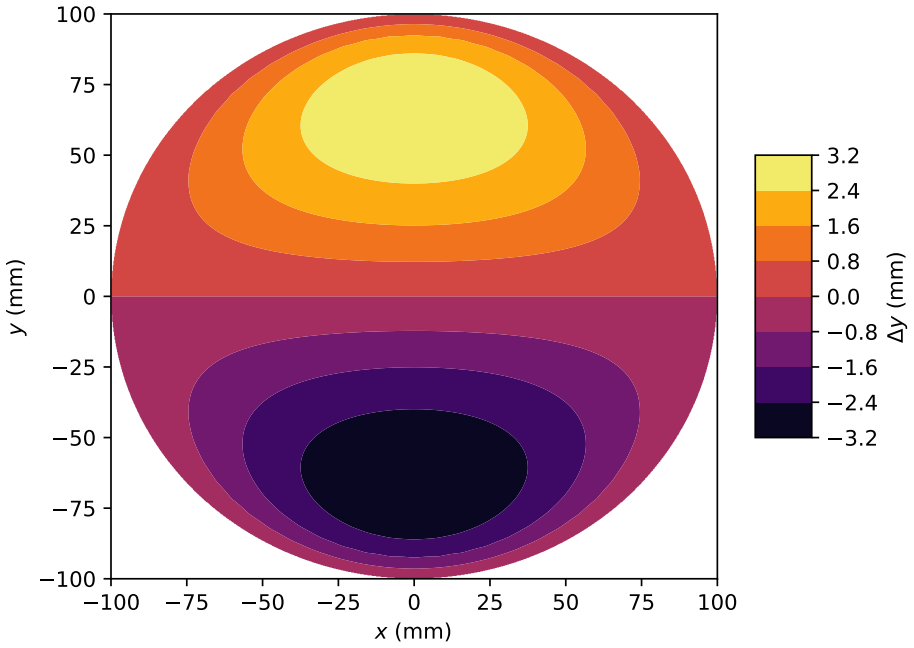

Figure 4-6. Displacement Δy of FE model at 2.0 bar with orthotropic properties $E_1 = 0.8$ GPa, $E_2 = 0.15$ GPa, $G_{12} = 0.025$ GPa, and $\nu_{12} = 0.24$. Note the symmetry about $y = 0$.

where

$$\hat{\boldsymbol{A}} = \begin{bmatrix} ||\boldsymbol{x}_1 - \hat{\boldsymbol{x}}_1||_2 & ||\boldsymbol{x}_2 - \hat{\boldsymbol{x}}_1||_2 & \cdots & ||\boldsymbol{x}_n - \hat{\boldsymbol{x}}_1||_2 \\ ||\boldsymbol{x}_1 - \hat{\boldsymbol{x}}_2||_2 & ||\boldsymbol{x}_2 - \hat{\boldsymbol{x}}_2||_2 & \cdots & ||\boldsymbol{x}_n - \hat{\boldsymbol{x}}_2||_2 \\ \vdots & \vdots & \ddots & \vdots \\ ||\boldsymbol{x}_1 - \hat{\boldsymbol{x}}_{\hat{n}}||_2 & ||\boldsymbol{x}_2 - \hat{\boldsymbol{x}}_{\hat{n}}||_2 & \cdots & ||\boldsymbol{x}_n - \hat{\boldsymbol{x}}_{\hat{n}}||_2 \end{bmatrix}. \tag{4-5}$$

For this problem, $\boldsymbol{x}$ refers to the in-plane (x, y) location of the FE model nodes, $\hat{\boldsymbol{x}}$ refers to the in-plane (x, y) location of the DIC data, $\boldsymbol{y}$ denotes the displacement from the FE model, and $\hat{\boldsymbol{y}}$ represents the experimental displacements. This type of RBF is ideal for interpolating surfaces of FE models since it is exact at node locations, and results in a smooth interpolation in-between the FE node locations.

4.2.3 Objective Functions

The objective function which quantifies the discrepancy between the physical bulge inflation tests and the FE model difference is fundamental for the optimization in the inverse analysis. The average absolute deviation between the x displacement of the FE model and inflation test is denoted $r_{\Delta x}(j, \boldsymbol{\beta})$ for the j test and $\boldsymbol{\beta}$ set of material parameters. These average absolute deviations are expressed as

$$r_{\Delta x}(j, \boldsymbol{\beta}) = \frac{1}{n_j} \sum_{i=1}^{n_j} |\Delta x(x_i, y_i, p_i)_t - \Delta x(x_i, y_i, p_i, \boldsymbol{\beta})_f| \tag{4-6}$$

$$r_{\Delta y}(j, \boldsymbol{\beta}) = \frac{1}{n_j} \sum_{i=1}^{n_j} |\Delta y(x_i, y_i, p_i)_t - \Delta y(x_i, y_i, p_i, \boldsymbol{\beta})_f| \tag{4-7}$$

$$r_{\Delta z}(j, \boldsymbol{\beta}) = \frac{1}{n_j} \sum_{i=1}^{n_j} |\Delta z(x_i, y_i, p_i)_t - \Delta z(x_i, y_i, p_i, \boldsymbol{\beta})_f| \tag{4-8}$$

where n_j is the total number of data points in the j test. A simple discrepancy is then formulated as the average L_1 distance in mm as

$$e(\boldsymbol{\beta}) = \frac{1}{n_t} \sum_{j}^{n_t} r_{\Delta x}(j, \boldsymbol{\beta}) + r_{\Delta y}(j, \boldsymbol{\beta}) + r_{\Delta z}(j, \boldsymbol{\beta}) \tag{4-9}$$

where n_t is the total number of tests. The subscripts t is for the physical inflation test data, while the subscript f is from the FE model.

The formulation of e considers the discrepancy in the x, y, and z directions to have an equal weight. This formulation could be problematic if the discrepancy in one displacement components dominates the others. In the bulge inflation test data, the Δz component was roughly ten times larger than the in-plane (x or y) components. This creates the potential for the $r_{\Delta z}$ discrepancies to be larger than the other two directions, because the Δz values have the potential to be at least ten times larger than Δx or Δy.

A second objective function is proposed as e_w to deal with the imbalance between the maximum in-plane and out-of-plane displacements. The function is just a slight modification of e, and is expressed as

$$e_w(\boldsymbol{\beta}) = \frac{1}{n_t}\sum_{j}^{n_t} r_{\Delta x}(j,\boldsymbol{\beta}) + r_{\Delta y}(j,\boldsymbol{\beta}) + w r_{\Delta z}(j,\boldsymbol{\beta}) \tag{4-10}$$

where w is a weighting component[2] . While there can be many ways to select w, a simple scheme was chosen as

$$w_z = \frac{1}{n_t}\sum_{j}^{n_t} \frac{\max\left(\Delta x(j)\right) + \max\left(\Delta y(j)\right)}{2\max\left(\Delta z(j)\right)} \tag{4-11}$$

which represents the ratio of the average x and y displacement to the maximum z displacement. This resulted in $w = 0.1$ for the bulge inflation tests in consideration.

Two different objective functions are presented to quantify the difference between the full displacement field of the FE model and DIC tests. One objective function is an average L_1 norm between the x, y, z displacements, while the other function is a relative L_1 which considers the weighted difference between x, y and z displacements. A zero for both functions would indicate that the FE model's displacement field exactly matches the experimental data. This is a similar to the work of Chapter 3 to see how the different objective functions influence the material parameters, since a perfect match will not be possible.

[2] The software available online allows a weight to be specified for each directional component of the displacement field.

The optimization requires the objective function e or e_w to be computed multiple times. There are many steps required to automate this using software, and the process is described in Table 4-2. Several Python functions were created to interface with the the ABAQUS solver and post processor for this application. The function essentially returns e or e_w from inputted material parameters.

Table 4-2. Process to compute the objective function for given material parameters.

Step	Description
1	Write the material model parameters to the ABAQUS input file
2	Run ABAQUS solver on the input file
3	Run ABAQUS post processor to export displacement field of FE model
4	Load the FE displacement field into memory
5	Compute the discrepancy between FE model and DIC data: i) Linearly interpolate the FE model to match the pressures of the bulge test data ii) Construct and evaluate RBFs to the FE model displacement field iii) Compute $r_{\Delta x}$, $r_{\Delta y}$, and $r_{\Delta z}$ for each set of test data
6	Compute the final objective function of e or e_w

4.2.4 Optimization

The inverse analysis is the process of finding the material parameters of the FE model to match the bulge inflation test data. The optimization problem can be stated as

$$\text{minimize:} \quad e(\boldsymbol{\beta}) \tag{4-12}$$

$$\text{subject to:} \quad \beta_l \leq \beta_k \leq \beta_u, \quad k = 1, 2, \cdots, n_p. \tag{4-13}$$

where $\boldsymbol{\beta}$ is the vector of material parameters which are restricted to some reasonable lower and upper bounds. The isotropic parameters are expressed as $\boldsymbol{\beta} = (E)$ or $\boldsymbol{\beta} = (E, G)$, and the simplified orthotropic parameters are expressed as $\boldsymbol{\beta} = (E_1, E_2, G_{12})$. Note that e_w is substituted for e when minimizing the weighted objective function.

The first optimization strategy used a global optimizer with an allocated number of function evaluations. When the global optimizer exhausted the specified budget, a local optimizer was used for final convergence to a local optimum. The global optimization strategy used was Efficient Global Optimization (EGO), which utilized the expected improvement

from a Gaussian process to minimize the function [81], [82]. A variant of the BFGS [83]–[86] gradient based optimization was used as the local optimizer [79], [87]. Initially 50 EGO function evaluations (calculations of e) were performed before switching to the BFGS implementation. A budget of 200 function evaluations for the BFGS appeared to be sufficient at finding a local optimum.

After several runs of the EGO to BFGS strategy, it became evident that the optimizer was failing at finding a global optimum. A multi-start optimization strategy was adopted to better deal with the presence of multiple local minima. The multi-start process ran five BFGS optimizations from different starting points in the design space [88]. Each of the five BFGS runs were limited to either 200 function evaluations, or satisfying the convergence criteria. Converge considered either relative changes in the objective function, absolute changes in the objective function, or gradient magnitude. This multi-start optimization was able to consistently find better optimums than the EGO to BFGS strategy, but at the cost of additional objective functions.

There is the possibility that some combination of material parameters may cause the FE analysis to not converge. This is problematic when the optimization algorithm requires a discrepancy for a particular set of parameters that lead to failed convergence. To deal with this problem, the maximum objective value from the run-time history was passed to the optimization algorithm when the FE analysis failed to converge. Additionally, a discrepancy value of 30 mm was passed if the first function evaluation in a given run failed to converge. This strategy works well with EGO, however it creates a non-differential objective function which can be problematic for gradient based optimization algorithms. There are also problems with the use of a L_1 based objective function, where gradients can vanish when the residual of a single points goes to zero.

While there were a number of potential issues using gradient based optimization with this application, in practice the gradient optimization was able to successfully minimize the objective function. Looking at the optimization history, the FE analysis would only fail to

converge during the line search stage of the gradient based optimization algorithm, and not the finite differences which approximate the gradients. This is less problematic because the gradients were accurate. Lastly, there were no observed issues with the optimization caused by the L_1 objective function.

4.2.5 Cross Validation

Cross validation is a model selection or validation tool used in various regression problems to assess the quality of models [89]. Cross validation provides for a nearly unbiased estimate of the modeling error, and can be used to diagnose overfitting or bias errors. Cross validation can be used to compare the performance of one material model to another in the context of fitting material models with an inverse analysis (FEMU). This may be important in practice when the ideal material model is unknown. In this case, cross validation will be used to quantitatively compare how the linear isotropic and orthotropic material models represent the behavior of PVC-coated polyester from these bulge inflation tests.

The processes proposed is similar to leave-one-out cross validation, and is described in Table 4-3. This cross validation score was computed for both the linear isotropic and orthotropic material models. The model with the lower cross validation score is assumed to be a better generalized representation of the material behavior.

Table 4-3. Process to compute leave-one-test-out cross validation error.

Step	Description
1	Perform optimization without test j
2	Calculate the discrepancy e or e_w on the left-out test j
3	Repeat 1 & 2 for all tests
4	Cross validation score is the average discrepancy e or e_w from the left-out tests

4.3 Results

Inverse analyses were performed on the bulge inflation tests to find material parameters for the linear isotropic and linear orthotropic models. The results show parameters when each test were fit separately (such that $n_t = 1$). Lastly, the cross validation errors were computed by

fitting parameters to all combinations of the three tests ($n_t = 3$). The focus of the results is to demonstrate the effect of the two objective functions.

4.3.1 Linear Isotropic Material Model

Resulting parameters for the single parameter (E) linear isotropic material model are found in Table 4-4, and results for the two parameter model (E and G) are shown in Table 4-5. The one parameter model used a Poisson's ratio of 0.24, while optimization of the two parameter resulted in a Poisson's ratio near 0.5. Effectively the shear modulus in the two parameter model approached the lower limit[3] , and the FE model is unable to run when the Poisson ratio exceed 0.5. Poisson's ratio appears to significantly effect the stiffness modulus E, in which the one parameter model resulted in a larger stiffness modulus. For both models there was little difference between parameters from minimizing e or e_w with the first test. The second and third test produced larger stiffness moduli when minimizing e_w, and the degree of the increase was larger with the one parameter model. In general, it appeared that minimizing e_w resulted in stiffer material parameters. Parameters of the two parameter isotropic model appears less effected by the weighted objective function than the single objective function.

Table 4-4. One parameter isotropic material results from each inverse analysis. Note ν was fixed to 0.24.

	Minimizing e E (GPa)	Minimizing e_w E (GPa)
Test 1	0.279	0.283
Test 2	0.222	0.292
Test 3	0.242	0.282
Test 4	0.218	0.253

The objective values from the various fits are shown in Table 4-6. For both objective functions, the fourth test resulted in the smallest objective values (or the best fit). The largest objective values (or the worst fit test) depends upon which objective function was minimized,

[3] The lower limit of G is $E/3$, and Poisson's ratio is expressed as $\nu = E/(2G) - 1$.

Table 4-5. Resulting isotropic material parameters from each inverse analysis. Note ν is calculated from E and G.

	Minimizing e			Minimizing e_w		
	E (GPa)	G (GPa)	ν	E (GPa)	G (GPa)	ν
Test 1	0.279	0.113	0.24	0.283	0.114	0.24
Test 2	0.160	0.054	0.48	0.170	0.057	0.48
Test 3	0.162	0.054	0.50	0.170	0.057	0.49
Test 4	0.154	0.052	0.48	0.155	0.052	0.49

but appears to be either the second or third test. In most cases, the two parameter model resulted in lower objective function values than the one parameter model.

Table 4-6. Resulting objective values when fitting the linear isotropic models to each bulge inflation test.

	One parameter (E)		Two parameter (E, G)	
	e (mm)	e_w	e (mm)	e_w
Test 1	1.554	0.497	1.554	0.497
Test 2	1.881	0.795	1.699	0.725
Test 3	1.870	0.588	1.716	0.549
Test 4	1.195	0.457	1.054	0.403

4.3.2 Linear Orthotropic Material Model

The simplified linear orthotropic material parameters resulting from inverse analysis on the individual tests are shown in Table 4-5. The parameters of the orthotropic model are very different depending upon which objective function was minimized. There are sizable changes to both E_1 and E_2 depending upon whether e or e_w was minimized. The most interesting changes occur in the second and third test, where the choice of objective function reversed the stiffness directions. Minimizing e resulted in $E_2 > E_1$, but minimizing e_w resulted in $E_1 > E_2$. Overall, minimizing e_w resulted in parameters that were more consistent from test to test which is expected since the test material was nominally identical. While the stiffness moduli were very different depending on e or e_w, the shear modulus was nearly the same in all conditions.

The objective values resulting from each parameter set with the linear orthotropic model are shown in Table 4-8. The table shows the resulting values of e_w when e was minimized,

Table 4-7. Resulting orthotropic material parameters from minimizing tests independently with each inverse analysis. Note that ν_{12} was fixed to 0.24.

	Minimizing e (GPa)			Minimizing e_w (GPa)		
	E_1	E_2	G_{12}	E_1	E_2	G_{12}
Test 1	0.343	0.248	0.005	0.303	0.229	0.005
Test 2	0.212	0.241	0.004	0.306	0.230	0.005
Test 3	0.217	0.257	0.004	0.306	0.229	0.005
Test 4	0.239	0.215	0.004	0.280	0.215	0.005

and vice versa. The definition of the worse fit depends upon which objective function was minimized. In all cases, the value of e_w was worse when e was minimized than when e_w was minimized. A similar statement can be made for minimizing e_w. If we consider test two, the objective values when minimizing e changed up to 15% when minimizing e_w while E_1 changed over 40% when the objective function was changed.

Table 4-8. Objective values when minimizing e or e_w for the linear orthotropic model to each bulge inflation test.

	Minimizing e (GPa)		Minimizing e_w (GPa)	
	e (mm)	e_w	e (mm)	e_w
Test 1	1.550	0.512	1.773	0.490
Test 2	1.660	0.765	1.917	0.710
Test 3	1.702	0.570	1.759	0.527
Test 4	1.033	0.406	1.101	0.380

Comparisons of the differences between the two parameter isotropic material model and the linear orthotropic material model are shown in Figures 4-7 through 4-10. The chosen displacement locations occur at the approximate maximums for the linear orthotropic FE model, as previously shown in Figures 4-4 through 4-6. The Δ_x displacements occur at $[x = 56, y = 0]$, the Δ_y displacements occur at $[x = 0, y = 63]$, and the Δ_z displacements occur at $[x = 0, y = 0]$ on the surface of the material. The displacements were plotted with the inflation pressure. The results of the one parameter isotropic material model have been omitted, because they were nearly identical to the two parameter isotropic results with the same objective function.

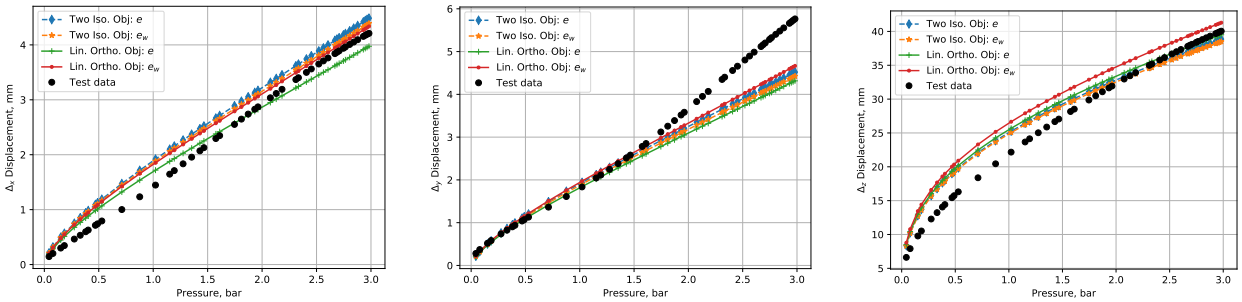

A Δ_x displacement B Δ_y displacement C Δ_z displacement

Figure 4-7. Resulting displacements from the two parameter isotropic and the linear orthotropic material models compared with test 1. The Δ_x results shown in A) occur at $[x = 56, y = 0]$. The Δ_y results shown in B) occur at $[x = 0, y = 63]$. The Δ_z results shown in C) occur at $[x = 0, y = 0]$.

The linear orthotropic FE model appears to match the selected test data better than the isotropic model in all of the cases presented in Figures 4-7 through 4-10. Although it is unclear whether the choice of e or e_w as the objective function resulted in a better fits. It appears that the linear orthotropic model with e_w as the objective function matched the Δ_x and Δ_y displacements better, while the e objective function matched the Δ_z displacements better. There are exceptions to both of these cases, where the reverse is seen, depending on which test is considered.

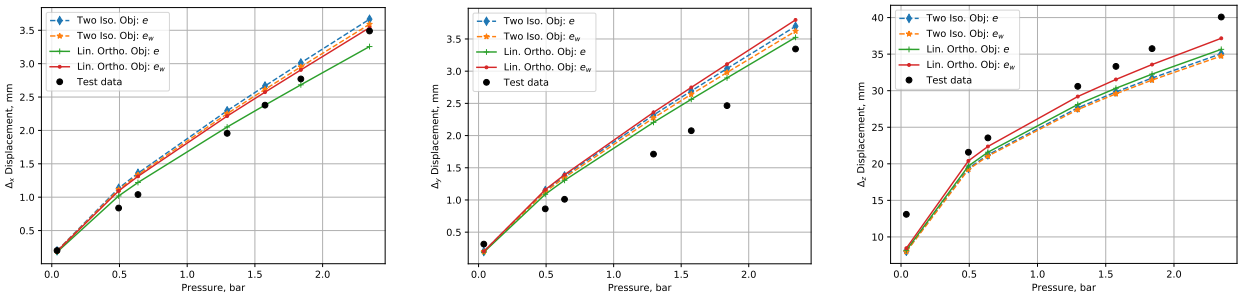

A Δ_x displacement B Δ_y displacement C Δ_z displacement

Figure 4-8. Resulting displacements from the two parameter isotropic and the linear orthotropic material models compared with test 2. The Δ_x results shown in A) occur at $[x = 56, y = 0]$. The Δ_y results shown in B) occur at $[x = 0, y = 63]$. The Δ_z results shown in C) occur at $[x = 0, y = 0]$.

The differences between e and e_w for the two parameter isotropic model were very subtle. However, there is a more noticeable difference between e and e_w for the linear orthotropic material model. This is most evident in the maximum Δ_z displacement pressure curves for all tests. The non-linearity of the Δ_z displacements is more prevalent than the Δ_x or Δ_y displacements.

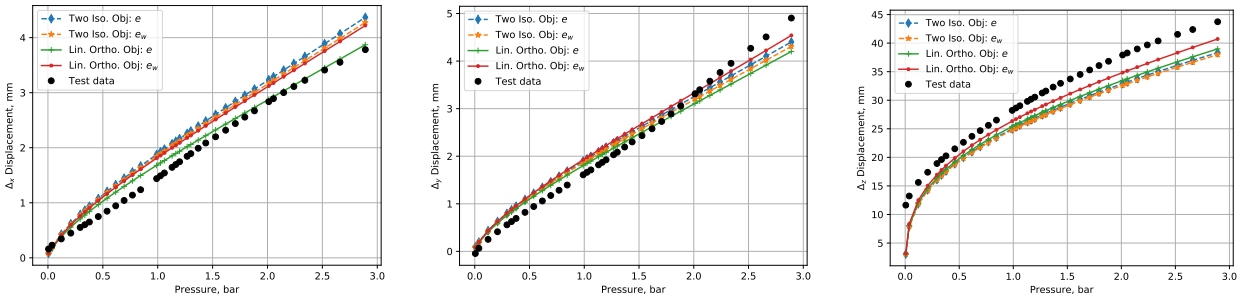

A Δ_x displacement B Δ_y displacement C Δ_z displacement

Figure 4-9. Resulting displacements from the two parameter isotropic and the linear orthotropic material models compared with test 3. The Δ_x results shown in A) occur at $[x = 56, y = 0]$. The Δ_y results shown in B) occur at $[x = 0, y = 63]$. The Δ_z results shown in C) occur at $[x = 0, y = 0]$.

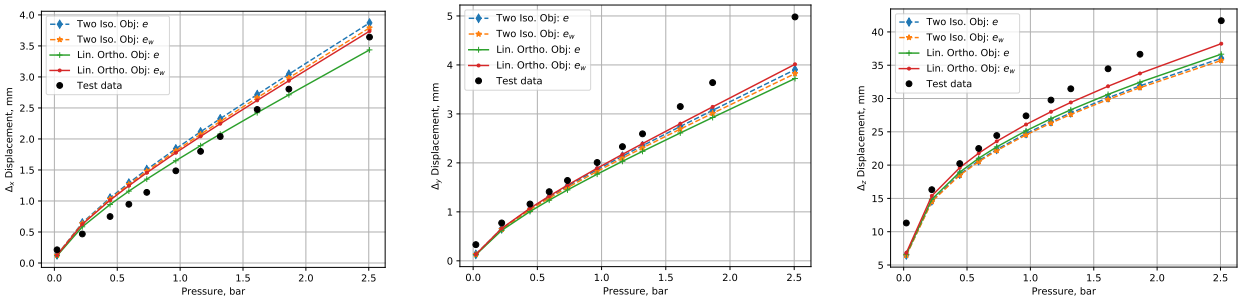

A Δ_x displacement B Δ_y displacement C Δ_z displacement

Figure 4-10. Resulting displacements from the two parameter isotropic and the linear orthotropic material models compared with test 4. The Δ_x results shown in A) occur at $[x = 56, y = 0]$. The Δ_y results shown in B) occur at $[x = 0, y = 63]$. The Δ_z results shown in C) occur at $[x = 0, y = 0]$.

4.3.3 Cross Validation Material Model Comparison

Inverse analyses were performed to fit isotropic and orthotropic material models to the bulge inflation tests. Additional inverse analyses were performed such that a leave-one-test-out

cross validation score was computed for each material model. The resulting discrepancy values are presented in Table 4-9. The orthotropic material model had the lowest cross validation error when e_w was minimized, but the two parameter isotropic material model had the lowest cross validation error when e was minimized. The different objective functions appear to prefer different material models. This implies that the material model which generalizes the bulge inflation test better depends on the definition of the discrepancy between the test data and FE model.

Table 4-9. Resulting discrepancy from the inverse analysis and leave-one-test-out cross validation.

	Cross validation error		Left out test values	
Model	e (mm)	e_w	e [1, 2, 3, 4]	e_w [1, 2, 3, 4]
isotropic (E)	1.995	0.590	[2.47, 2.10, 1.87, 1.54]	[0.62, 0.52, 0.59, 0.63]
isotropic (E and G)	1.833	0.554	[2.37, 1.85, 1.72, 1.40]	[0.57, 0.50, 0.56, 0.60]
orthotropic	1.856	0.533	[2.47, 1.88, 1.73, 1.35]	[0.49, 0.72, 0.53, 0.40]

The two parameter isotropic material model parameters from the full inverse analysis and the cross validation runs are presented in Table 4-10. When e was minimized, the stiffness modulus varied from 0.155 to 0.170 GPa. However, when e_w was minimized the stiffness modulus varied from 0.170 to 0.193 GPa. and the shear modulus varied from 0.057 to 0.070 GPa. Overall, e_w resulted in more consistent and stiffer moduli.

Table 4-10. Resulting two parameter isotropic material parameters from each inverse analysis.

	Minimizing e (GPa)		Minimizing e_w (GPa)	
	E	G	E	G
Leaving test 1 out	0.155	0.052	0.170	0.057
Leaving test 2 out	0.167	0.056	0.170	0.057
Leaving test 3 out	0.164	0.055	0.170	0.056
Leaving test 4 out	0.170	0.057	0.193	0.066

The orthotropic material parameters from the cross validation study are shown in Table 4-11. There is a significant difference between the parameter variance depending upon which objective function was used. For instance, E_1 varied from 0.224 to 0.280 GPa when e was

minimized. However, when e_w was minimized E_1 varied from 0.303 to 0.305 GPa. A similar trend occurs for E_2 and G_{12}, where minimizing e_w resulted in more consistent parameters.

Table 4-11. Resulting orthotropic material parameters from each inverse analysis.

	Minimizing e (GPa)			Minimizing e_w (GPa)		
	E_1	E_2	G_{12}	E_1	E_2	G_{12}
Leaving test 1 out	0.224	0.235	0.003	0.303	0.229	0.005
Leaving test 2 out	0.297	0.231	0.004	0.304	0.229	0.005
Leaving test 3 out	0.284	0.224	0.004	0.304	0.229	0.005
Leaving test 4 out	0.280	0.244	0.003	0.305	0.229	0.005

4.4 Discussion

The most striking result was the effect of the two objective functions on selecting parameters for the linear orthotropic material model. When e was minimized the linear orthotropic parameters varied significantly from test to test, with some tests resulting in $E_2 > E_1$ and others $E_1 > E_2$. This was not the case when e_w was minimized, in which the parameters from test to test were fairly consistent with $E_1 > E_2$. The difference between the two objective functions was that e considered the discrepancies in the x, y and z directions to be of equal weight, while e_w considered the z discrepancies to be one tenth the weight. This weighting factor corresponds to an imbalance between the test maximum z displacement being about ten times larger than the maximum x or y displacements. It's important to clarify that both e and e_w would approach zero if it was possible for a perfect fit, however resulting material parameters occur with the inability to perfectly fit the data. In these circumstances it appears that one may need to careful consider how to eventuate the discrepancy of the displacement field, especially under similar imbalanced displacement data.

Tests two and three are of particular interest with the linear orthotropic model, because these tests resulted in $E_2 > E_1$ when e was minimized. It could be reasonable to assume that the test directions were incorrect by a factor of $90°$, and that this mistake in the x and y directions resulted in the set of parameters. Additional inverse analyses were performed on these tests, where the test data was rotated by factors of $45°$ and $90°$. What is interesting is that when e was minimized the resulting parameters resulted in $E_2 > E_1$ regardless of the

rotation, and there was little change to the parameters. However, when e_w was minimized both E_2 and E_1 would change significantly based on the rotation. This hints that giving more weight to the x and y displacements, like in e_w, would be better if an inverse analyses was required to identify orthotropic parameters without knowing the primary and secondary material directions.

The different objective functions had an interesting effect on using leave-one-test-out cross validation for material model selection. When e was minimized, the cross validation error favored the two parameter isotropic material model. Though when e_w was minimized, the cross validation error favored the orthotropic material model by a much larger margin. This reemphasizes the importance of selecting an appropriate objective function, as the choice of objective function not only effects the resulting parameters, but also effects the perceived generalization error of the model.

4.5 Conclusion

An inverse analysis was described to find material parameters by matching the full displacement field from bulge inflation tests. Optimization was used to find material parameters in a FE model that best matched the experimental displacement field from tests on PVC-coated polyester. Material parameters were determined for a linear isotropic and simplified linear orthotropic material models. Two different objective functions were considered to describe the discrepancy between the experimental data and numerical model. The first objective function considered equal weight between the displacement components, while the other function gave more weight to the x and y displacements. The weighting scheme was chosen to compensate for the fact that the majority of the deflections within the bulge inflation test occur out-of-plane. Resulting material parameters for the linear orthotropic material model were very different depending on which objective function was minimized. Thus the choice of objective function being considered is very important when performing such an optimization on the full field data.

Cross validation was performed to determine whether the isotropic or orthotropic material model was a better representation of the material behavior. There was little difference in the cross validation error according to the equally weighted objective function, however the weighted objective function heavily favored the orthotropic material model. This indicates that the choice of objective function was not only important in material parameter selection, but can also impact material model selection.

CHAPTER 5
SUMMARY

This collection of work has demonstrated that the choice of objective function could have an important impact when identifying material parameters, to a degree that has been overlooked in much of the literature. The objective function was abstracted differently throughout this work, but can be thought of as 1) problem definition, 2) error measure, and 3) normalization of data. The second chapter considered problem definition, and demonstrated that different material parameters occur when matching an imperfect material model using either the stress-strain or load-displacement responses. The third chapter considered different error measures directly, and demonstrated that different mathematical norms will result in different material parameters provided imperfect matching. The fourth chapter worked with the normalization of experimental data, and demonstrated how different normalization schemes of displacement components result in different material parameters. The lessons learned in this work recommend engineers to explore more than one possible objective function, as the results related to the different objective functions will provide more insight to the task. Researchers who plan to present material parameters from a study should pay careful attention to how the choice of objective function influence their results.

Non-linear orthotropic material parameters where characterized for PVC-coated polyester. Uniaxial tests where performed in the material's primary, secondary, and 45° bias directions. Parameters were determined by either matching a FE model to the experimental load-displacement results, or by matching the stress-strain responses. These two approaches can be thought of as two different objective functions. This resulted in either the load-displacement behavior or the stress-strain behavior being characterized more accurately by the FE model, because the material model couldn't perfectly describe the complex behavior of the material. The results were most pronounced on the 45° bias test, for which there are very clear distinctions between the load-displacement and stress-strain sets of material parameters.

The choice of matching the load-displacement or stress-strain responses resulted in different non-linear orthotropic material parameters.

Parameters were determined for a kinematic hardening model using several different similarity measures. Some of the methods, like PCM, originated from the material parameter identification community. Other methods, like the Discrete Fréchet Distance and Dynamic Time Warping had a substantial history in the machine learning community. All of these methods are convenient for an engineer to use as the objective function when calibrating materials parameters when working with tension-compression-tension tests. The fundamental difference between methods is analogous to different mathematical norms. Using these different similarity measures resulted in different sets of kinematic hardening parameters.

Isotropic and orthotropic material parameters were determined from bulge inflation tests on PVC-coated polyester. Experiments captured full-field displacements using DIC. Parameters where characterized using an inverse analysis that matched a FE model displacement field to the experimental data. The bulge inflation tests had a numerical issue, in which the out-of-plane displacements were an order of magnitude larger than the in-plane displacements. Two objective functions were formulated with different normalization schemes of the displacements. The two normalization schemes resulted in significantly different material parameters. A normalization scheme which considered the displacement residuals to be of equal weight resulted in the best and most consistent orthotropic parameters.

APPENDIX A
LACK OF FIT TESTS TO FIND ADEQUATE MATERIAL MODELS

A lack-of-fit test can be used to determine whether a finite element (FE) material model, or experimental results should be the focus to improve overall model accuracy. The lack-of-fit test compares the unbiased estimate of variance to the estimated variance from noise within data. GSJ and Hart methods from literature are provided to estimate the noise within data, and a generalized lack-of-fit test is described. The variance estimators are compared and convergence is demonstrated on a simple regression problem. The lack-of-fit test is then applied to a material calibration problem using the FE method. The lack-of-fit test indicates that the shear component of a non-linear orthotropic material models could be improved, despite already being considered an excellent fit. Additionally the lack-of-fit test is used with a load-dependent Poisson's ratio to demonstrate that the variance in the experimental data should be reduced in order to improve the model.*

A.1 Introduction

It has become common practice to calibrate material model parameters on experimental data for finite element (FE) analyses. The overall accuracy of the FE model is dependent on the model's ability to replicate the material behavior. Thus it is important to select the best material parameters to accurately describe the material behavior. In general parameter values are selected such that the FE model reproduces some experimental results. The accuracy of the FE model can be improved by either improving the model (e.g., finding a better material model), or by improving the experimental data (e.g., reducing the uncertainty in the experimental data). Potentially a lack-of-fit test may be used to decide which aspect (model or data) should be the focus for improvement.

* A previous version of this chapter was published in AIAA Non-Deterministic Approaches Conference [90].

In this context a lack-of-fit investigation looks at whether the primary contribution of error is due to the inherent variance in experimental data, or the inability of the material model to replicate the experimental data. Mismatch between the FE model and experimental data is due to both the material model not being accurate enough, and noise in the experimental data. However noise doesn't just appear in experimental data, and sometimes a poor model may generate aditional noise as demonstrated by Park et al. [91]. Noise leads to discrepancies between the true material model and the captured experimental data. Additionally noise in data may yield calibrated material parameters that are not accurate. A model passing the lack-of-fit test indicates that the noise in the experimental data is limiting the accuracy of the calibrated parameters. Alternatively a failed lack-of-fit test indicates that the material model is unable to replicate the response captured in the experimental data.

Analysis of variance (ANOVA) is a widely used set of statistical models aimed at comparing variation between data. ANOVA models include the partitioning of the sum of squares, lack-of-fit tests, likelihood ratio test, and the F-test. Traditionally these methods require the data to have true replicates, though practically obtaining these replicates is difficult for material tests. In terms of material response modeling, true replicates would require multiple stress values for each strain value. However material test data is typically collected in a way such that there is a dependent response as a function of some other independent variable (e.g., variation of stress values among strain values for repeated uniaxial tests).

The difference between true replicates and a typical material response can be seen in figure A-1, which shows an example of true replicates in A) and a more typical experimental response in B). There are multiple $f(x)$ values for a given x when looking at a response containing true replicates. True replicates of experimental responses can be difficult to capture. An experiment is generally performed to captured a response $f(x)$ which varies with respect to x. The experiment itself is repeated, however the captured responses may not contain replicates for the exact same independent variable x. There are classical statistical methods that can be applied when true replicates exist [92].

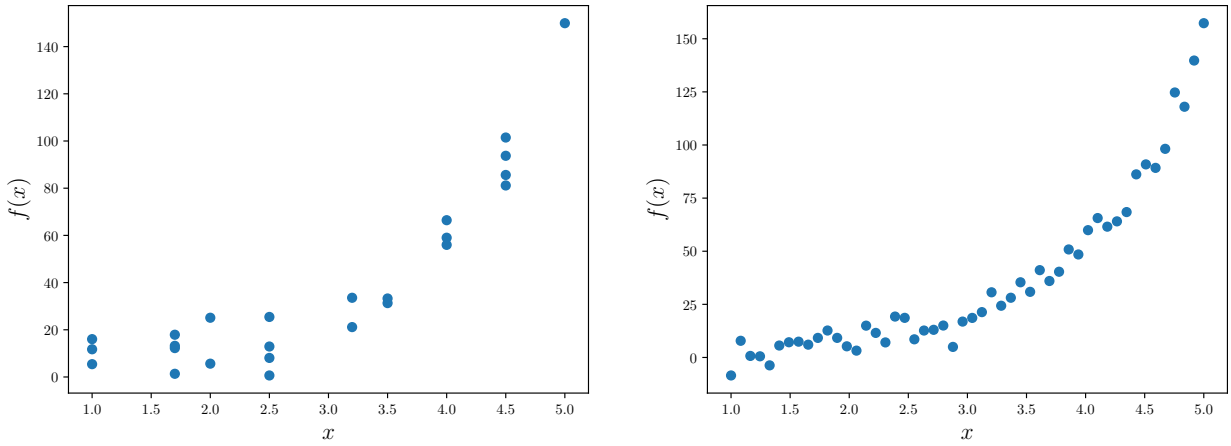

A True replicates

B Typical response

Figure A-1. True replicates shown in A) where there are multiple $f(x)$ for a unique x. A more typical response is shown in B) of collected experimental data where $f(x)$ appears to demonstrate inherent variation amid different x values.

This paper goes on to describe the lack-of-fit test which is based on comparing a ratio of variances. First the unbiased variance is calculated which represents the variance between the model and data. Then the variance from the noise (or scatter) within the data is estimated. Two different variance estimators are used from literature. First the popular GSJ variance estimator is described [93]. Then a generalized variance estimator proposed by Hart is described [94]. These variance estimators are used to estimate the variance due to the noise (or scatter) within experimental data. A classical lack-of-fit test is then described from the literature by comparing these variances.

The GSJ and Hart variance estimators are compared against each other. Additionally the convergence behavior of the variance estimators and the lack-of-fit tests is demonstrated on a simple linear regression example. The lack-of-fit tests are then used on a material parameter identification problem. An example shows a case where it is suggested that the shear component of a non-linear orthotropic material model be improved in order to improve the accuracy of the FE model. Another example uses the lack-of-fit test to show that the variation within experimental data be reduced in order to improve a load-dependent Poisson's ratio model.

A.2 Statistical Methods

The variances investigated either represent the variance from the error of the fit, or the variance from noise (or scatter) within the data. Mathematical definitions of the variances are proposed from literature. The unbiased variance represents the variance of the error between the model and data. The GSJ and Hart methods are presented to approximate the inherent variance from noise within the data. Popular alternative variance estimates are also mentioned, though this work emphasizes the GSJ and Hart methods. Lastly the F-statistic is proposed for a generalized lack-of-fit test.

A.2.1 Unbiased Variance

The residual $\boldsymbol{e}$ is described as

$$\boldsymbol{e} = f(\boldsymbol{x}) - \hat{f}(\boldsymbol{x}) \tag{A-1}$$

where the predictive model is represented by $\hat{f}(\boldsymbol{x})$, and the data is represented by $f(\boldsymbol{x})$. The unbiased estimate of the variance is

$$\hat{\sigma}^2 = \frac{\boldsymbol{e} \cdot \boldsymbol{e}^{\mathsf{T}}}{n - n_\beta} \tag{A-2}$$

for a linear regression problem, with n number of data points, and n_β number of parameters in the predictive model [92].[1] The unbiased estimate of the variance assumes that the model accurately describes the data. If this unbiased variance is significantly larger than the variance due to noise in the data, then the model is not accurate.

The measure of the lack-of-fit can be described by the difference between the unbiased variance and the variance from noise in data. It is common to use the unbiased variance as a goodness-of-fit metric for a predictive model. It can be noted that $\boldsymbol{e} \cdot \boldsymbol{e}^{\mathsf{T}}$ represents the sum

[1] Myers et al. in Ref. [92] refers to $\hat{\sigma}^2$ as the unbiased estimator. It was chosen to refer to this term as the unbiased variance in order to avoid confusion from the later described variance estimators.

of the square of the residuals, another metric that is often used to represent goodness-of-fit for regression problems.

A.2.2 GSJ Variance Estimator

Gasser et al. proposed a variance estimator based on local linear fitting between three consecutive points [93]. This method for estimating variance is commonly referred to as the GSJ method and was originally intended for non-linear regression. However, the GSJ method isn't just limited to applications in non-linear regression. For instance the GSJ method can be used to approximate the variance due to noise (or scatter) within data.

Let's considered a data set $f(\boldsymbol{x})$, where $\boldsymbol{x}$ is ordered as $x_1 < x_2 < \cdots < x_n$. A vector of pseudo residuals $\tilde{\boldsymbol{e}}$ can be constructed by considering every three consecutive data points. A single pseudo residual $\tilde{e}_i$ is described by

$$\tilde{e}_i = \frac{x_{i+1} - x_i}{x_{i+1} - x_{i-1}} f(x_{i-1}) + \frac{x_i - x_{i-1}}{x_{i+1} - x_{i-1}} f(x_{i+1}) - f(x_i) \tag{A-3}$$

$$= a_i f(x_{i-1}) + b_i f(x_{i+1}) - f(x_i) \tag{A-4}$$

for $i = 2, 3, \cdots, n-1$. The variance $\hat{\sigma}_e^2$ of the estimated noise within data is obtained by taking

$$\hat{\sigma}_e^2 = \frac{1}{n-2} \sum_{i=2}^{n-1} \frac{e_i^2}{a_i^2 + b_i^2 + 1} \tag{A-5}$$

where n represents the number of data points. It's worthwhile to note that $\hat{\sigma}_e^2$ can be calculated for all one dimensional data containing at least three points. The GSJ variance estimator becomes more accurate as the number of data points increases, and this convergence behavior is demonstrated in Section III.

A.2.3 Hart Variance Estimator

Hart proposed a generalized variance estimator useful for lack-of-fit tests [94]. The estimator considers the noise within data by taking differences between every two consecutive residuals. The derivation is meant for linear regression problems, however it can be extended to non-linear regression problems by using the linearized regression matrix described by Coppe

et al. [95]. An example regression matrix $\boldsymbol{X}$ for fitting a quadratic polynomial to data is represented bellow.

$$\boldsymbol{X} = \begin{bmatrix} 1 & x_1 & x_1^2 \\ 1 & x_2 & x_2^2 \\ \vdots & \vdots & \\ 1 & x_n & x_n^2 \end{bmatrix} \tag{A-6}$$

The data should be ordered consecutively as $x_1 < x_2 \cdots < x_n$. Thus the first residual is defined as the difference between the data and predictive model at the first location $e_1 = f(x_1) - \hat{f}(x_1)$, the second residual $e_2 = f(x_2) - \hat{f}(x_2)$, and so forth as $e_n = f(x_n) - \hat{f}(x_n)$. The estimate of the variance from the noise in the data $\tilde{\sigma}^2$ is described as

$$\tilde{\sigma}^2 = \frac{\boldsymbol{e}^{\mathsf{T}} \cdot \boldsymbol{H} \cdot \boldsymbol{e}}{a_n} \tag{A-7}$$

$$= \frac{1}{a_n} \sum_{i=2}^{n} \left(e_i - e_{i-1} \right)^2 \tag{A-8}$$

where $a_n = 2(n-1) - \text{trace}(\boldsymbol{H}\boldsymbol{X}(\boldsymbol{X}^{\mathsf{T}}\boldsymbol{X})^{-1}\boldsymbol{X}^{\mathsf{T}})$ and $\boldsymbol{H}$ is the $n \times n$ tridiagonal matrix.

$$H = \begin{bmatrix} 1 & -1 & 0 & 0 & 0 & \cdots & 0 & 0 & 0 \\ -1 & 2 & -1 & 0 & 0 & \cdots & 0 & 0 & 0 \\ 0 & -1 & 2 & -1 & 0 & \cdots & 0 & 0 & 0 \\ \vdots & \vdots & \vdots & \vdots & \vdots & \ddots & \vdots & \vdots & \vdots \\ 0 & 0 & 0 & 0 & 0 & \cdots & -1 & 2 & -1 \\ 0 & 0 & 0 & 0 & 0 & \cdots & 0 & -1 & 1 \end{bmatrix} \tag{A-9}$$

Hart uses this generalized variance estimate to perform non-parametric lack-of-fit tests, stating that it is more conservative than GSJ. However unlike GSJ, Hart's method is dependent upon the chosen regression model. The convergence behavior of the Hart variance estimator (with respect to the accuracy of the regression model and the number of data points) is demonstrated in Section III.

A.2.4 Alternative Variance Estimators

Various other methods have been used to estimate the variance from noise in data. Notable simple methods include estimating the noise by the variation between consecutive x points as $\hat{\sigma}_x^2$, or by the variation between consecutive $f(x)$ points as $\hat{\sigma}_f^2$.

$$\hat{\sigma}_x^2 = \frac{1}{2(n-1)} \sum_{i=2}^{n} \left(x_i - x_{i-1}\right)^2 \tag{A-10}$$

$$\hat{\sigma}_f^2 = \frac{1}{2(n-1)} \sum_{i=2}^{n} \left(f(x_i) - f(x_{i-1})\right)^2 \tag{A-11}$$

However Gasser et al. demonstrated that the GSJ method was more accurate than $\hat{\sigma}_f^2$ [93]. Additionally $\hat{\sigma}_x^2$ will not provide useful insight when x has been systematically spaced. It is worthwhile to note that Altman and Paulson provided an alternative derivation for the GSJ method when the spacing between x points is consistent [96]. Hart stated in Ref. [94] that his generalized method is closely related to the cubic spline method created by Munson and Jernigan [97]. Expansions of the GSJ method could be created using higher order (quadratic, cubic) interpolations between consecutive data points.

A.2.5 F-Test and Lack-of-Fit

The F-test represents a statistical test for investigating lack-of-fit. Essentially F represents our test statistic, which will be used to determine whether or not a model is adequate with the provided data. A classical lack-of-fit test categorizes the error resulting from either lack-of-fit or pure error [92]. Lack-of-fit error refers to the error between the model and true function. While pure error represents the inherent error from the noise (or scatter) within the data. Using these principles, the F-statistic can be generalized as the the ratio of variances

$$F \approx \frac{\hat{\sigma}^2}{\hat{\sigma}_e^2} \approx \frac{\hat{\sigma}^2}{\tilde{\sigma}^2} \tag{A-12}$$

where the unbiased estimate of variance is compared to the estimated variance of noise within the data.

The F-statistic follows the F$(X; n - n_\beta, n - 1)$ distribution where n represents the number of data points and n_β represents the number of model parameters. The null hypothesis H_0 is constructed assuming that there is no lack-of-fit, and the model is adequate given the scatter in the data. For this hypothesis, the P-value is obtained by taking the complementary cumulative distribution of F$(F; n - n_\beta, n - 1)$. The null hypothesis is accepted when

$$H_0 : \text{P-value} > 0.05 \tag{A-13}$$

and the P-value is greater than some level of confidence, which conventionally is 0.05 for significance.

A rejected null hypotheses implies that the model poorly describes the data. The null hypothesis is rejected for large F values, where the majority of variance is characterized from the inability of the model to fit the data. Alternatively all of the modeling variance could be equal to the variance from noise in the data, or $F = 1$. When $F = 1$ the model is accepted, because it is assumed that the only error in the model originates from the inherent noise in the data. It is possible for the F-statistic to be less than 1, because the estimated variance from noise may be greater than the unbiased variance (particularly when there is error in the estimated variance). The models are usually accepted for a small test statistic where $F < 1$ because the error is less than the approximated scatter within the data.

A.3 Demonstrated Convergence of Statistical Methods

A simple example was created to demonstrate the convergence behavior of the variance estimators and lack-of-fit test. Data is sampled from the equation

$$f(x) = -1.4 + 1.5x + 190.3x^2 \tag{A-14}$$

with the addition of random Gaussian noise that follows the normal distribution of $N(\mu = 0, \sigma^2 = 25)$. The number of data points was increased to demonstrate the convergence behavior. The data points x_i are selected at random from $0 \leq x_i \leq 1$. The least squares method is used to fit polynomials with degrees ranging from zero to five to the data. With the

Hart method, it is also important to understand the effect of the chosen regression model on the estimated variance. Polynomials with degrees three to five were chosen to provide insight on overfitting the true function. A k degree polynomial is expressed as

$$\hat{f}(\boldsymbol{x}) = \sum_{j=0}^{k} \beta_j \boldsymbol{x}^j \tag{A-15}$$

where the β_j parameters are determined from the least squares fit. Examples of polynomial fits for 10, 20, and 200 data points can be seen in figure A-2.

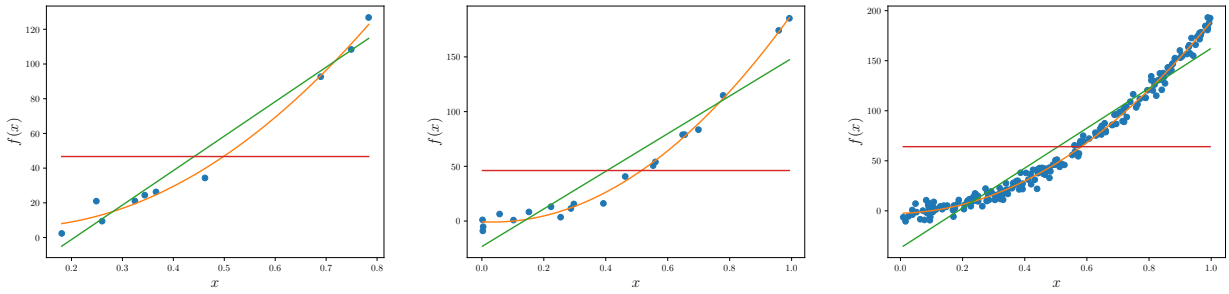

A 10 data points B 20 data points C 200 data points

Figure A-2. Constant, linear, and quadratic polynomial fits for 10, 20, and 200 data points.

A.3.1 Variance Estimator Convergence

The estimated variance from noise for the GSJ and Hart methods are compared to the variance of the added noise randomly drawn from the normal distribution. It is the intention of this comparison to demonstrate the accuracy of the estimated variance from noise for a simple data set. The estimated variances are presented in table A-1. For a small number of points the GSJ method does a poor job at estimating the variance of the noise in the data. However as the number of data points increases, the accuracy of the GSJ method improves. The same trend is observed with the Hart method, in which the number of data points improved the accuracy of the estimated variance of noise. The Hart method was able to estimate the noise with reasonable accuracy when using higher degree polynomials and only 10 data points. For this example the Hart method using the 4^{th} degree polynomial produced the most accurate estimation of the variance from noise in the signal. Lastly it is worthwhile to note that even

with 20,000 data points, the estimated variance from all methods converged to 25.3 despite having a true variance of 25.0. This discrepancy looks worse as a variance than as a standard deviation because of the squared term. If standard deviations were considered, the estimated standard deviation would be 5.03 and the true standard deviation would be 5.0.

Table A-1. Demonstrated convergence of the GSJ and Hart variance from noise estimation methods for the quadratic example with 10 through 20,000 data points.

Variance metric	$n = 10$	$n = 20$	$n = 200$	$n = 2000$	$n = 20,000$
GSJ $\hat{\sigma}_e^2$	271.4	177.5	27.1	23.8	25.3
0 degree Hart $\tilde{\sigma}^2$	260.1	171.4	27.0	23.8	25.3
1 degree Hart $\tilde{\sigma}^2$	37.6	60.4	25.6	23.8	25.3
2 degree Hart $\tilde{\sigma}^2$	30.4	27.1	25.3	23.9	25.3
3 degree Hart $\tilde{\sigma}^2$	25.7	27.2	25.3	23.9	25.3
4 degree Hart $\tilde{\sigma}^2$	23.2	24.8	25.3	23.9	25.3
5 degree Hart $\tilde{\sigma}^2$	25.9	25.6	25.3	23.9	25.3
True σ^2 from noise*	23.58	24.1	24.7	24.7	25.0

* True noise refers to the variance calculated from the samples pulled from the normal distribution. The normal distribution used had a $\sigma^2 = 25.0$, however the actual variance of these samples will differ when n is small.

It was possible the random spacing of the $\boldsymbol{x}$ data points influenced the performance of the GSJ variance. To demonstrate this affect, the GSJ variance was recalculated for linearly spaced x data points chosen from $0 \leq x_i \leq 1$. The noise from the normal distribution was preserved from the previous example. The results of the linearly spaced x values on the GSJ variance is presented in table A-2. The GSJ method estimated the variance from noise more accurately when using linearly spaced data points as opposed to the randomly selected data points. This likely occurs because the linear approximation between three far points is much worse than three close data points. Despite improving, the GSJ variance estimate did a poor job at estimating the noise with few data points.

A.3.2 Lack-of-Fit Convergence

The F-statistic and P-values were calculated for the previous example of fitting various degree polynomials to quadratic data with normally distributed noise. The unbiased estimate

Table A-2. Demonstrated convergence of the GSJ when data points are linearly spaced from $0 \leq x_i \leq 1$.

Variance metric	$n = 10$	$n = 20$	$n = 200$	$n = 2000$	$n = 20,000$
GSJ $\hat{\sigma}_e^2$	255.6	93.8	26.0	24.6	25.2
True σ^2 from noise*	23.58	24.1	24.7	24.7	25.0

* True noise refers to the variance calculated from the samples pulled from the normal distribution. The normal distribution used had a $\sigma^2 = 25.0$, however the actual variance of these samples will differ when n is small.

of variance $\hat{\sigma}^2$ for the model fits are seen in table A-3. The F-statistic and P-value were calculated for each degree polynomial fit. The results using the GSJ method are shown in table A-4 and the Hart method in table A-5. In general the GSJ and Hart methods are in agreement with accepting and rejecting models based on the lack-of-fit test. Additionally the GSJ and Hart methods converge to the same F-statistic values for this example when $n = 2000$ data points are used. The only disagreement between the GSJ and Hart methods occur for the 1 degree polynomial fit when $n = 20$, in which the GSJ method accepts the model while the Hart method rejects the model. It is noted that the GSJ method in this case is on the boundary of the 95% confidence hypothesis test, and that the model would have been rejected if 99% confidence hypothesis test was used.

Table A-3. Unbiased estimate of variance $\hat{\sigma}^2$ for various degree polynomial fits to the true quadratic function which included normally distributed noise. The bottom row of the table shows the variance of the normally distributed noise in the data.

Degree	$n = 10$	$n = 20$	$n = 200$	$n = 2000$	$n = 20,000$
0	2008	3307	3571	3321	3291
1	85.9	384	208	237	227
2	27.3	25.5	24.9	24.7	25.0
3	21.3	26.2	25.0	24.7	25.0
4	21.8	22.7	25.1	24.7	25.0
5	26.3	22.4	24.7	24.7	25.0
True σ^2 from noise*	23.58	24.1	24.7	24.7	25.0

* True noise refers to the variance calculated from the samples pulled from the normal distribution. The normal distribution used had a $\sigma^2 = 25.0$, however the actual variance of these samples will differ when n is small.

Table A-4. GSJ estimated variance used to calculate the F-statistic and P-value for the example quadratic with 10 through 20,000 data points. P-values greater than 0.05 indicated that the data is adequately described by the degree of polynomial fit.

Degree	$n = 10$	$n = 20$	$n = 200$	$n = 2000$	$n = 20,000$
0	$F = 7.40, \mathsf{P} = 0.03$	$F = 18.6, \mathsf{P} = 0.00$	$F = 132, \mathsf{P} = 0.00$	$F = 139, \mathsf{P} = 0.00$	$F = 130, \mathsf{P} = 0.00$
1	$F = 0.30, \mathsf{P} = 0.94$	$F = 2.16, \mathsf{P} = 0.05$	$F = 7.67, \mathsf{P} = 0.00$	$F = 9.94, \mathsf{P} = 0.00$	$F = 8.96, \mathsf{P} = 0.00$
2	$F = 0.10, \mathsf{P} = 1.00$	$F = 0.14, \mathsf{P} = 1.00$	$F = 0.92, \mathsf{P} = 0.73$	$F = 1.04, \mathsf{P} = 0.22$	$F = 0.99, \mathsf{P} = 0.79$
3	$F = 0.08, \mathsf{P} = 1.00$	$F = 0.14, \mathsf{P} = 1.00$	$F = 0.92, \mathsf{P} = 0.72$	$F = 1.04, \mathsf{P} = 0.22$	$F = 0.99, \mathsf{P} = 0.79$
4	$F = 0.08, \mathsf{P} = 1.00$	$F = 0.13, \mathsf{P} = 1.00$	$F = 0.93, \mathsf{P} = 0.71$	$F = 1.04, \mathsf{P} = 0.21$	$F = 0.99, \mathsf{P} = 0.79$
5	$F = 0.10, \mathsf{P} = 0.98$	$F = 0.13, \mathsf{P} = 1.00$	$F = 0.91, \mathsf{P} = 0.74$	$F = 1.04, \mathsf{P} = 0.21$	$F = 0.99, \mathsf{P} = 0.79$

Table A-5. Hart estimated variance used to calculate the F-statistic and P-value for the example quadratic with 10 through 20,000 data points. P-values greater than 0.05 indicated that the data is adequately described by the degree of polynomial fit.

Degree	$n = 10$	$n = 20$	$n = 200$	$n = 2000$	$n = 20,000$
0	$F = 7.70, \mathsf{P} = 0.02$	$F = 19.3, \mathsf{P} = 0.00$	$F = 132, \mathsf{P} = 0.00$	$F = 139, \mathsf{P} = 0.00$	$F = 130, \mathsf{P} = 0.00$
1	$F = 2.27, \mathsf{P} = 0.12$	$F = 6.37, \mathsf{P} = 0.00$	$F = 8.12, \mathsf{P} = 0.00$	$F = 9.94, \mathsf{P} = 0.00$	$F = 8.96, \mathsf{P} = 0.00$
2	$F = 0.90, \mathsf{P} = 0.55$	$F = 0.94, \mathsf{P} = 0.55$	$F = 0.98, \mathsf{P} = 0.55$	$F = 1.04, \mathsf{P} = 0.22$	$F = 0.99, \mathsf{P} = 0.79$
3	$F = 0.83, \mathsf{P} = 0.58$	$F = 0.96, \mathsf{P} = 0.53$	$F = 0.99, \mathsf{P} = 0.54$	$F = 1.04, \mathsf{P} = 0.22$	$F = 0.99, \mathsf{P} = 0.79$
4	$F = 0.94, \mathsf{P} = 0.50$	$F = 0.92, \mathsf{P} = 0.56$	$F = 0.99, \mathsf{P} = 0.52$	$F = 1.04, \mathsf{P} = 0.22$	$F = 0.99, \mathsf{P} = 0.79$
5	$F = 1.02, \mathsf{P} = 0.44$	$F = 0.87, \mathsf{P} = 0.60$	$F = 0.98, \mathsf{P} = 0.56$	$F = 1.04, \mathsf{P} = 0.21$	$F = 0.99, \mathsf{P} = 0.79$

It is important to remember that both the GSJ and Hart methods are estimations of the variance from the scatter in the data. When there is a limited number of data points, the methods may yield different results. However the example problem demonstrated that both the GSJ and Hart methods converge to the same values given a large number of data.

The F-statistic is useful in determining whether a model adequately describes data. In the quadratic example with added normally distributed noise, the F-statistic demonstrated that constant (degree 0) and linear (degree 1) models were inadequate to represent the quadratic data. The models were inadequate because a significant portion of the unbiased variance $\hat{\sigma}^2$ originated from the model's inability to fit the data and not from the inherent variance (from noise) in the data. It is worthwhile to note that the F-statistic does not provide insight about over fitting, since the polynomials with degrees 3-5 were always accepted with the F-statistic.

A.4 Application to Material Parameter Identification

The F-statistic is applied to a material calibration example of Jekel et al., in which a non-linear orthotropic material model is fit to uniaxial test data using non-linear regression [24]. There are three distinctive FE models, one for the warp, fill, and 45° bias uniaxial tests. Each FE model is compared to the corresponding uniaxial experimental data. The intention is to apply the F-statistic to investigate the lack-of-fit for a practical material calibration problem. In terms of material calibration, the F-statistic and lack-of-fit tests represent a useful tool on demonstrating whether the model would improve the most from improvements to the FE model, or from reducing the variance in the experimental data.

Both the GSJ and Hart methods were used to investigate the lack-of-fit. It's worthwhile to note that it is significantly simpler to apply the GSJ method, as the Hart method requires a linearized regression matrix. Since this is a non-linear regression problem, a linearized regression matrix was approximated using finite differences following Coppe et al [95].

The lack-of-fit results are presented in table A-6, where the F-statistic and P-values were calculated for the non-linear orthotropic model on two different PVC-coated polyesters. The Hart and GSJ methods were in agreement for all cases, where only the CF0700T 45° bias

model was deemed inadequate with the provided data. It is interesting to note that this particular model failed the lack-of-fit test, despite being a relatively good fit to the data. For all of the other 5 examples, the lack-of-fit tests demonstrated that the models adequately described the test data. An accepted lack-of-fit test (P-value > 0.05) would indicate that the variance within the experimental data should be reduced in order to improve the overall FE model. Alternatively a rejected lack-of-fit test (P-value ≤ 0.05) would suggest improvements like using a material model that more accurately represented the experimental response.

Table A-6. F-statistics and P-values (model is accepted when P > 0.05) for the non-linear orthotropic material model on two types of PVC-coated polyester.

Material	Method	Warp	Fill	45° bias
CF0700T	GSJ	$F = 0.40, \mathrm{P} = 1.00$	$F = 0.85, \mathrm{P} = 0.73$	$F = 1.59, \mathrm{P} = 0.00$
CF0700T	Hart	$F = 1.35, \mathrm{P} = 0.14$	$F = 1.20, \mathrm{P} = 0.25$	$F = 2.79, \mathrm{P} = 0.00$
VALMEX® 7318	GSJ	$F = 0.46, \mathrm{P} = 1.00$	$F = 0.98, \mathrm{P} = 0.53$	$F = 0.84, \mathrm{P} = 0.79$
VALMEX® 7318	Hart	$F = 1.28, \mathrm{P} = 0.18$	$F = 1.04, \mathrm{P} = 0.45$	$F = 0.86, \mathrm{P} = 0.77$

The fit of the CF0700T 45° bias test data and FE model is shown in A) of figure A-3, while B) shows the VALMEX® 7318 45° bias fit. In both cases the FE model appears to capture the experimental response well. One way to qualitatively investigate lack-of-fit is to plot the residuals $\boldsymbol{e}$ of the model. If a model has lack-of-fit, there will be a systematic departure in the residual plot. Alternatively if a model has no lack-of-fit, the residual plot will appear as random noise. To visualize this description, the residual plots from the 45° bias test direction is seen in figure A-4 for the two types of PVC-coated polyester. The CF0700T 45° bias test is shown in A) where the systematic departure indicates that lack-of-fit is present. The VALMEX® 7318 45° bias test is shown in B), where the inherent randomness (especially at high displacements) indicates inherent variability in the experimental data. Patterns in the residual plot can be an indication of a case where it is best to improve the model. While a zero centered residual plot with random scatter could indicate lack-of-fit.

The CF0700T 45° bias test was described as an exceptionally good fit because the average residual was small relative to the data values. The residuals were on the order of

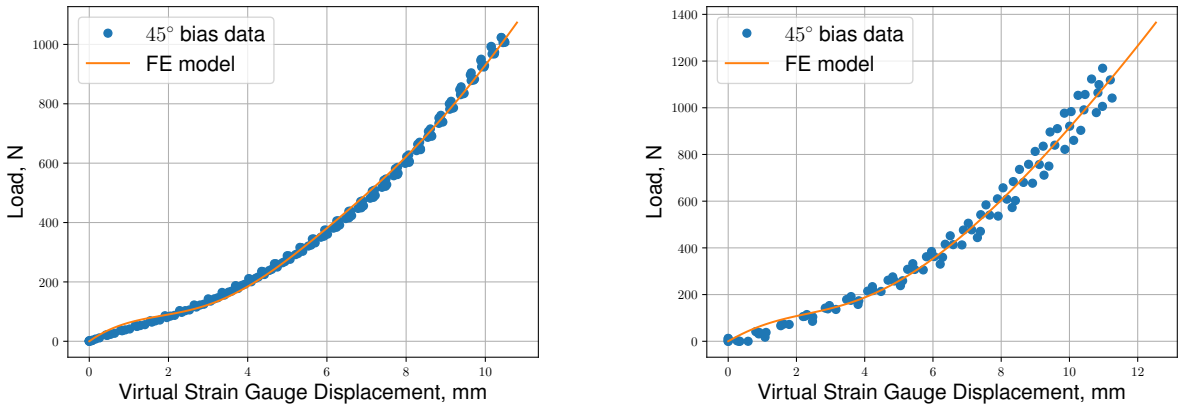

A CF0700T 45° bias test

B VALMEX® 7318 45° bias test

Figure A-3. The experimental data and final FE model results. The accuracy of the FE model depends on the material model and the uncertainty in the experimental data.

20 N, while the data had a maximum value around 1200 N. This demonstrates an example where the lack-of-fit test indicates that an existing model could be improved, despite being already considered a good fit. In this case a second order polynomial was used for the shear moduli and potentially a higher order polynomial would allow the model to better match the experimental response.

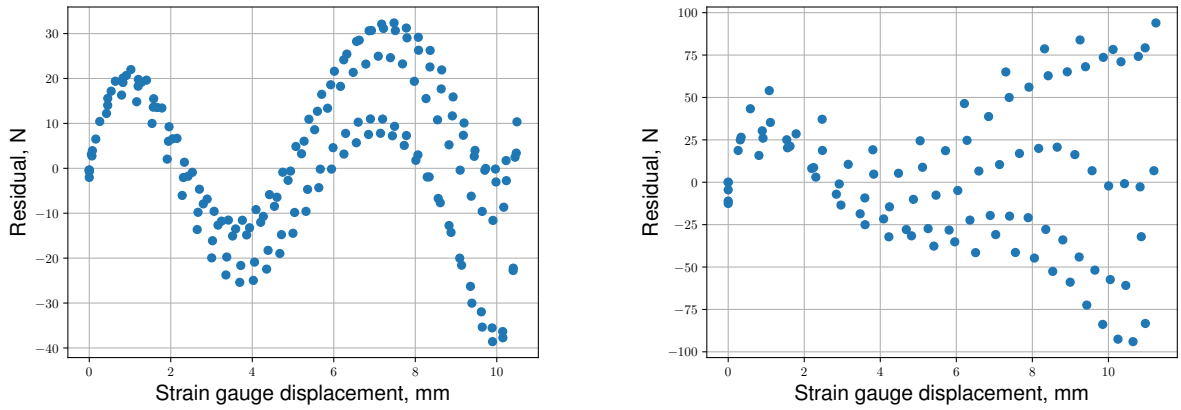

A CF0700T 45° bias test

B VALMEX® 7318 45° bias test

Figure A-4. Residual plots of 45° bias uniaxial test for two different PVC-coated polyesters. In A) the lack-of-fit test was failed, while B) passed the lack-of-fit test.

The Poisson's ratio for the CF0700T PVC-coated polyester is now considered as another material parameter calibration example [24]. A linear trend was fitted to the Poisson's ratio that varied with respect to the load, as seen in figure A-5. A lack-of-fit test ($F \approx 0.9$) indicates that the linear trend is an accepted model. The lack-of-fit test indicated that the major source of the variance was from the experimental data. In this case the only way to improve a trend to the linear Poisson's ratio model would be to reduce the variance in the experimental data. Attempting to use a better model for the trend, such as quadratic or cubic polynomials, will not gain much improvement in the overall accuracy. For instance the unbiased variance for the linear trend is $\hat{\sigma}^2 = 5.7 \times 10^{-}4$, quadratic trend is $\hat{\sigma}^2 = 5.7 \times 10^{-}4$, and for a cubic trend is $\hat{\sigma}^2 = 5.6 \times 10^{-}4$.

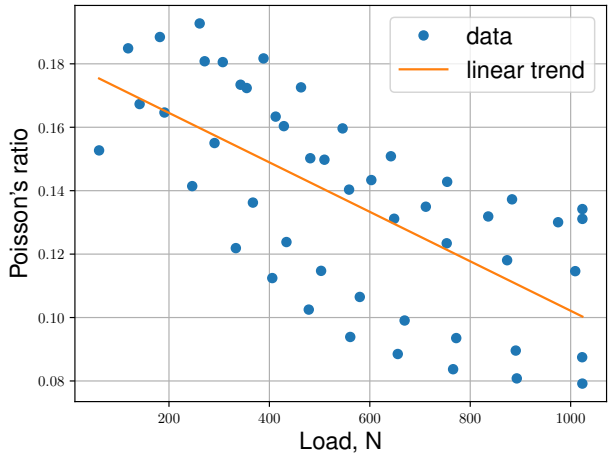

Figure A-5. Poisson's ratio as a function of the applied load for CF0700T PVC-coated polyester, with a linear trend fitted to the data.

It is worthwhile to consider that for these examples, conclusions as to whether to improve the model or data could have been drawn without a lack-of-fit test using visual methods. Though the lack-of-fit test serves as a basis to aid such decisions. Additonally it may be difficult to visualize high dimensional data, and thus it is anticipated that extensions of the lack-of-fit in high dimmensions may be useful when dealing with data that is difficult to visualize. Unfortunately the GSJ and Hart methods as proposed will require modification to be

extended to higher dimensions. If true replicates exist, a classical lack-of-fit test can be applied following Myers et al. regardless of the dimension of data [92].

A.5 Conclusion

A generalized lack-of-fit test was described that could be applied to experimental data when calibrating a material model. The F-statistic represented a comparison of the unbiased estimate of variance to the estimated noise within the data. Two methods, GSJ and Hart, were used to approximate the variance from the noise within experimental data for cases without true replicates. The GSJ method can be directly applied to data, while the Hart method requires a linear regression model. This gives the GSJ an advantage in simplicity. Though it was shown that the Hart method can be more accurate with fewer data points, provided that the regression model used closely resembles the true function. The lack-of-fit test can be used to indicate if the model, or the data has the largest potential for improvement.

The lack-of-fit tests were applied to a material calibration problem, in which a non-linear orthotropic model was used to describe PVC-coated polyester. It is worthwhile to note that the existing model was previously considered an excellent fit. Despite this, the lack-of-fit test indicated that one of the experimental responses was inadequately described by the model. This lack-of-fit could be visualized as a systematic departure in a residual plot. An interesting take away is that even if a material model is of exceptional fit, the material calibration parameters may fail the lack-of-fit test. In this case it would be recommenced to consider improving the model. Alternatively with the Poisson's ratio example, the lack-of-fit test indicates that the uncertainty in the experimental data should be reduced in order to predict a better trend.

APPENDIX B
ALGORITHM TO CALCULATE AREA BETWEEN TWO CURVES

The area of any simple (non self intersecting) quadrilateral can be expressed by Gauss's area formula (also known as the shoelace formula). Gauss's area formula for a simple quadrilateral is

$$A = \frac{1}{2}\left|x_1y_2 + x_2y_3 + x_3y_4 + x_4y_1 - x_2y_1 - x_3y_2 - x_4y_3 - x_1y_4\right| \tag{B-1}$$

where A is the area and (x_i, y_i) represents the vertices of the quadrilateral. It is worthwhile to note that any complex quadrilateral can become a simple quadrilateral by rearranging the order of the vertices.

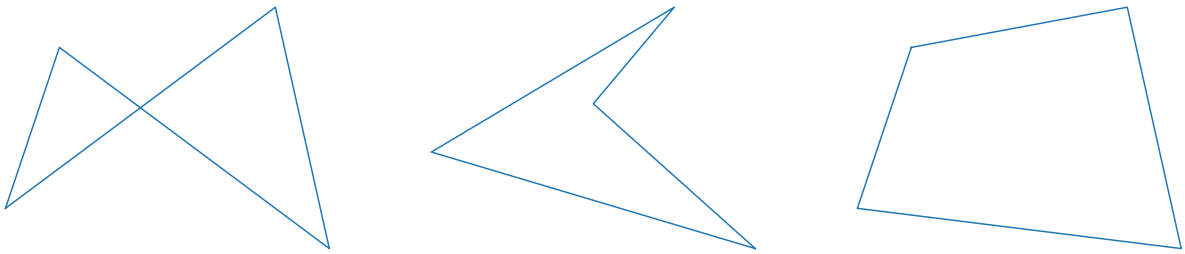

A Complex B Concave C Convex

Figure B-1. Examples of complex and simple quadrilaterals. A simple quadrilateral can be either concave or convex.

The interior angles of a quadrilateral can be used to detect whether a quadrilateral is simple or complex. Any simple quadrilateral will have a sum of interior angles that add up to $360°$. If all interior angles are less than $180°$, the simple quadrilateral is said to be convex. However if one interior angle is greater than $180°$, the simple quadrilateral is said to be concave. The interior angles of complex quadrilaterals will add up to $720°$. An example of a complex, concave, and convex quadrilaterals are shown in Fig. B-1.

The change of sign of cross products can be used to detect if a quadrilateral is complex (as an interpretation of the interior angles). Let's consider an arbitrary quadrilateral

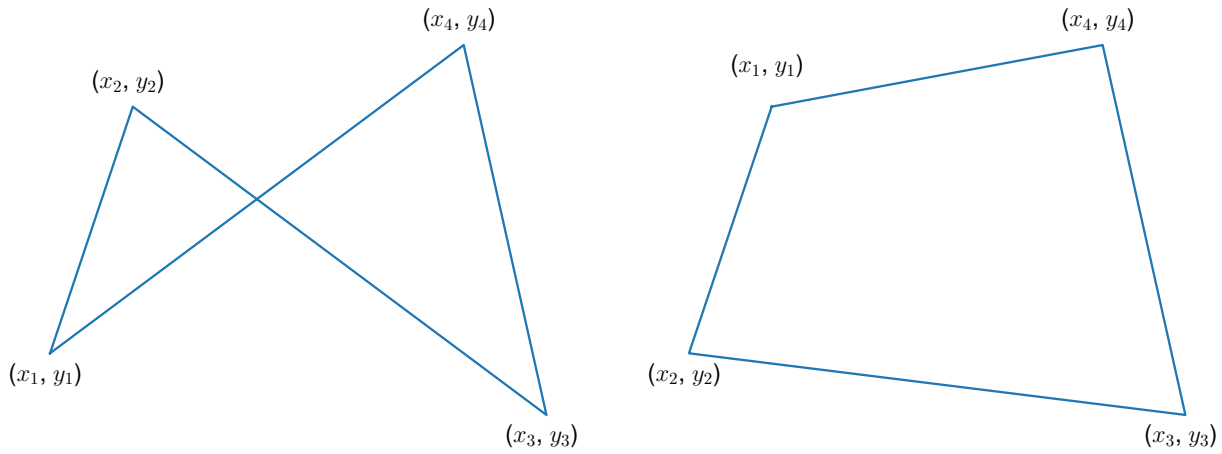

Figure B-2. Construction of simple quadrilaterals. By swapping the vertices of (x_1, y_1) with (x_2, y_2), the complex quadrilateral of A) becomes the simple quadrilateral in B).

represented by the following vectors:

$$\boldsymbol{AB} =< x_2 - x_1, y_2 - y_1 > \tag{B-2}$$

$$\boldsymbol{BC} =< x_3 - x_2, y_3 - y_2 > \tag{B-3}$$

$$\boldsymbol{CD} =< x_4 - x_3, y_4, -y_3 > \tag{B-4}$$

$$\boldsymbol{DA} =< x_1 - x_4, y_1 - y_4 > \tag{B-5}$$

The sign of the following cross products dictates whether a quadrilateral is self intersecting or not.

$$\boldsymbol{AB} \times \boldsymbol{BC} \tag{B-6}$$

$$\boldsymbol{BC} \times \boldsymbol{CD} \tag{B-7}$$

$$\boldsymbol{CD} \times \boldsymbol{DA} \tag{B-8}$$

$$\boldsymbol{DA} \times \boldsymbol{AB} \tag{B-9}$$

A complex quadrilateral exists if and only if two of the above cross products are negative and the other two are positive. A simple quadrilateral will have at least three of the same sign cross

products. The vertices of a complex quadrilateral can be used to create a simple quadrilateral simply by rearranging the order as shown in Fig. B-2.

A pseudocode algorithm to compute the effective area between two curves is presented as Algorithm 1. The algorithm first ensures that the two curves have the same number of data points. If not, points are added to the curve with fewer points. The total number of quadrilaterals created will be one less than the number of data points. Two consecutive points are taken from each curve, acting as the vertices of the quadrilateral. Note that the order of the data points which represent the curve is important. The first quadrilateral uses the first and second data point from each curve, the second quadrilateral uses the second and third data point from each curve and so forth. Each quadrilateral is then determined to be either simple or complex. If the quadrilateral is complex, the vertices are reordered until the quadrilateral becomes simple. The area of each simple quadrilateral is calculated using the Gauss area formula, and all quadrilateral areas are summed to give an effective area between curves.

Algorithm 1: Compute the effective area between curveA and curveB.

```
1  function areaBetweenCurves (curveA, curveB);
   Input  : Data of curveA and curveB.
   Output: Area between curveA and curveB.
2  # the length() function returns the number of data points
3  if length(curveA) < length(curveB) then
4  |   A = curveA;
5  |   B = curveB;
6  else
7  |   B = curveA;
8  |   A = curveB;
9  end
10 while length(A) < length(B) do
11 |   Compute distance between every two consecutive points of A;
12 |   Find the two points that generate the max distance;
13 |   Create a point that bisects these two points;
14 |   Add the bisect point to A in between the two points;
15 end
16 n = length(A) -1; # compute the number of quadrilaterals;
17 areas = zeros (n); # initiate zeros array for areas;
18 for i = 1 to n do
19 |   # Assemble quadrilateral;
20 |   quad = [A[i], A[i+1], B[i+1], B[i]];
21 |   if quad is not simple then
22 |   |   Rearrange the order of vertices until quad is simple;
23 |   end
24 |   # Calculate the Gauss/shoelace area of the quadrilateral;
25 |   areas[i] = gaussArea(quad);
26 end
27 # Return the summation of quadrilateral areas;
28 return sum(areas);
```

APPENDIX C
LINE PLOT FOR KINEMATIC HARDENING PROBLEM

Line plots were performed in between data points of the kinematic hardening problem to visualize the design space with different similarity measures. All objective function values were normalized using

$$z_i = \frac{x_i - \min(\boldsymbol{x})}{\max(\boldsymbol{x}) - \min(\boldsymbol{x})} \tag{C-1}$$

such that zero is the best found objective function, and one is the worst. The line plots without noise are presented in Fig. C-1, and the line plots with noise are presented in Fig. C-2. The line plots help to illustrate the state of the design space (for each measure of similarity) between the optima found. Additionally it appears that the Area and Curve Length methods produced smoother design spaces than the PCM and Discrete Fréchet methods. The line plots were calculated from the results of the first SDRM optimization result, and sometimes display a local optimum that the SDRM failed to find.

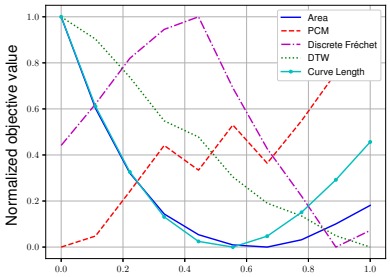

A from PCM to Area

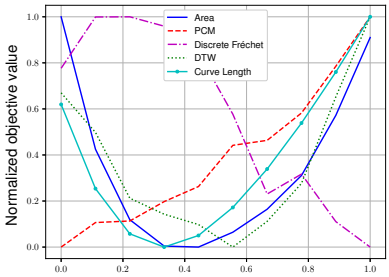

B from PCM to Discrete Fréchet

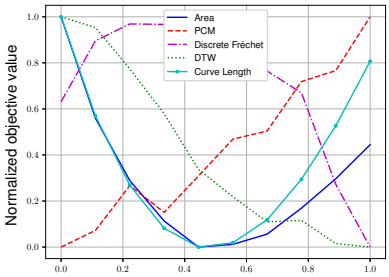

C from PCM to DTW

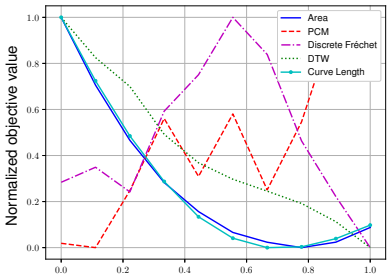

D from PCM to Curve Length

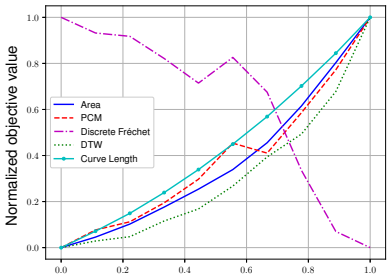

E from Area to Discrete Fréchet

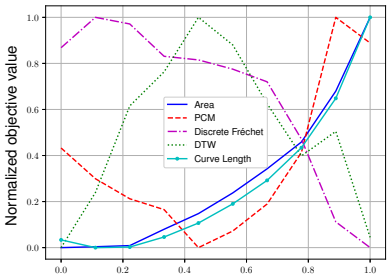

F from Area to DTW

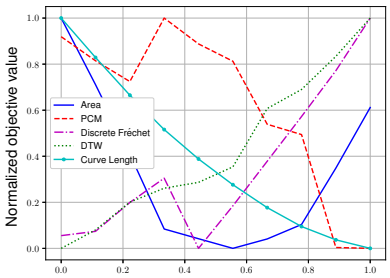

G from Area to Curve Length

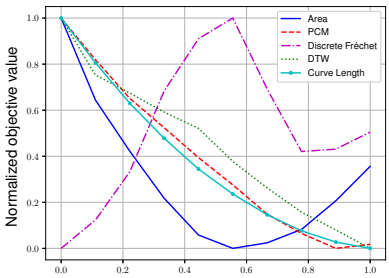

H from Discrete Fréchet to DTW

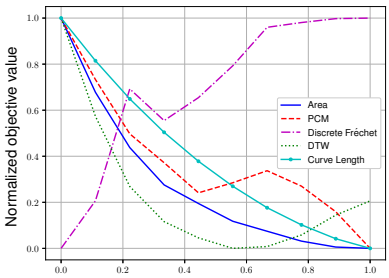

I from Discrete Fréchet to Curve Length

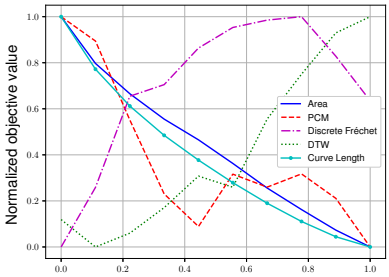

J from DTW to Curve Length

Figure C-1. Without noise: Line plot with normalized objective values from one objective optimum to another objective optimum.

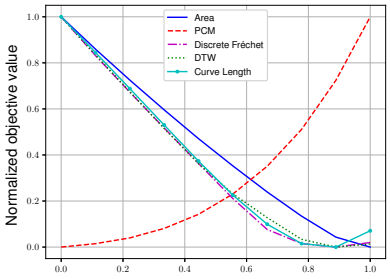

A from PCM to Area

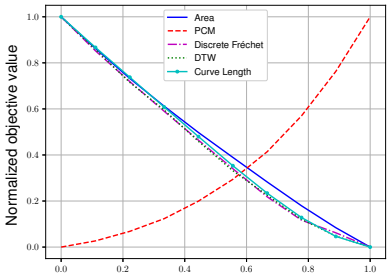

B from PCM to Discrete Fréchet

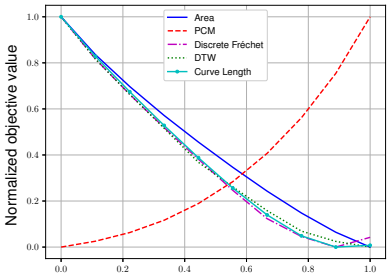

C from PCM to DTW

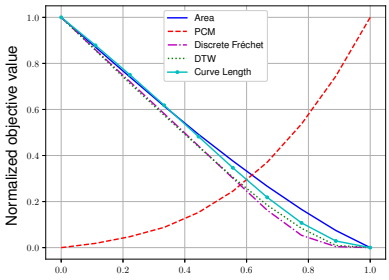

D from PCM to Curve Length

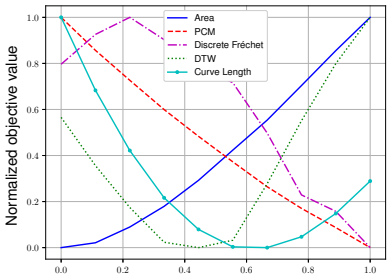

E from Area to Discrete Fréchet

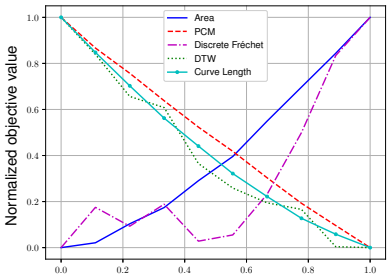

F from Area to DTW

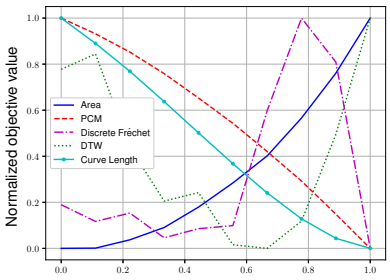

G from Area to Curve Length

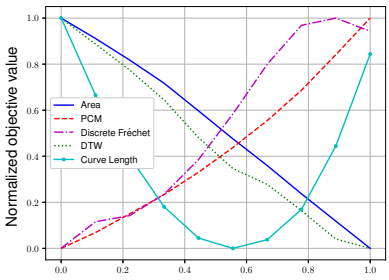

H from Discrete Fréchet to DTW

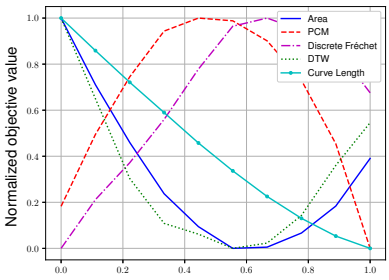

I from Discrete Fréchet to Curve Length

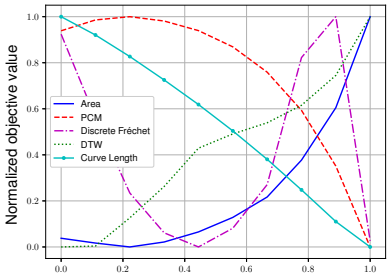

J from DTW to Curve Length

Figure C-2. With noise: Line plot with normalized objective values from one objective optimum to another objective optimum.

APPENDIX D
KINEMATIC HARDENING RESULTS

It is difficult to recognize the differences between similarity measures for the kinematic hardening parameter identification from section 3.3. This appendix section shows the results from section 3.3 for the individual hysteresis loops. The results of the hysteresis curve from the parameter identification can be seen in Figs. D-1- D-5, and the results with noise in Figs. D-6- D-10.

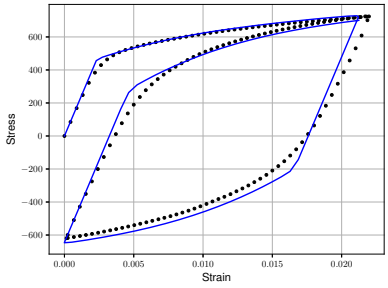

A first cycle

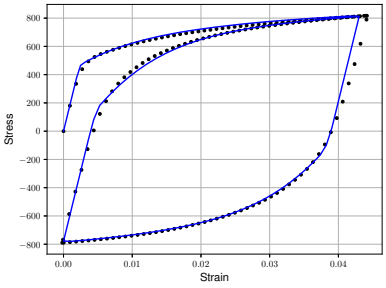

B second cycle

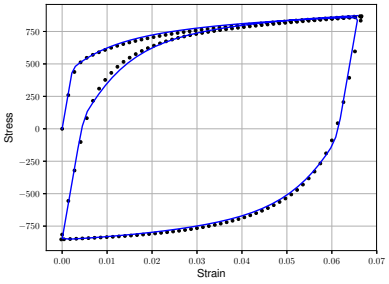

C third cycle

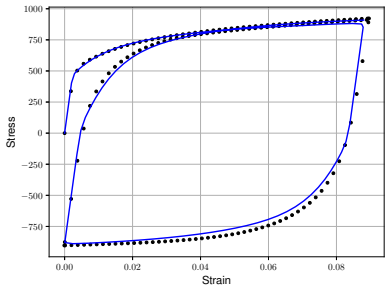

D fourth cycle

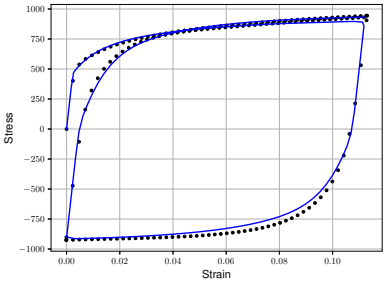

E fifth cycle

Figure D-1. Area results for kinematic hardening parameter identification.

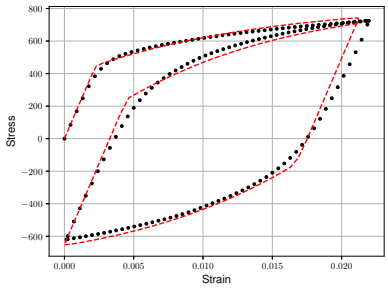

A first cycle

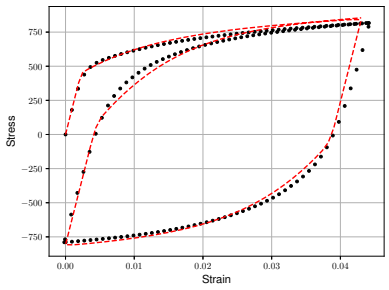

B second cycle

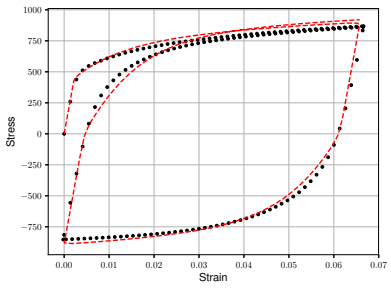

C third cycle

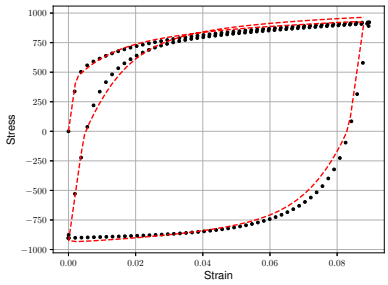

D fourth cycle

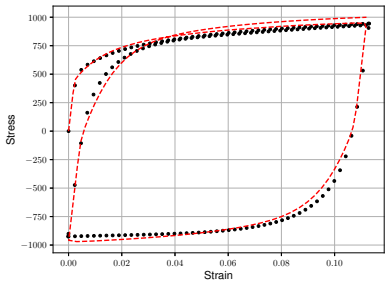

E fifth cycle

Figure D-2. PCM results for kinematic hardening parameter identification.

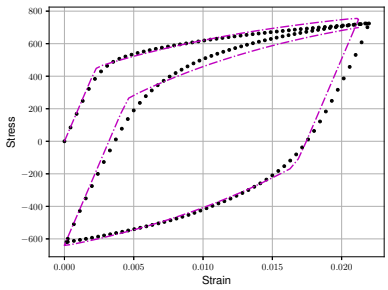

A first cycle

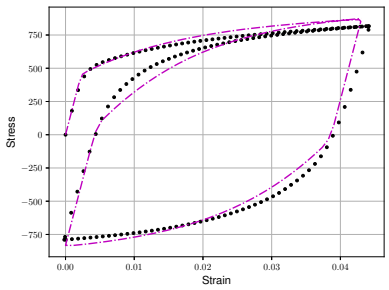

B second cycle

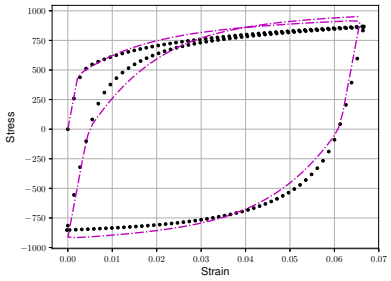

C third cycle

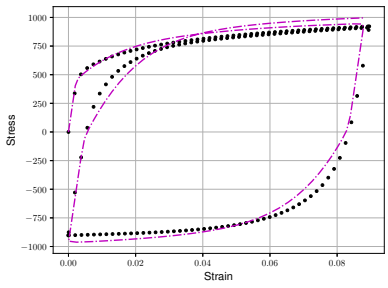

D fourth cycle

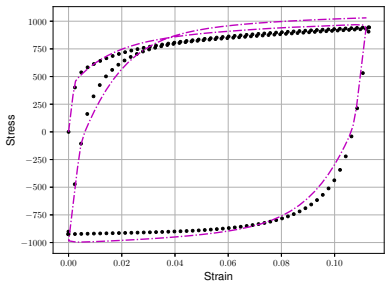

E fifth cycle

Figure D-3. Discrete Fréchet results for kinematic hardening parameter identification.

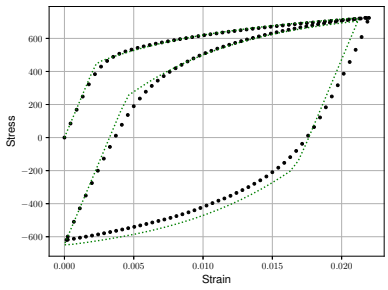

A first cycle

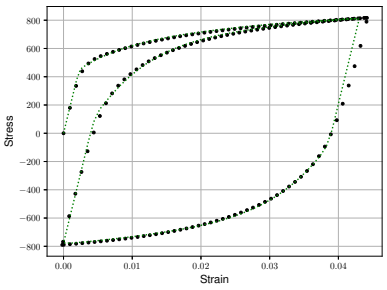

B second cycle

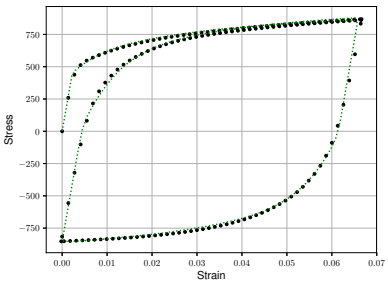

C third cycle

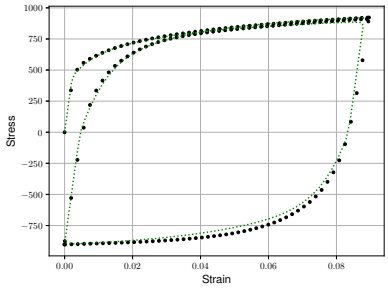

D fourth cycle

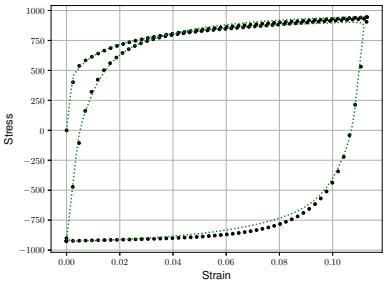

E fifth cycle

Figure D-4. DTW results for kinematic hardening parameter identification.

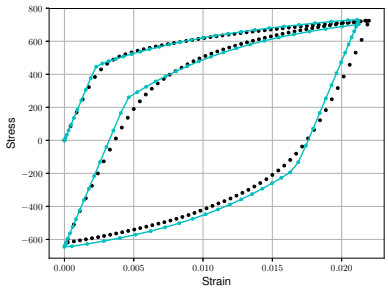

A first cycle

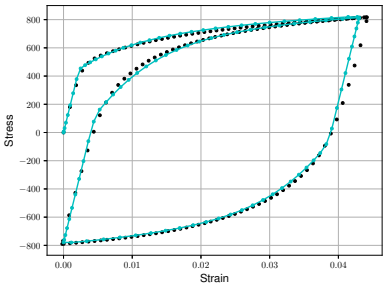

B second cycle

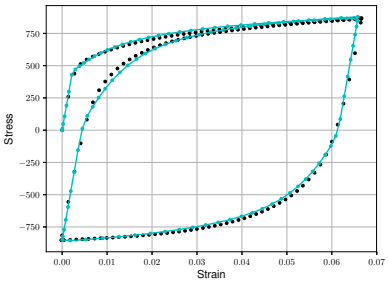

C third cycle

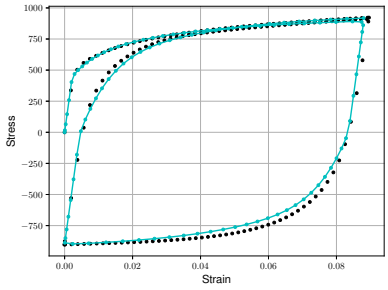

D fourth cycle

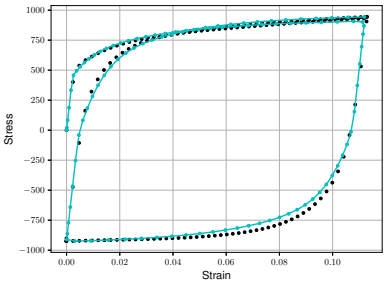

E fifth cycle

Figure D-5. Curve Length results for kinematic hardening parameter identification.

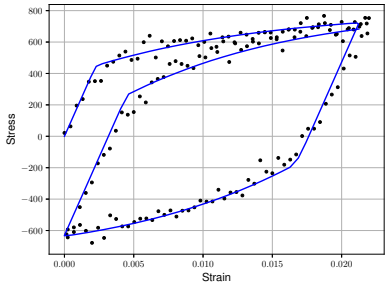

A first cycle

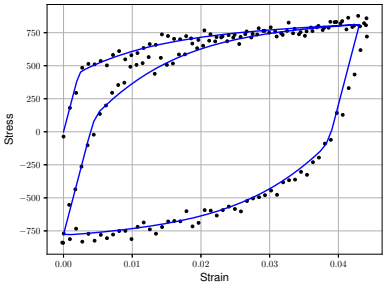

B second cycle

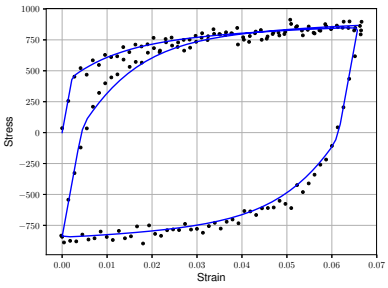

C third cycle

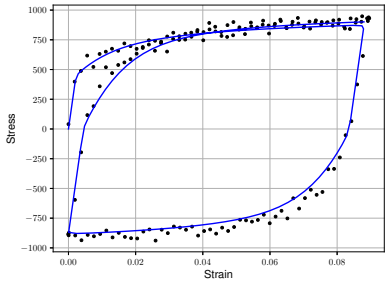

D fourth cycle

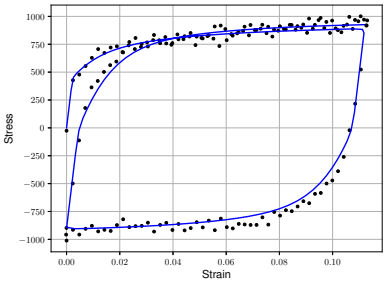

E fifth cycle

Figure D-6. Area results with noise for kinematic hardening parameter identification.

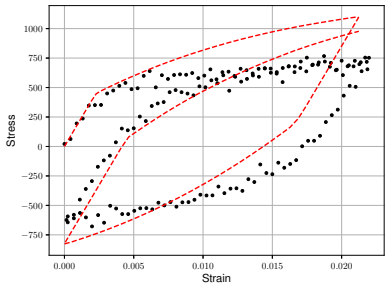

A first cycle

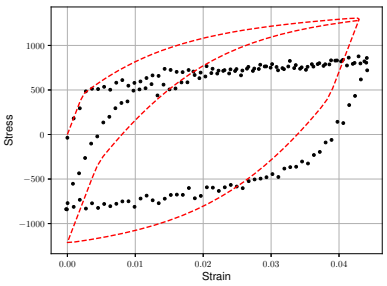

B second cycle

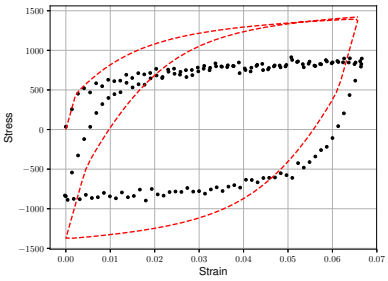

C third cycle

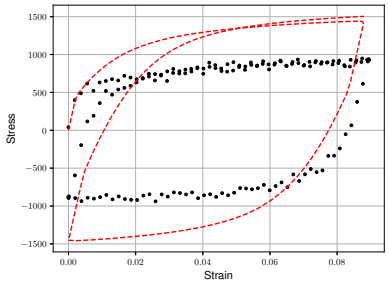

D fourth cycle

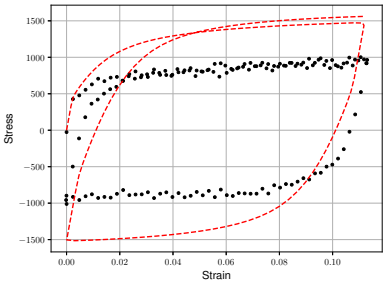

E fifth cycle

Figure D-7. PCM results with noise for kinematic hardening parameter identification.

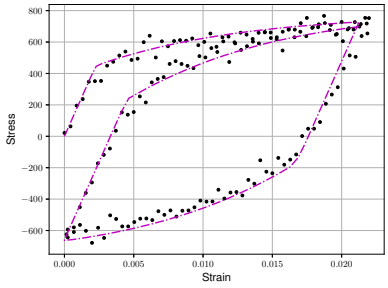

A first cycle

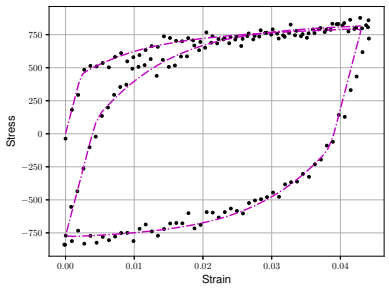

B second cycle

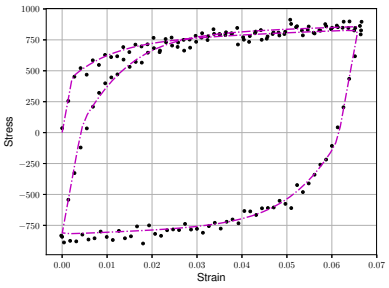

C third cycle

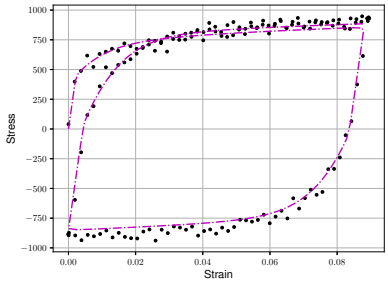

D fourth cycle

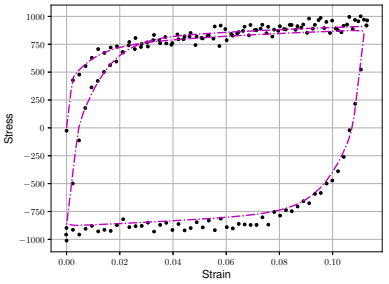

E fifth cycle

Figure D-8. Discrete Fréchet results with noise for kinematic hardening parameter identification.

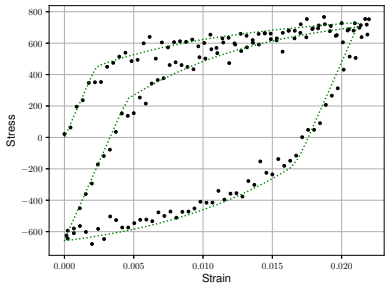

A first cycle

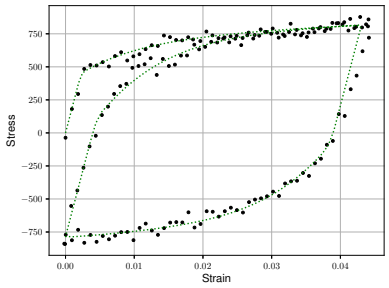

B second cycle

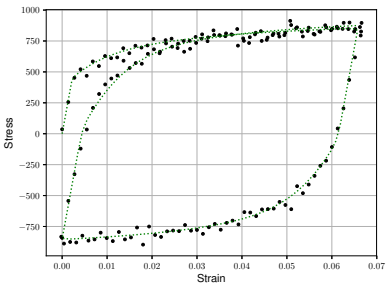

C third cycle

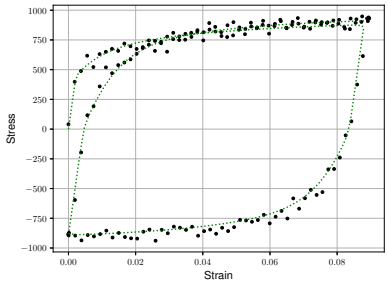

D fourth cycle

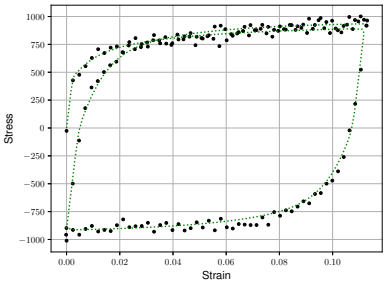

E fifth cycle

Figure D-9. DTW results with noise for kinematic hardening parameter identification.

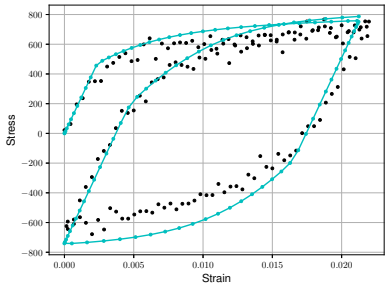

A first cycle

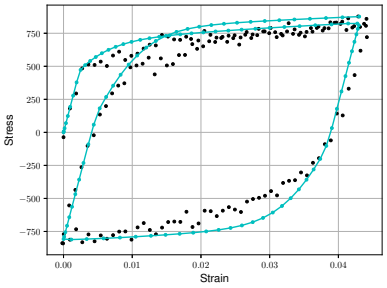

B second cycle

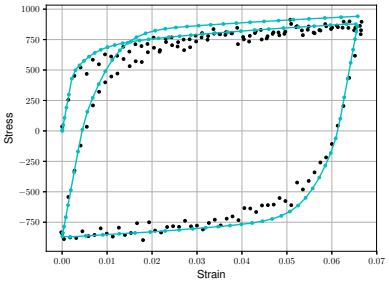

C third cycle

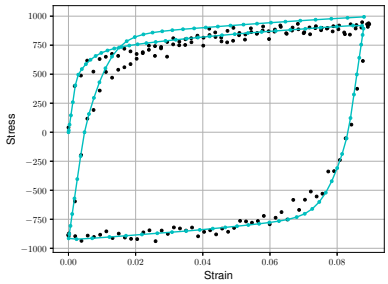

D fourth cycle

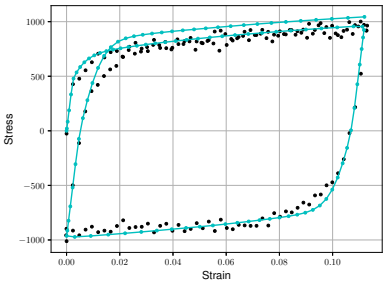

E fifth cycle

Figure D-10. Curve Length results with noise for kinematic hardening parameter identification.

REFERENCES

[1] D. S. Schnur and N. Zabaras, "An inverse method for determining elastic material properties and a material interface," *International Journal for Numerical Methods in Engineering*, vol. 33, no. 10, pp. 2039–2057, 1992, ISSN: 1097-0207. DOI: 10.1002/nme.1620331004.

[2] G. Lovato, F. Moret, P. Le Gallo, G. Cailletaud, and P. Pilvin, "Determination of brazed joint constitutive law by inverse method," *Le Journal de Physique IV*, vol. 3, no. C7, pp. C7–1135, 1993.

[3] J. C. Gelin and O. Ghouati, "An inverse method for determining viscoplastic properties of aluminium alloys," *Journal of Materials Processing Technology*, vol. 45, no. 1, pp. 435–440, 1994, ISSN: 0924-0136. DOI: https://doi.org/10.1016/0924-0136(94)90378-6.

[4] O. Sigmund, "Materials with prescribed constitutive parameters: An inverse homogenization problem," *International Journal of Solids and Structures*, vol. 31, no. 17, pp. 2313–2329, 1994, ISSN: 0020-7683. DOI: https://doi.org/10.1016/0020-7683(94)90154-6.

[5] G. Cailletaud and P. Pilvin, "Identification and inverse problems related to material behaviour," *Inverse problems in engineering mechanics*, vol. 1, pp. 79–86, 1994.

[6] M. Rabahallah, T. Balan, S. Bouvier, B. Bacroix, F. Barlat, K. Chung, and C. Teodosiu, "Parameter identification of advanced plastic strain rate potentials and impact on plastic anisotropy prediction," *International Journal of Plasticity*, vol. 25, no. 3, pp. 491–512, 2009, ISSN: 0749-6419. DOI: http://dx.doi.org/10.1016/j.ijplas.2008.03.006.

[7] N. Souto, A. Andrade-Campos, and S. Thuillier, "Material parameter identification within an integrated methodology considering anisotropy, hardening and rupture," *Journal of Materials Processing Technology*, vol. 220, pp. 157–172, 2015.

[8] F. Yoshida, M. Urabe, R. Hino, and V. V. Toropov, "Inverse approach to identification of material parameters of cyclic elasto-plasticity for component layers of a bimetallic sheet," *International Journal of Plasticity*, vol. 19, no. 12, pp. 2149–2170, 2003, ISSN: 0749-6419. DOI: http://dx.doi.org/10.1016/S0749-6419(03)00063-9.

[9] F. Bosi and S. Pellegrino, "Nonlinear thermomechanical response and constitutive modeling of viscoelastic polyethylene membranes," *Mechanics of Materials*, vol. 117, pp. 9–21, 2018, ISSN: 0167-6636. DOI: https://doi.org/10.1016/j.mechmat.2017.10.004.

[10] R. Storn and K. Price, "Differential Evolution – A Simple and Efficient Heuristic for global Optimization over Continuous Spaces," *Journal of Global Optimization*, vol. 11, no. 4, pp. 341–359, Dec. 1997, ISSN: 1573-2916. DOI: 10.1023/A:1008202821328.

[11] D. H. Wolpert and W. G. Macready, "No free lunch theorems for optimization," *IEEE Transactions on Evolutionary Computation*, vol. 1, no. 1, pp. 67–82, Apr. 1997, ISSN: 1089-778X. DOI: 10.1109/4235.585893.

[12] N. Stander and K. J. Craig, "On the robustness of a simple domain reduction scheme for simulation-based optimization," *Engineering Computations*, vol. 19, no. 4, pp. 431–450, 2002. DOI: 10.1108/02644400210430190.

[13] B. M. Chaparro, S. Thuillier, L. F. Menezes, P. Y. Manach, and J. V. Fernandes, "Material parameters identification: Gradient-based, genetic and hybrid optimization algorithms," *Computational Materials Science*, vol. 44, no. 2, pp. 339–346, 2008, ISSN: 0927-0256. DOI: https://doi.org/10.1016/j.commatsci.2008.03.028.

[14] N. Stander, W. Roux, T. Goel, T. Eggleston, and K. Craig, *LS-OPT ® User's Manual - A Design Optimization and Probabilistic Analysis Tool*. 2015.

[15] T. C. Chu, W. F. Ranson, and M. A. Sutton, "Applications of digital-image-correlation techniques to experimental mechanics," *Experimental Mechanics*, vol. 25, no. 3, pp. 232–244, 1985, ISSN: 1741-2765. DOI: 10.1007/BF02325092.

[16] C. Galliot and R. H. Luchsinger, "The shear ramp: A new test method for the investigation of coated fabric shear behaviour – Part II: Experimental validation," *Composites Part A: Applied Science and Manufacturing*, vol. 41, no. 12, pp. 1750–1759, Dec. 2010. DOI: 10.1016/j.compositesa.2010.08.014.

[17] T. Garbowski, G. Maier, and G. Novati, "On calibration of orthotropic elastic-plastic constitutive models for paper foils by biaxial tests and inverse analyses," *Structural and Multidisciplinary Optimization*, vol. 46, no. 1, pp. 111–128, Dec. 2011, ISSN: 1615-147X. DOI: 10.1007/s00158-011-0747-3.

[18] G. Machado, D. Favier, and G. Chagnon, "Membrane curvatures and stress-strain full fields of axisymmetric bulge tests from 3D-DIC measurements. Theory and validation on virtual and experimental results," *Experimental mechanics*, vol. 52, no. 7, pp. 865–880, 2012.

[19] T. K. Tonge, L. S. Atlan, L. M. Voo, and T. D. Nguyen, "Full-field bulge test for planar anisotropic tissues: Part I – Experimental methods applied to human skin tissue," *Acta Biomaterialia*, vol. 9, no. 4, pp. 5913–5925, 2013, ISSN: 1742-7061. DOI: https://doi.org/10.1016/j.actbio.2012.11.035.

[20] T. H. Becker, M. Mostafavi, R. B. Tait, and T. J. Marrow, "An approach to calculate the J-integral by digital image correlation displacement field measurement," *Fatigue & Fracture of Engineering Materials & Structures*, vol. 35, no. 10, pp. 971–984, 2012. DOI: 10.1111/j.1460-2695.2012.01685.x.

[21] B. J. Murienne and T. D. Nguyen, "A comparison of 2D and 3D digital image correlation for a membrane under inflation," *Optics and Lasers in Engineering*, vol. 77, pp. 92–99, 2016, ISSN: 0143-8166. DOI: https://doi.org/10.1016/j.optlaseng.2015.07.013.

[22] J. Cao and J. Lin, "A study on formulation of objective functions for determining material models," *International Journal of Mechanical Sciences*, vol. 50, no. 2, pp. 193–204, 2008, ISSN: 0020-7403. DOI: https://doi.org/10.1016/j.ijmecsci.2007.07.003.

[23] A. Andrade-Campos, R. De-Carvalho, and R. A. F. Valente, "Novel criteria for determination of material model parameters," *International Journal of Mechanical Sciences*, vol. 54, no. 1, pp. 294–305, 2012, ISSN: 0020-7403. DOI: https://doi.org/10.1016/j.ijmecsci.2011.11.010.

[24] C. F. Jekel, G. Venter, and M. P. Venter, "Modeling PVC-coated polyester as a hypoelastic non-linear orthotropic material," *Composite Structures*, vol. 161, pp. 51–64, Feb. 2017, ISSN: 0263-8223. DOI: http://dx.doi.org/10.1016/j.compstruct.2016.11.019.

[25] P. V. Cavallaro, A. M. Sadegh, and C. J. Quigley, "Decrimping Behavior of Uncoated Plain-woven Fabrics Subjected to Combined Biaxial Tension and Shear Stresses," *Textile Research Journal*, vol. 77, no. 6, pp. 403–416, Jun. 2007, ISSN: 0040-5175. DOI: 10.1177/0040517507080258.

[26] R. H. Luchsinger, A. Sydow, and R. Crettol, "Structural behavior of asymmetric spindle-shaped Tensairity girders under bending loads," *Thin-Walled Structures*, vol. 49, no. 9, pp. 1045–1053, 2011. DOI: 10.1016/j.tws.2011.03.012.

[27] T.-T. Nguyen, S. Ronel, M. Massenzio, K. L. Apedo, and E. Jacquelin, "Analytical buckling analysis of an inflatable beam made of orthotropic technical textiles," *Thin-Walled Structures*, vol. 51, no. 0, pp. 186–200, Feb. 2012, ISSN: 0263-8231. DOI: http://dx.doi.org/10.1016/j.tws.2011.10.017.

[28] C. Galliot and R. H. Luchsinger, "Structural behavior of symmetric spindle-shaped Tensairity girders with reinforced chord coupling," *Engineering Structures*, vol. 56, pp. 407–416, 2013. DOI: 10.1016/j.engstruct.2013.05.023.

[29] P. V. Cavallaro, M. E. Johnson, and A. M. Sadegh, "Mechanics of plain-woven fabrics for inflated structures," *Composite Structures*, vol. 61, no. 4, pp. 375–393, 2003. DOI: 10.1016/S0263-8223(03)00054-0.

[30] Gosling and Bridgens, "Material Testing & Computational Mechanics - A New Philosophy For Architectural Fabrics," en, *International Journal of Space Structures*, vol. 23, no. 4, pp. 215–232, Nov. 2008, ISSN: 0266-3511. DOI: 10.1260/026635108786959870.

[31] S. Chen, X. Ding, and H. Yi, "On the Anisotropic Tensile Behaviors of Flexible Polyvinyl Chloride-coated Fabrics," *Textile Research Journal*, vol. 77, no. 6, pp. 369–374, Jun. 2007, ISSN: 0040-5175. DOI: 10.1177/0040517507078791.

[32] P. Kłosowski, W. Komar, and K. Woźnica, "Finite element description of nonlinear viscoelastic behaviour of technical fabric," *Construction and Building Materials*, vol. 23, no. 2, pp. 1133–1140, Feb. 2009, ISSN: 09500618. DOI: 10.1016/j.conbuildmat.2008.06.002.

[33] C. Galliot and R. Luchsinger, "A simple model describing the non-linear biaxial tensile behaviour of PVC-coated polyester fabrics for use in finite element analysis," *Composite Structures*, vol. 90, no. 4, pp. 438–447, 2009, ISSN: 02638223. DOI: 10.1016/j.compstruct.2009.04.016.

[34] A. Ambroziak and P. Kłosowski, "Mechanical properties for preliminary design of structures made from PVC coated fabric," *Construction and Building Materials*, vol. 50, pp. 74–81, Jan. 2014, ISSN: 09500618. DOI: 10.1016/j.conbuildmat.2013.08.060.

[35] MSC Marc, *Volume A : Theory and User Information*. MSC Software Corporation, 2014.

[36] ASTM D751 - 06, *Standard Test Methods for Coated Fabrics*, January. 2011.

[37] LaVision GmbH, *Product-Manual DaVis 8.2 Software*. Göttingen, Germany, 2014.

[38] Vanderplaats Research & Development Inc., *DOT Users manual*, 5.X. Colorado Springs, CO, 2001.

[39] C. F. Jekel, G. Venter, M. P. Venter, N. Stander, and R. T. Haftka, "Similarity measures for identifying material parameters from hysteresis loops using inverse analysis," *International Journal of Material Forming*, Jul. 2018, ISSN: 1960-6214. DOI: 10.1007/s12289-018-1421-8.

[40] M. C. Boyce and E. M. Arruda, "Constitutive Models of Rubber Elasticity: A Review," *Rubber Chemistry and Technology*, vol. 73, no. 3, pp. 504–523, 2000. DOI: 10.5254/1.3547602.

[41] M. Grédiac, F. Pierron, and A. Vautrin, "The Iosipescu in-plane shear test applied to composites: A new approach based on displacement field processing," *Composites Science and Technology*, vol. 51, no. 3, pp. 409–417, 1994, ISSN: 0266-3538. DOI: https://doi.org/10.1016/0266-3538(94)90109-0.

[42] M. Grédiac, F. Pierron, S. Avril, and E. Toussaint, "The Virtual Fields Method for Extracting Constitutive Parameters From Full-Field Measurements: a Review," *Strain*, vol. 42, no. 4, pp. 233–253, 2006, ISSN: 1475-1305. DOI: 10.1111/j.1475-1305.2006.tb01504.x.

[43] D. Lederer, H. Igarashi, A. Kost, and T. Honma, *On the parameter identification and application of the Jiles-Atherton hysteresis model for numerical modelling of measured characteristics*, 1999. DOI: 10.1109/20.767167.

[44] H. Haddadi, S. Bouvier, M. Banu, C. Maier, and C. Teodosiu, "Towards an accurate description of the anisotropic behaviour of sheet metals under large plastic deformations: Modelling, numerical analysis and identification," *International Journal of Plasticity*, vol. 22, no. 12, pp. 2226–2271, 2006, ISSN: 0749-6419. DOI: 10.1016/j.ijplas.2006.03.010.

[45] P.-A. Eggertsen and K. Mattiasson, "On the identification of kinematic hardening material parameters for accurate springback predictions," *International Journal of Material Forming*, vol. 4, no. 2, pp. 103–120, 2011, ISSN: 1960-6214. DOI: 10.1007/s12289-010-1014-7.

[46] T. Harth, S. Schwan, J. Lehn, and F. G. Kollmann, "Identification of material parameters for inelastic constitutive models: statistical analysis and design of experiments," *International Journal of Plasticity*, vol. 20, no. 8, pp. 1403–1440, 2004, ISSN: 0749-6419. DOI: http://dx.doi.org/10.1016/j.ijplas.2003.11.001.

[47] R. De-Carvalho, R. A. F. Valente, and A. Andrade-Campos, "On the Objective Function Evaluation in Parameter Identification of Material Constitutive Models - Single-point or FE Analysis," *International Journal of Material Forming*, vol. 3, no. 1, pp. 33–36, 2010, ISSN: 1960-6214. DOI: 10.1007/s12289-010-0700-9.

[48] F. Yoshida and T. Uemori, "A model of large-strain cyclic plasticity describing the Bauschinger effect and workhardening stagnation," *International Journal of Plasticity*, vol. 18, no. 5, pp. 661–686, 2002, ISSN: 0749-6419. DOI: http://dx.doi.org/10.1016/S0749-6419(01)00050-X.

[49] D. Kim, F. Barlat, S. Bouvier, M. Rabahallah, T. Balan, and K. Chung, "Non-quadratic anisotropic potentials based on linear transformation of plastic strain rate," *International Journal of Plasticity*, vol. 23, no. 8, pp. 1380–1399, 2007, ISSN: 0749-6419. DOI: http://dx.doi.org/10.1016/j.ijplas.2007.01.006.

[50] M. Gruber, N. Lebaal, S. Roth, N. Harb, P. Sterionow, and F. Peyraut, "Parameter identification of hardening laws for bulk metal forming using experimental and numerical approach," *International Journal of Material Forming*, vol. 9, no. 1, pp. 21–33, 2016, ISSN: 1960-6214. DOI: 10.1007/s12289-014-1196-5.

[51] H. ul Hassan, F. Maqbool, A. Güner, A. Hartmaier, N. Ben Khalifa, and A. E. Tekkaya, "Springback prediction and reduction in deep drawing under influence of unloading modulus degradation," *International Journal of Material Forming*, vol. 9, no. 5, pp. 619–633, Nov. 2016, ISSN: 1960-6214. DOI: 10.1007/s12289-015-1248-5.

[52] E. Markiewicz and B. Langrand, "Characterisation and Parameters Identification of Materials Constitutive and Damage Models: From Normalised Direct Approach to Most Advanced Inverse Problem Resolution," *Procedia Engineering*, vol. 173, pp. 33–40, 2017, ISSN: 1877-7058. DOI: https://doi.org/10.1016/j.proeng.2016.12.016.

[53] P. A. L. S. Martins, R. M. Natal Jorge, and A. J. M. Ferreira, "A Comparative Study of Several Material Models for Prediction of Hyperelastic Properties: Application to Silicone-Rubber and Soft Tissues," *Strain*, vol. 42, no. 3, pp. 135–147, 2006, ISSN: 1475-1305. DOI: 10.1111/j.1475-1305.2006.00257.x.

[54] O. T. Bruhns and D. K. Anding, "On the simultaneous estimation of model parameters used in constitutive laws for inelastic material behaviour," *International Journal of*

Plasticity, vol. 15, no. 12, pp. 1311–1340, 1999, ISSN: 0749-6419. DOI: http://dx.doi.org/10.1016/S0749-6419(99)00046-7.

[55] K. Witowski and N. Stander, "Parameter Identification of Hysteretic Models Using Partial Curve Mapping," *12th AIAA Aviation Technology, Integration, and Operations (ATIO) Conference and 14th AIAA/ISSMO Multidisciplinary Analysis and Optimization Conference*, Aviation Technology, Integration, and Operations (ATIO) Conferences, Sep. 2012. DOI: doi:10.2514/6.2012-5580.

[56] M. P. Venter and G. Venter, "Simple implementation of plain woven polypropylene fabric," *Journal of Industrial Textiles*, Aug. 2016. DOI: 10.1177/1528083716665627.

[57] M. M. Fréchet, "Sur quelques points du calcul fonctionnel," *Rendiconti del Circolo Matematico di Palermo (1884-1940)*, vol. 22, no. 1, pp. 1–72, 1906.

[58] T. Eiter and H. Mannila, "Computing discrete Fréchet distance," Tech. Rep., 1994.

[59] A. Driemel, S. Har-Peled, and C. Wenk, "Approximating the Fréchet Distance for Realistic Curves in Near Linear Time," *Discrete & Computational Geometry*, vol. 48, no. 1, pp. 94–127, 2012, ISSN: 1432-0444. DOI: 10.1007/s00454-012-9402-z.

[60] K. Bringmann, *Why Walking the Dog Takes Time: Frechet Distance Has No Strongly Subquadratic Algorithms Unless SETH Fails*, 2014. DOI: 10.1109/FOCS.2014.76.

[61] S. L. Seyler, A. Kumar, M. F. Thorpe, and O. Beckstein, "Path Similarity Analysis: A Method for Quantifying Macromolecular Pathways," *PLOS Computational Biology*, vol. 11, no. 10, pp. 1–37, 2015. DOI: 10.1371/journal.pcbi.1004568.

[62] H. Alt and M. Godau, "Computing the Fréchet Distance Between Two Polygonal Curves," *International Journal of Computational Geometry & Applications*, vol. 05, no. 01n02, pp. 75–91, 1995. DOI: 10.1142/S0218195995000064.

[63] D. J. Berndt and J. Clifford, "Using Dynamic Time Warping to Find Patterns in Time Series," in *Proceedings of the 3rd International Conference on Knowledge Discovery and Data Mining*, ser. AAAIWS'94, AAAI Press, 1994, pp. 359–370.

[64] F. Petitjean, A. Ketterlin, and P. Gançarski, "A global averaging method for dynamic time warping, with applications to clustering," *Pattern Recognition*, vol. 44, no. 3, pp. 678–693, 2011, ISSN: 0031-3203. DOI: https://doi.org/10.1016/j.patcog.2010.09.013.

[65] T. Giorgino, "Computing and Visualizing Dynamic Time Warping Alignments in R: The dtw Package," *Journal of Statistical Software; Vol 1, Issue 7 (2009)*, Aug. 2009.

[66] S. Salvador and P. Chan, "Toward Accurate Dynamic Time Warping in Linear Time and Space," *Intell. Data Anal.*, vol. 11, no. 5, pp. 561–580, Oct. 2007, ISSN: 1088-467X.

[67] Livermore Software Technology Corporation, "*MAT KINEMATIC HARDENING TRANSVERSELY ANISOTROPIC," in *LS-DYNA Keyword User's Manual Volume II Material Models*, 2016, pp. 635–646.

[68] P. Tormene, T. Giorgino, S. Quaglini, and M. Stefanelli, "Matching incomplete time series with dynamic time warping: an algorithm and an application to post-stroke rehabilitation," *Artificial Intelligence in Medicine*, vol. 45, no. 1, pp. 11–34, 2009, ISSN: 0933-3657. DOI: https://doi.org/10.1016/j.artmed.2008.11.007.

[69] A. Shaw, S. Sriramula, P. D. Gosling, and M. K. Chryssanthopoulos, "A critical reliability evaluation of fibre reinforced composite materials based on probabilistic micro and macro-mechanical analysis," *Composites Part B: Engineering*, vol. 41, no. 6, pp. 446–453, 2010, ISSN: 1359-8368. DOI: https://doi.org/10.1016/j.compositesb.2010.05.005.

[70] T. D. Dinh, A. Rezaei, L. Daelemans, M. Mollaert, D. V. Hemelrijck, and W. V. Paepegem, "A hybrid micro-meso-scale unit cell model for homogenization of the nonlinear orthotropic material behavior of coated fabrics used in tensioned membrane structures," *Composite Structures*, vol. 162, pp. 271–279, 2017, ISSN: 0263-8223. DOI: https://doi.org/10.1016/j.compstruct.2016.12.027.

[71] N. Stranghöner, J. Uhlemann, F. Bilginoglu, K.-U. Bletzinger, H. Bögner-Balz, E. Corne, N. Gibson, P. Gosling, R. Houtman, J. Llorens, *et al.*, "Prospect for European Guidance for the Structural Design of Tensile Membrane Structures," *Science and Policy Report (SaP-Report). Draft Version. To be published by the Joint Research Centre (JRC) of the European Commission, publication expected*, 2016.

[72] M. Rachik, F. Schmidtt, N. Reuge, Y. Le Maoult, and F. Abbeé, "Elastomer biaxial characterization using bubble inflation technique. II: Numerical investigation of some constitutive models," *Polymer Engineering & Science*, vol. 41, no. 3, pp. 532–541, 2001. DOI: 10.1002/pen.10750.

[73] M. Charalambides, L. Wanigasooriya, G. Williams, and S. Chakrabarti, "Biaxial deformation of dough using the bubble inflation technique. I. Experimental," *Rheologica Acta*, vol. 41, no. 6, pp. 532–540, Jan. 2002, ISSN: 0035-4511. DOI: 10.1007/s00397-002-0242-2.

[74] C. A. Mejía and E. O. L. Lantsoght, "Strain and deflection analysis in plain concrete beams and reinforced concrete beams by applying Digital Image Correlation," in *SEMC 2016–Sixth International Conference on Structural Engineering, Mechanics and Computation*, CRC Press, 2016.

[75] M. Drass and J. Schneider, "On the mechanical behavior of transparent structural silicone adhesive–TSSA," in *SEMC 2016–Sixth International Conference on Structural Engineering, Mechanics and Computation*, 2016, pp. 14–16.

[76] C. F. Jekel, G. Venter, and M. P. Venter, "Obtaining a hyperelastic non-linear orthotropic material model via inverse bubble inflation analysis," *Structural and Multidisciplinary Optimization*, pp. 1–9, 2016, ISSN: 1615-1488. DOI: 10.1007/s00158-016-1456-8.

[77] C. F. Jekel, "Digital Image Correlation on Steel Ball," in *Obtaining non-linear orthotropic material models for pvc-coated polyester via inverse bubble inflation*, 2016, ch. Appendix A, pp. 83–87.

[78] M. Sheplak and J. Dugundji, "Large Deflections of Clamped Circular Plates Under Initial Tension and Transitions to Membrane Behavior," *Journal of Applied Mechanics*, vol. 65, no. 1, pp. 107–115, Mar. 1998, ISSN: 0021-8936.

[79] E. Jones, T. Oliphant, P. Peterson, *et al.*, *SciPy: Open source scientific tools for Python*.

[80] D. S. Broomhead and D. Lowe, "Radial basis functions, multi-variable functional interpolation and adaptive networks," Royal Signals and Radar Establishment Malvern (United Kingdom), Tech. Rep., 1988.

[81] D. R. Jones, M. Schonlau, and W. J. Welch, "Efficient Global Optimization of Expensive Black-Box Functions," *Journal of Global Optimization*, vol. 13, no. 4, pp. 455–492, Dec. 1998, ISSN: 1573-2916. DOI: 10.1023/A:1008306431147.

[82] The GPyOpt authors, *GPyOpt: A bayesian optimization framework in python*, http://github.com/SheffieldML/GPyOpt, 2016.

[83] C. G. Broyden, "The Convergence of a Class of Double-rank Minimization Algorithms 1. General Considerations," *IMA Journal of Applied Mathematics*, vol. 6, no. 1, pp. 76–90, Mar. 1970, ISSN: 0272-4960. DOI: 10.1093/imamat/6.1.76.

[84] R. Fletcher, "A new approach to variable metric algorithms," *The Computer Journal*, vol. 13, no. 3, pp. 317–322, Jan. 1970, ISSN: 0010-4620. DOI: 10.1093/comjnl/13.3.317.

[85] D. Goldfarb, "A family of variable-metric methods derived by variational means," *Math. Comp. 24 (1970), 23-26*, 1970. DOI: https://doi.org/10.1090/S0025-5718-1970-0258249-6.

[86] D. F. Shanno, "Conditioning of quasi-Newton methods for function minimization," *Math. Comp. 24 (1970), 647-656*, 1970. DOI: https://doi.org/10.1090/S0025-5718-1970-0274029-X.

[87] R. H. Byrd, P. Lu, J. Nocedal, and C. Zhu, "A limited memory algorithm for bound constrained optimization," *SIAM Journal on Scientific Computing*, vol. 16, no. 5, pp. 1190–1208, 1995.

[88] J. F. Schutte, R. T. Haftka, and B. J. Fregly, "Improved global convergence probability using multiple independent optimizations," *International Journal for Numerical Methods*

in Engineering, vol. 71, no. 6, pp. 678–702, Dec. 2006, ISSN: 0029-5981. DOI: 10.1002/nme.1960.

[89] N. V. Queipo, R. T. Haftka, W. Shyy, T. Goel, R. Vaidyanathan, and P. Kevin Tucker, "Surrogate-based analysis and optimization," *Progress in Aerospace Sciences*, vol. 41, no. 1, pp. 1–28, Jan. 2005, ISSN: 03760421. DOI: 10.1016/j.paerosci.2005.02.001.

[90] C. F. Jekel, R. T. Haftka, G. Venter, and M. P. Venter, "Lack-of-fit Tests to Indicate Material Model Improvement or Experimental Data Noise Reduction," in *2018 AIAA Non-Deterministic Approaches Conference*, 2018.

[91] C. Park, M. G. Fernandez-Godino, N. H. Kim, and R. T. Haftka, "Validation, Uncertainty Quantification and Uncertainty Reduction for a Shock Tube Simulation," in *18th AIAA Non-Deterministic Approaches Conference*, ser. AIAA SciTech Forum, American Institute of Aeronautics and Astronautics, Jan. 2016. DOI: doi:10.2514/6.2016-1192.

[92] R. H. Myers, D. C. Montgomery, and C. M. Anderson-Cook, "Building Empirical Models," in *Response Surface Methodology: Process and Product Optimization Using Designed Experiments*, ser. Wiley Series in Probability and Statistics, Third, Wiley, 2016, ch. 2, pp. 13–62, ISBN: 9781118916032.

[93] T. Gasser, L. Sroka, and C. Jennen-Steinmetz, "Residual Variance and Residual Pattern in Nonlinear Regression," *Biometrika*, vol. 73, no. 3, pp. 625–633, 1986, ISSN: 00063444. DOI: 10.2307/2336527.

[94] J. D. Hart, "Classical Lack-of-Fit Tests," in *Nonparametric Smoothing and Lack-of-Fit Tests*, New York, NY: Springer New York, 1997, ch. 5, pp. 117–143, ISBN: 978-1-4757-2722-7. DOI: 10.1007/978-1-4757-2722-7_5.

[95] A. Coppe, R. T. Haftka, and N. H. Kim, "Uncertainty Identification of Damage Growth Parameters Using Nonlinear Regression," *AIAA Journal*, vol. 49, no. 12, pp. 2818–2821, Dec. 2011, ISSN: 0001-1452. DOI: 10.2514/1.J051268.

[96] N. S. Altman and C. P. Paulson, "Some remarks about the gasser-sroka-jennen-steinmetz variance estimator," *Communications in Statistics - Theory and Methods*, vol. 22, no. 4, pp. 1045–1051, Jan. 1993, ISSN: 0361-0926. DOI: 10.1080/03610928308831072.

[97] P. J. Munson and R. W. Jernigan, "A Cubic Spline Extension of the Durbin-Watson Test," *Biometrika*, vol. 76, no. 1, pp. 39–47, 1989, ISSN: 00063444. DOI: 10.2307/2336367.

BIOGRAPHICAL SKETCH

Charles Jekel graduated from high school in Colorado Springs, Colorado and went on to earn his Bachelor of Science degree in mechanical engineering from the University of Colorado Colorado Springs. As an engineer working for United Technologies Corporation, Charles oversaw the final assembly of commercial flight attendant seats. He completed a research based Master of Engineering degree at Stellenbosch University in South Africa, where his research investigated using an inverse analysis to determine non-linear orthotropic material parameters for PVC-coated polyester.